Syracuse University

SURFACE

Dissertations - ALL   SURFACE

December 2017

Gas Phase Oxidation of Levulinic Acid for the Production of Maleic Anhydride over Supported Vanadium Oxide Catalysts

Anargyros Chatzidimitriou
Syracuse University

Follow this and additional works at: https://surface.syr.edu/etd

Part of the Engineering Commons

Abstract

With continued depletion of fossil carbon, there is a need to utilize renewable sources of energy and consumer end products. In this context, we examine the aerobic oxidation of levulinic acid, a bio-based platform chemical derived from lignocellulosic biomass, to produce maleic anhydride, a valuable commodity chemical. This process is carried out over supported vanadium oxide catalysts. Yields as high as 71% of the theoretical maximum were achieved at 573 K over a vanadium oxide catalyst supported on SiO_2. The exact mechanism underlying this transformation is complex, but our results suggest that maleic anhydride forms by the oxidative cleavage of the methyl carbon in α- and β-angelica lactones, which form as primary products by facile dehydration of LA. We have identified all major and minor/side products, and we propose plausible mechanisms leading to their formation. These mechanistic insights allow us to envision strategies for controlling product selectivity during oxidative cleavage reactions. To probe the extent to which vanadate structure dictates reactivity and selectivity, we consider the oxidative cleavage of 2-pentanone over a number of vanadium oxide catalysts that vary in both vanadium oxide structure and support. We observe that activity and selectivity on supported vanadium oxides is sensitive to both the choice of support and the vanadium loading[1]. Rates scale inversely with the electronegativity of the heteroatom present in the solid oxide support. Finally, as vanadium oxide surfaces display both acid/base and redox functions, we have developed a set of reaction-based tools for characterizing acid site character and density in solid oxides. Specifically, we employ a series of amine titrants in FTIR, Temperature Programmed, and Steady State reaction studies to provide in situ titration of Brønsted acid site density under reaction conditions. In doing so, we observe that small pore zeolites screen amine molecules

based on their kinetic diameter, while materials that vary in Brønsted:Lewis site distribution display contrasting Brønsted acid site densities that are dependent on the degree of substitution of the α-carbon in the alkylamine. Finally, we try to develop new techniques to better measure the intrinsic activity of a Brønsted catalyzed reaction.

Gas Phase Oxidation of Levulinic Acid for the Production of Maleic Anhydride over Supported
Vanadium Oxide Catalysts

by

Anargyros Chatzidimitriou

Diploma, National Technical University of Athens, 2011

Dissertation

Submitted in partial fulfillment of the requirements for the degree of

Doctor of Philosophy in Chemical Engineering.

Syracuse University

December 2017

Acknowledgements

I would like to acknowledge the help of my family, my wife and kids at the time. I might not remember who you are but I thank you! These last six years of my life have been a blur. I was 32 when I first came to Syracuse and now, I have a wife, two kids and this dissertation to finish. Now that it is all about to end, for better or for worse, I am more in a blur than I have ever been before. I have seen people coming and going, professors retiring, professors getting hired, classrooms renovated, Lynore going to SBI and coming back, custodians coming and going, presidents going, the Cubs winning the World Series, the Cavs wining the NBA championship, ZLAD turning into the silly walker and when I first started I thought this as a short station in a bigger journey. That turned out to be not quite as I had anticipated and not at all in a bad way.

For the few weeks of writing my thesis I want to acknowledge music from Clutch, Orbital, Nick Cave and the Bad Seed, Nirvana, Offspring, Augustus Pablo, Monster Magnet, Neil Young, RTJ, QOTSA and The White Stripes. My mp3 player was my only connection outside of the world of catalysis.

Everyone I know just has to put up with me, which is a lot to ask but some people do it and I thank them for that. Firstly, my labmates including Aimee and Omar (first zeolite rap duet ever), Christian, Josh, GVL drinking Xinlei, Ran, Shaofu and Columbia for sponsoring our jackets. I want to acknowledge my advisor, Jesse Bond for the long hours he agreed to sacrifice very late on Friday afternoons in order to help Omar and myself get the HPLC up and running. I also want to thank my dad for posing shirtless on skype, bragging how the temperature in Athens, Greece is 20 °C in the middle of the winter. George, David and Kostas for being true friends 6000 miles away and generally everybody back home that makes it so much harder to be here. Finally, and

joking aside, a huge thanks to Sofia, Nikolas and Alkione for making life fun, my sister, my brother in law and their two monsters for making it even more fun.

I would like to thank Professor Jesse Bond for unlimited hours of academic advising, counseling, etc., Omar Abdelrahman for unlimited conversations, not exclusive to catalysis, Ran Zhu and Robert Glasser for their experiments and input on deciphering vanadium oxide speciation and support interactions. I also want to thank all the people on the third floor of Link Hall for creating a healthy, academic environment.

I want to acknowledge Professor Andreas Heyden and Muhammad Osman Mamun from the University of South Carolina for their generous contribution of thermodynamic data on the oxidative and non-oxidative pathways of levulinic acid, Professor Morris D. Argyle from Brigham Young University for valuable input on the synthesis of vanadium oxide catalysts and Professor Michael T. Timko along with Dr. Geoffrey Tompsett from the Worcester Polytechnical institute for offering to help with UV and Raman spectroscopy. In addition, I would like to thank Professor Stephanie Wettstein from Montana State University for offering us the opportunity to collaborate and Professor Moises A. Carreon for supplying several silicoaluminophosphate zeolites.

"Τα πιο όμορφα πράγματα χάνονται γρήγορα· άνθρωποι, σύννεφα, το μελάνι στα ποιήματα"

Table of Contents

List of Figures

List of Schemes

List of Tables

1 Introduction

Fueled by the waning of fossil reserves, there is increasing interest in biomass conversion. Specifically, there is a renewed call for upgrading non-edible, lignocellulosic biomass. Lignocellulose comprises the structural part of woody plants. It is abundant and widely considered to be the only practical alternative carbon source to presently-used fossil resources, such as crude oil and natural gas. Ideally, as industry becomes more sustainable, it would move from petroleum fuels and petrochemicals to bio-based fuels and chemicals. Because they are consumed on immense scales, biofuels seem to represent an attractive end point for the downstream processing of non-edible lignocellulosic biomass; however, the complex and oxygen rich chemical structure of lignocellulose is, at a molecular level, quite distinct from conventional, liquid transportation fuels [2]. Transportation fuels are generally comprised of alkanes— paraffins (linear alkanes), isoparaffins (branched alkanes), and napthenes (cyclic alkanes)—and aromatic compounds[3]. Refineries go to great lengths in hydrotreating to ensure that they are devoid of heteroatoms. In contrast, lignocellulose—the proposed alternative starting point for a sustainable industry—is made up of the heavily oxygenated polymers of lignin, cellulose and hemicellulose[2]. Cellulose is a polysaccharide made up of linked glucose monomers; hemicellulose is a polysaccharide comprised of pentoses (arabinose, xylose) and hexoses (glucose, mannose, and galactose); and lignin is a linked collection of the monolignols: paracoumaryl alcohol, coniferyl alcohol and sinapyl alcohol. Clearly, transforming polysaccharides and lignin into transportation fuels represents a daunting chemical challenge that requires fragmentation, defunctionalization, and (often) carbon-carbon bond formation to build fuel molecular weight into the diesel and aviation fuel ranges. Although technologies for delivering these so-called "advanced biofuels" have certainly been developed, the cost of

deconstruction and deep deoxygenation is substantial, and they have, to date, been unable to compete with petroleum fuels.

The challenge of making biofuels hinges on the extensive chemical functionality of lignocellulose. Removing this functionality and converting the carbon into a liquid alkane fuel is complex and expensive, and biofuels have difficulty competing against petroleum refining, which mostly depends on crude fractionation, cracking, and hydrotreating to remove trace heteroatoms.

In contrast, the manufacture of petrochemicals from natural gas and crude oil broadly requires *introducing* chemical functionality to inert alkanes, which is generally either extremely endothermic and/or requires kinetically difficult alkane activation [3]. More often than not, petrochemical synthesis suffers from difficult selectivity control (e.g., partial oxidation) and/or high energy demand (e.g., dehydrogenation, aromatic synthesis). As with biofuels synthesis, the production of chemical commodities from lignocellulose contrasts with crude oil upgrading. Specifically, the extensive oxygen functionality of polysaccharides and lignin make them inherently reactive relative to crude oil, which allows them to be processed under relatively mild conditions where it may be possible to effect both energy efficiency and selectivity control.Furthermore, the high oxygen content of polysaccharides make them ideal feedstock for the production of functionalized chemicals and thus a competitive precursor compared to crude oil.

The remainder of this thesis focuses on partially oxygenated hydrocarbons—namely maleic anhydride—as they are a valuable class of products used as precursors for a vast number of consumer end products. Biomass can offer such products at much milder conditions by incorporating the already rich and diverse functionality of biomass derived platform chemicals,

while selectivity control can be achieved with appropriate catalyst selection. As a chemicals feedstock, biomass becomes increasingly attractive relative to fossil hydrocarbons with the amount of oxygen in the target product. With the above in mind we present a novel pathway for the production of maleic anhydride (MA) through the aerobic oxidation of levulinic acid (LA) over supported vanadium oxide catalysts[4]. Before delving into the process and the technical details of this reaction, there is a need to highlight the reasons behind the choice of LA as a feedstock for the production of MA and attempt a comparison between the industrially established process and the one proposed herein from an economic standpoint taking into account differences in process parameters.

2   Linking Levulinic Acid to Maleic Anhydride

2.1   Significance of Levulinic Acid as a Platform Chemical and Current Outlook

Levulinic acid is an intriguing platform chemical identified by the Department of Energy as one of 12 top bio-based molecules [5]. LA can be derived through either five-carbon (C_5, pentose) or six-carbon (C_6, hexose) [6] sugars as depicted in Scheme 1.
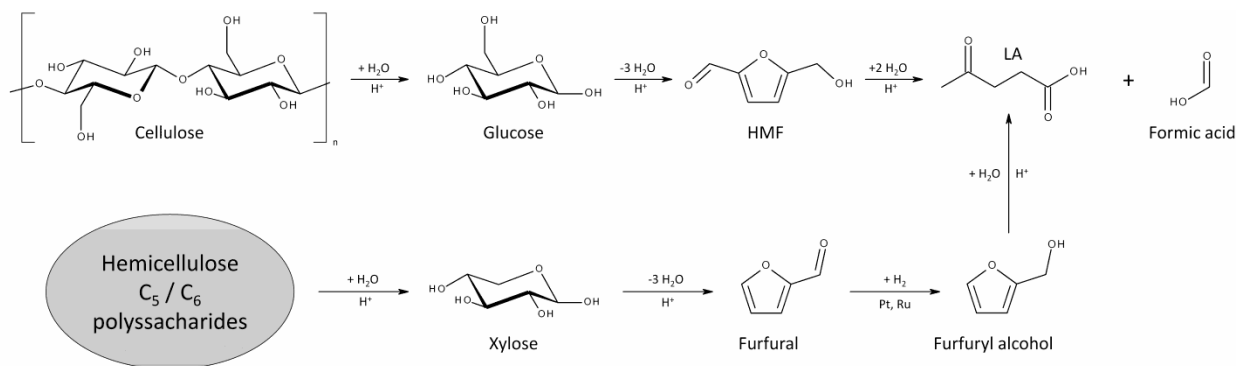
Scheme 1 *Possible pathways for LA production from lignocellulosic biomass*

The pentose route relies on acid-catalyzed hydrolysis of furfuryl alcohol, which is obtained by selective hydrogenation of the carbonyl group in furfural. Furfural is produced by triple dehydration of pentose sugars, such as xylose, and it can generally be recovered from direct acid hydrolysis of C_5 polysaccharides, such as xylans [7, 8]. Similarly, the hexose route is based on acid-catalyzed hydrolysis of cellulose followed by dehydration of the resulting glucose (C_6) monomers, which produces 5-hydroxymethylfurfural (HMF). In aqueous solution, HMF is rehydrated under to form LA and formic acid[9]. The preceding section establishes that LA can realistically be produced from abundant C_5 and C_6 containing polysaccharides using primarily acid-catalyzed reactions, suggesting fairly economical production. It is also worth noting that LA is a bifunctional molecule, which presents a range of possible downstream applications that are highlighted below.

LA itself has little value as a chemical commodity, and there are presently no potential large-scale LA consumers to support development of LA-production facilities; however, LA offers intriguing chemical functionality, and it can be upgraded to multiple potentially saleable products including fuels, fuel additives, and chemical commodities. For example, LA can be converted into oxygenated fuel additives such as gamma-valerolactone[10] methyltetrahydrofuran[11], alkyl levulinates[12], alkyl valerates[13], alkane fuels[14-19] and niche specialty chemicals, such as the herbicide δ-aminolevulinic acid (DALA)[20] as depicted in Scheme 2.
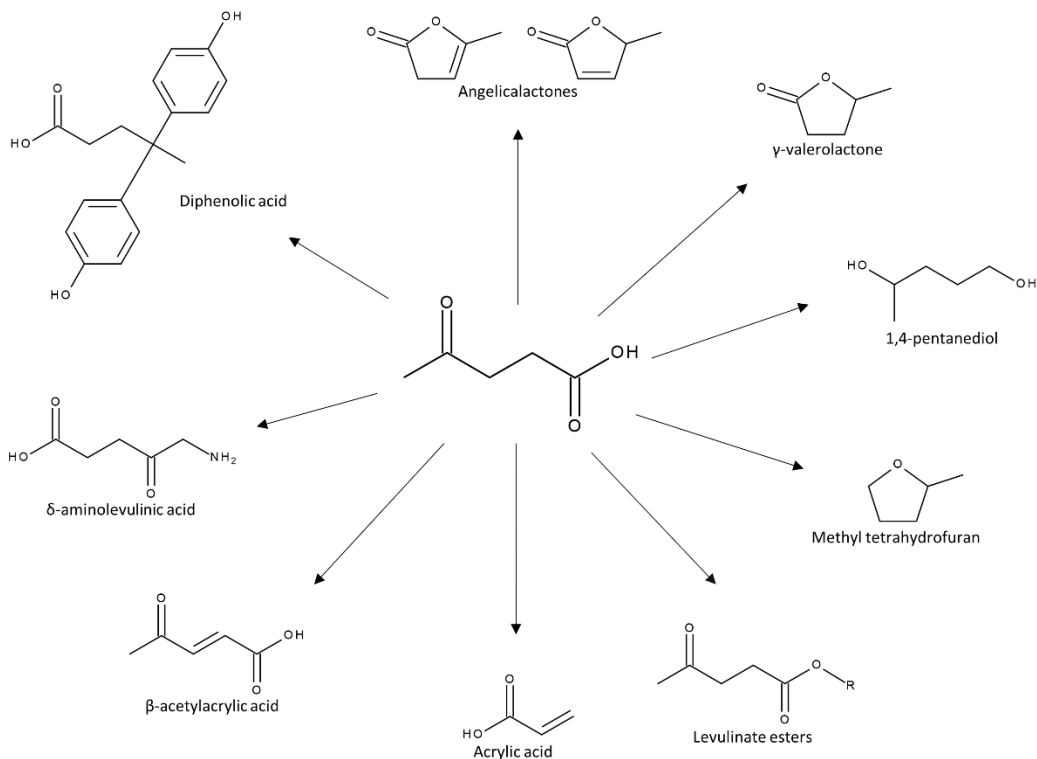
Scheme 2 *Established downstream processing of levulinic acid (LA)*

To date, the majority of commercialization attempts for LA typically involve the production of biofuels, such as ethyl levulinate; however, due to the aforementioned costs of deep deoxygenation, such biodiesel is not able to compete with crude oil diesel at current prices. Recognizing that bio-platforms such as LA are generally unable to compete with crude oil for the production of transportation fuels, one can argue that targeting the production of chemical commodities—which are relatively difficult to synthesize from crude—is more economically viable in the near term. It is in this context that we discuss the production of MA from LA.

We recently demonstrated that oxidation of LA over supported vanadium oxides gives appreciable, single-pass yields of MA. Maleic anhydride (MA) is the dehydration product of maleic or fumaric acids, which are cis/trans C_4 diacid isomers (Scheme 3).

2.2 Importance and Current Production Routes of Maleic Anhydride
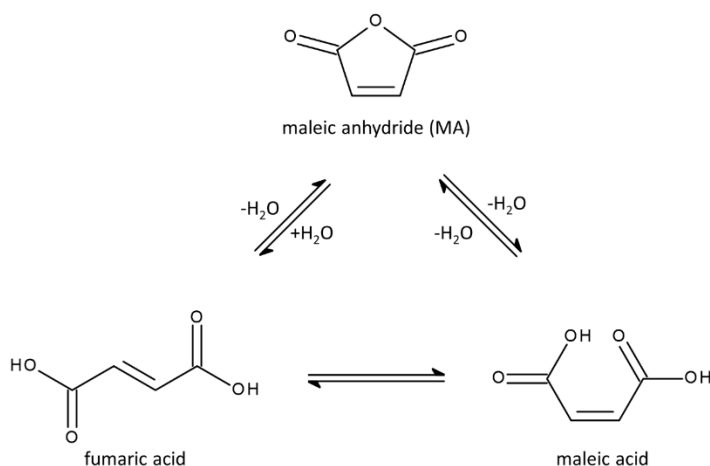
Scheme 3 *Interconversion between maleic, fumaric acid and their anhydride (MA)*

Relative to crude oil, MA has a high oxygen to carbon ratio (O:C = 3:4). It is produced

industrially either by oxidation of n-butane ($0.21-0.58 per kg, 2014-2017[21]) or oxidation of

benzene (~$1 per kg, 2017[22]) as shown in Scheme 4. Benzene oxidation is carried out over

supported vanadium oxide catalysts. This route is regarded as selective, and it is capable of

achieving single pass yields of MA greater than 70% at 623-673 K[23].
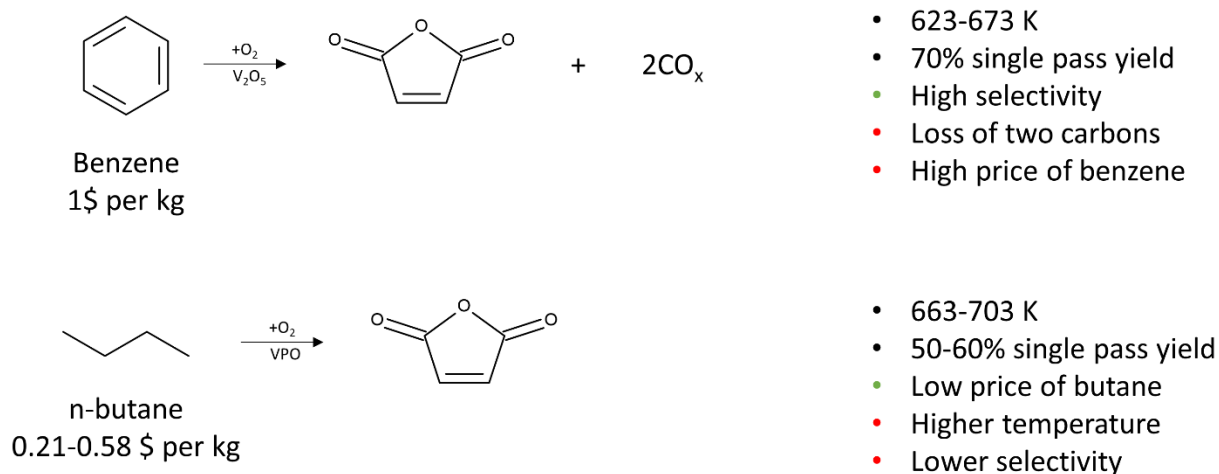
Scheme 4 *MA synthesis in the petrochemical industry*

The oxidation of n-butane is carried out over vanadium phosphate catalysts, which selectively oxidize the C_1 and C_4 methyl carbons in butane with minimal C-C cleavage [24]. Butane oxidation is well-studied within both academia and the petrochemical industry. To date, it has been optimized to give a maximum MA single pass yield of not more than 50-60% at 663-703 K. More generally, it is carried out at low single pass conversions under recycled conditions to achieve overall yields comparable to the benzene oxidation process. Comparing the two processes, butane oxidation occurs at higher temperatures and gives lower single-pass selectivity; however, in recent history, these factors are offset by the low price of butane relative to benzene, and butane oxidation has become the industry standard for MA synthesis.
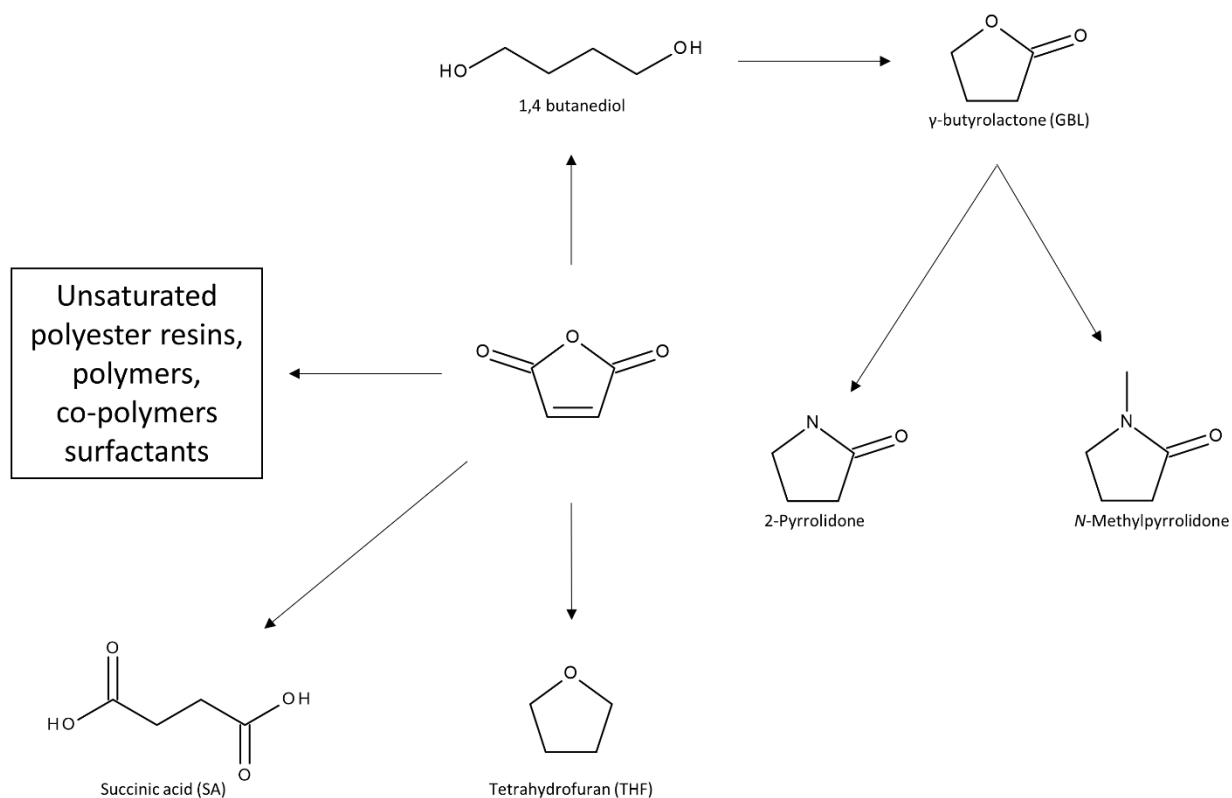
Scheme 5 *Existing market for the utilization of MA*

Scheme 5 details the existing market for utilization of MA. It is primarily used (>60%) for the production of unsaturated polyester resins; however, it also serves as a precursor to 1,4 butanediol, tetrahydrofuran, γ-butyrolactone and, alongside styrene, acrylonitrile, vinyl compounds, acrylic compounds, alkenes and nitrogen containing monomers, as an ingredient in the manufacture of co-polymers [23]. These numerous downstream applications ensure a number of offtakers for MA, and it is generally considered to have a well-established and robust global market (1500-2000 kilotons per year [25]).

MA production from butane is not highly selective. This arises from the process parameters and specifically the high temperatures required for the functionalization of alkanes. These high temperatures result in the overoxidation of alkanes shifting the selectivity from desired products. Alternatively, oxygenated biomass derivatives can serve as better feedstock for the production of oxygenated commodity chemicals like MA as one would generally expect milder reaction temperatures which can lead to more selective processes.

2.3   Levulinic Acid as an Alternative Feedstock for the production of Maleic Anhydride

Alternatively, we propose the use of levulinic acid (LA) as an intermediate for the production of MA from lignocellulosic biomass, which we have demonstrated to occur at mild temperatures (573-598 K) compared to butane oxidation (663-703 K). The conversion of LA into MA is facilitated by the cleavage of the methyl carbon in LA, and it occurs over supported vanadium oxide catalysts. Specifically, we have achieved MA yields as high as 71% of the maximum theoretical yield over vanadium oxides supported on amorphous silica. Compared to the established industrial process of butane oxidation, we were able to achieve 10-20% higher single pass yields of MA at a temperature that was at least 90 K lower. Dunlop [26] has also reported

the production of succinic acid through the oxidation of LA vapors over vanadium oxide supported on pumice in 1954. Succinic acid is the saturated equivalent of maleic acid and we will discuss the disparity between ours and the findings in Dunlop's patent during the description of the possible reaction pathways.

From an economic standpoint, BioFine, a biorefinery process technology company that has established the production of LA through an acid hydrolysis process, has indicated that cellulose-derived LA can be produced for roughly $0.21 per kg[20]. Based on this price and a yield of 70%, the cost of LA would contribute roughly $0.36 per kg to MA manufacture, which is comparable to estimated butane expenses in the conventional approach. Based on butane prices over the past years and reported MA yields of 70% under industrial conditions of full recycle, we estimate that butane purchasing will contribute $0.18-0.49 per kg to the cost of MA production, where the variation reflects fluctuations in the butane market price over the past decade. While BioFine's estimate of the LA production cost is likely optimistic, it is worth noting that LA production costs could increase roughly 2.5-fold to $0.53 per kg before LA is unable to compete with butane at $1.05 per kg, where it's price peaked in 2008 and approached again in 2012. Certainly, the LA-based approach becomes more attractive as the price of butane increases. Further, although 70% is likely a ceiling on attainable MA yields during well-optimized butane oxidation under recycle conditions, we see no reason that the best single-pass yield reported here (71%) represents an upper limit on attainable MA selectivity during LA oxidation; therefore, future optimization could make the LA-based approach more attractive.

3 Selectivity Trends in Levulinic Acid Oxidation Over Supported Vanadates

3.1 Mapping the Reaction Network for the Oxidative Cleavage of Levulinic Acid to Maleic Anhydride

Prior to summarizing trends in LA conversion and product selectivity with variation in operating conditions and catalyst selection, we facilitate a comprehensive discussion of selectivity by considering the landscape of oxidative and non-oxidative reactions that occur in this system. Scheme 6 represents a collection of oxidative and non-oxidative pathways that lead to the formation of the most abundant reaction products observed including two plausible pathways for the production of MA through the oxidative cleavage of LA.
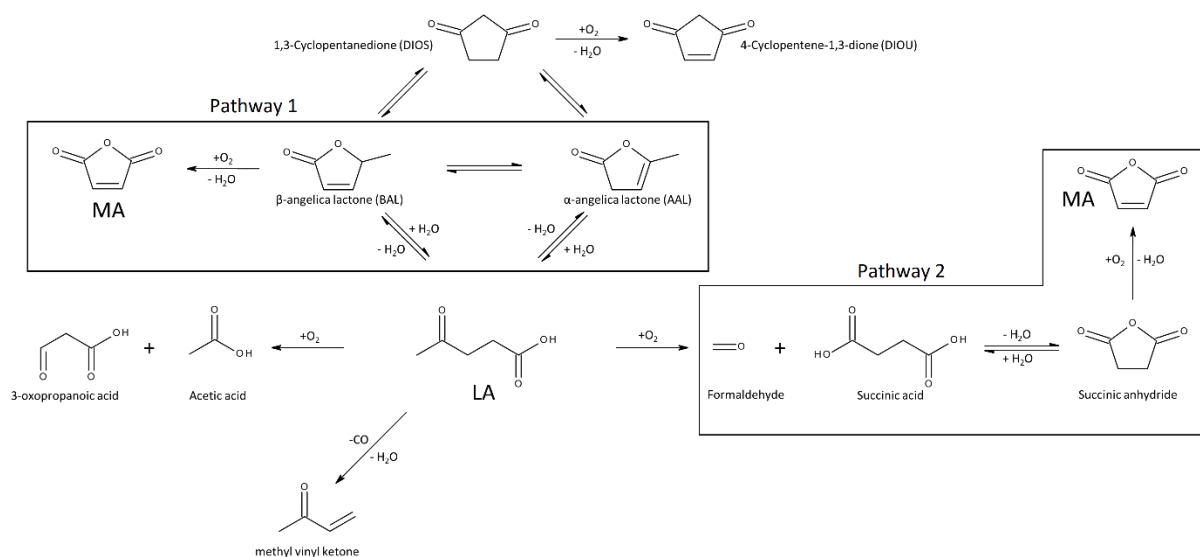
Scheme 6 *Oxidative and non-oxidative pathways for the consumption of LA and its derivatives over supported vanadates*

We have identified two possible pathways for the formation of MA via oxidative scission over vanadium oxide catalysts. Pathway 1 entails the oxidative scission of the methyl carbon in angelicalactones. LA can easily be converted to angelicalactones via a simple dehydration step.

Pathway 2 entails the direct oxidative scission of the methyl carbon in LA. The latter pathway

has been described in the oxidative cleavage of methylketones[27-29]. LA is a bifunctional

molecule, featuring both carboxylic acid and ketone functionalities and we believe that oxidative

cleavage in LA follows similar pathways with that of monofunctional methylketones as depicted

in Scheme 7.
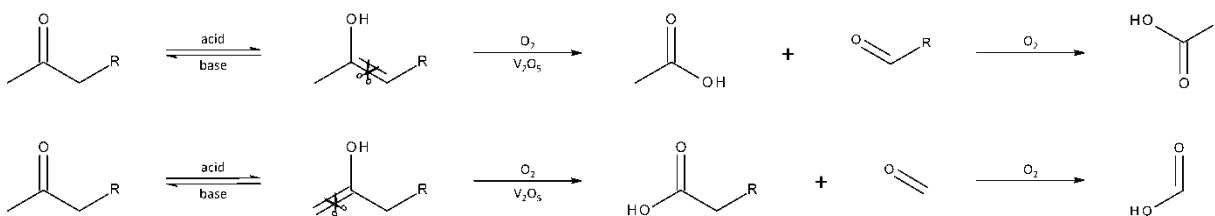
Scheme 7 *Possible pathways for oxidative cleavage in methyketones*

Oxidative cleavage of methylketones occurs on the C-C double bond that forms after the

enolization of the ketone. Depending on the position of the double bond the scission yields a

mixture of different aldehydes and carboxylic acids.

At first glance, the two pathways of Scheme 6 are not very dissimilar; there can, however, be

significant impacts on product selectivity depending on which one is more dominant.

Rearrangement of angelicalactones produces the 1,3 cyclopentanedione (DIOS) which can

further undergo oxidative dehydrogenation to form its unsaturated equivalent, 4-cyclopentene-

1,3-dione (DIOU), It is worth mentioning that DIOS and DIOU are both intriguing,

multifunctional molecules. To our knowledge, their synthesis from LA has not been previously

reported, and future efforts directed toward optimizing their selectivity may establish them as a

new class of bio-based platform intermediates. Methyl vinyl ketone can also be obtained by the

decarbonylation of LA. At elevated temperatures, all observed products are expected to further

oxidize, to some extent, to CO_x. Oxidative cleavage of LA was studied at varying temperature, LA partial pressure, oxygen partial pressure and catalyst loading. In addition, different catalyst supports were employed in order to probe their intrinsic oxidative activity. Finally, product selectivities in the oxidative cleavage of 2-pentanone, a monofunctional analogue of LA, were contrasted with those of LA.

3.2 Materials and Methods

3.2.1 Catalyst Synthesis

Bulk vanadium oxide has very limited surface area (4 m^2g^{-1}) and a significant mass would be required to achieve appreciable catalytic activity. Instead, oxide supports such as γ-Al_2O_3, SiO_2 and TiO_2 offer a much higher surface area onto which vanadium oxide species can be deposited. A disperse vanadate monomolecular layer was deposited on all three supports via the wet impregnation method. Each support including γ-Al_2O_3 (low soda, Strem Chemicals 95%), TiO_2 (Aeroxide® P25, Acros) and SiO_2 (99% Davisil grade 633, Sigma) was mixed with the appropriate amount of ammonium metavanadate dissolved in a 1M solution of oxalic acid (98% anhydrous, Acros). The mixture was evaporated to dryness. Subsequently the catalyst was calcined at 723 K for 240 minutes, under 50 sccm of air (Airgas, Ultra Zero) and was crushed and sieved to achieve a uniform particle size between 45 and 90 μm. The molar quantity of vanadium employed for synthesis was calculated based on the BET surface area of each support (Table 1) obtained using a commercial system (Micromeritics ASAP 2020), with the aim of creating an amorphous, two-dimensional vanadia monolayer in contact with the oxide support. Bulk V_2O_5 (98%, Acros) was also considered.

Table 1 *Surface area characterization of employed catalysts*

Catalyst	*Support*	*Weight % of V*	Support S_{BET} (m^2g^{-1})	Catalyst S_{BET} (m^2g^{-1})	Surface density (V atoms per nm^2)
V_2O_5	n/a	56	n/a	4	
VO_x/Al_2O_3	Al_2O_3	15.7	231	216	9.5
VO_x/SiO_2	SiO_2	9.6	481	333	2.6
VO_x/TiO_2	P25	4.3	56	31	9.5

For Al_2O_3 and TiO_2 supports, $9.5VO_x/nm^2$ was the targeted coverage; while in the case of the

SiO_2 support, the coverage was limited to $2.7VOx/nm2$, due to the low density and reactivity of

the surface hydroxyls[30].

3.2.2 LA and 2-Pentanone Oxidation Reactions

Maleic acid (98%, Fisher), acetaldehyde (99.5%, Sigma), acetic acid (99.8%, Acros),

propionaldehyde (99%, Acros), propionic acid (99%, Acros), acrylic acid (99%, Acros), 4-

cyclopentene-1,3-dione (95%, Sigma Aldrich), butenone (99%, Sigma), α-angelica lactone (MP

Biomedicals), CO (99.99% Praxair) and CO_2 (5% in N2, Airgas) were used as supplied from the

manufacturers for standard preparations and instrument calibrations. Acetone (99.9%, Fischer)

was used as a solvent for all reactor samples and standard preparations. Levulinic acid (LA, 98%,

Sigma Aldrich) and 2-pentanone (99%, Acros) were used as reactor feeds. Purified water used in

catalyst preparation and HPLC mobile phases were prepared in house by sequential reverse

osmosis, UV oxidation, and double ion exchange. He (99.999%, Airgas) was used as a diluent,

O2 (99.999%, Airgas) and O2 (1% in He with 1% Ar, Praxair) were used as oxidants, while air

(Airgas, Ultra Zero) was used for calcinations both in the catalyst synthesis phase and for the in-

situ calcination of the catalytic reactor prior to reaction.

The catalyst powder was placed in a ½" stainless steel tubular reactor and was held in place by two quartz wool plugs. The remaining volume of the tube was filled with quartz granules (800-2000 μm in size) in order to minimize dead volume and enhance the mixing characteristics. Scheme 8 is a depiction of the reactor setup used for this particular experiment.
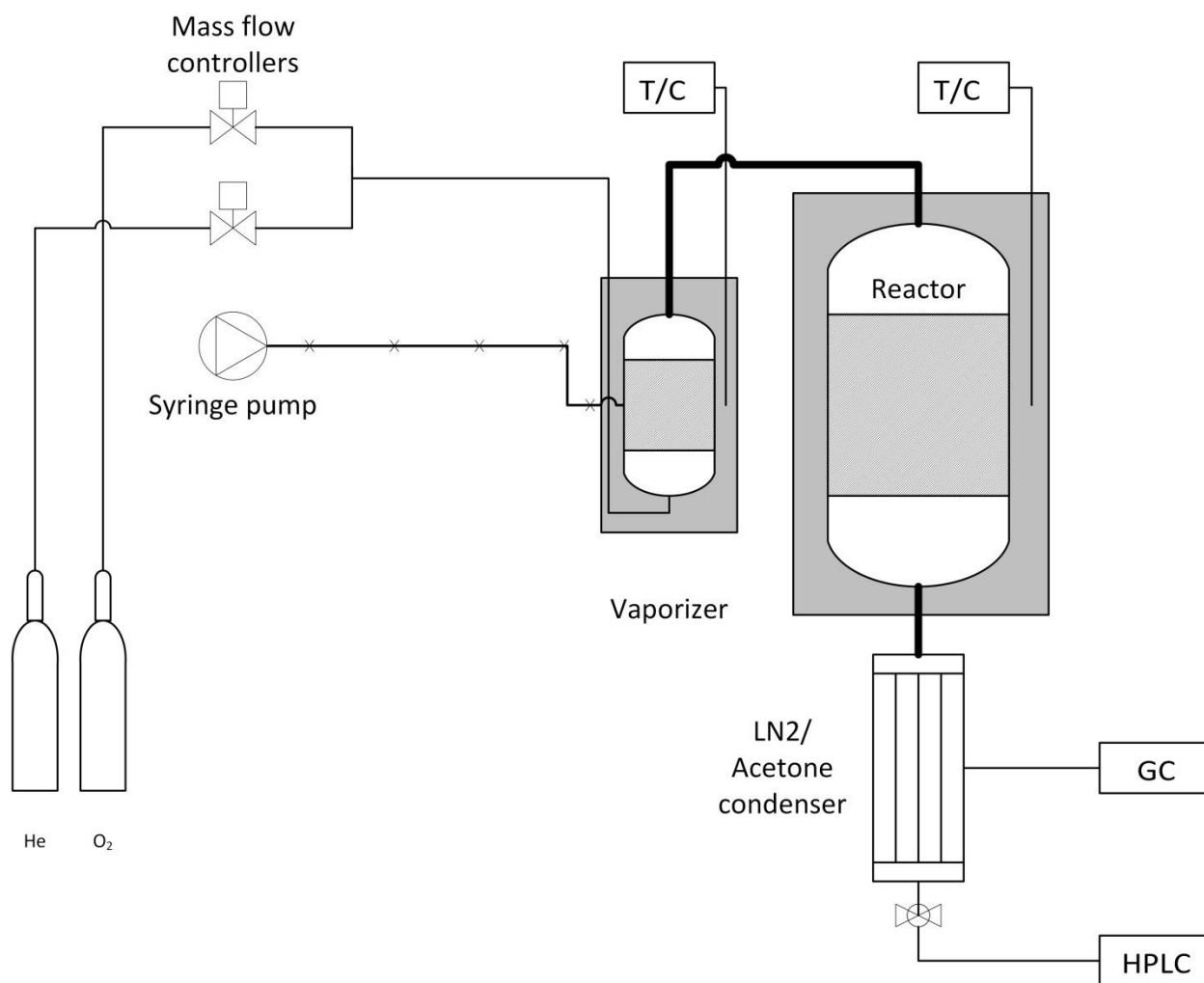
Scheme 8 *LA oxidation reactor*

The reactor tube was placed in a ceramic tubular furnace (Omega CRFC). Manual mass flow controllers (Vici Valco, Model 300) where used to control flowrates of He and O_2 while a

syringe pump (Cole Parmer Series 100) was employed to control the liquid feed rate. Both gas and liquid streams were preheated and introduced in the vaporizer chamber in a countercurrent fashion, heated by a furnace built in-house. At the exit of the catalytic reactor, the gaseous effluent was scrubbed using an acetone filled trap, which was typically immersed in an ice bath to allow rapid cooling and capture of condensable reaction products. After the initial introduction of LA and oxidant feeds to the catalyst bed, it was permitted 48 hours to reach a steady state. Data reported here were collected over roughly 200 hours on stream for a given catalyst sample. During this time, reactors were periodically returned to the initial operating conditions, and comparison of rates to the initial steady state data indicated that no significant activity losses occurred over the course of a given experiment. Though long-term stability was not assessed, catalysts employed here were observed to be fully regenerable for five consecutive reaction cycles via calcination in air at 773 K.

All product species reported here, with the exception of CO_x, were recovered in the condenser. All condensed species, with the exception of MA, were quantitatively analyzed by an Agilent 7890 GC equipped with an FID detector and an HP-INNOWAX column; initial identification of products was conducted by an Agilent 7890 GC equipped with a 5975C MS detector via an HP-INNOWAX column. Chromatographic analysis of diacids, including MA, is challenging. To positively identify MA as our major product, an experiment was devised in which the reactor effluent was passed through a methanol bath with the purpose of esterifying the acids and diacids of our product stream. Esters of maleic, fumaric and succinic acid were positively identified against the "Japan AIST/NIMC Database" [31] as shown in Figure 1.

GC-MS Chromatogram
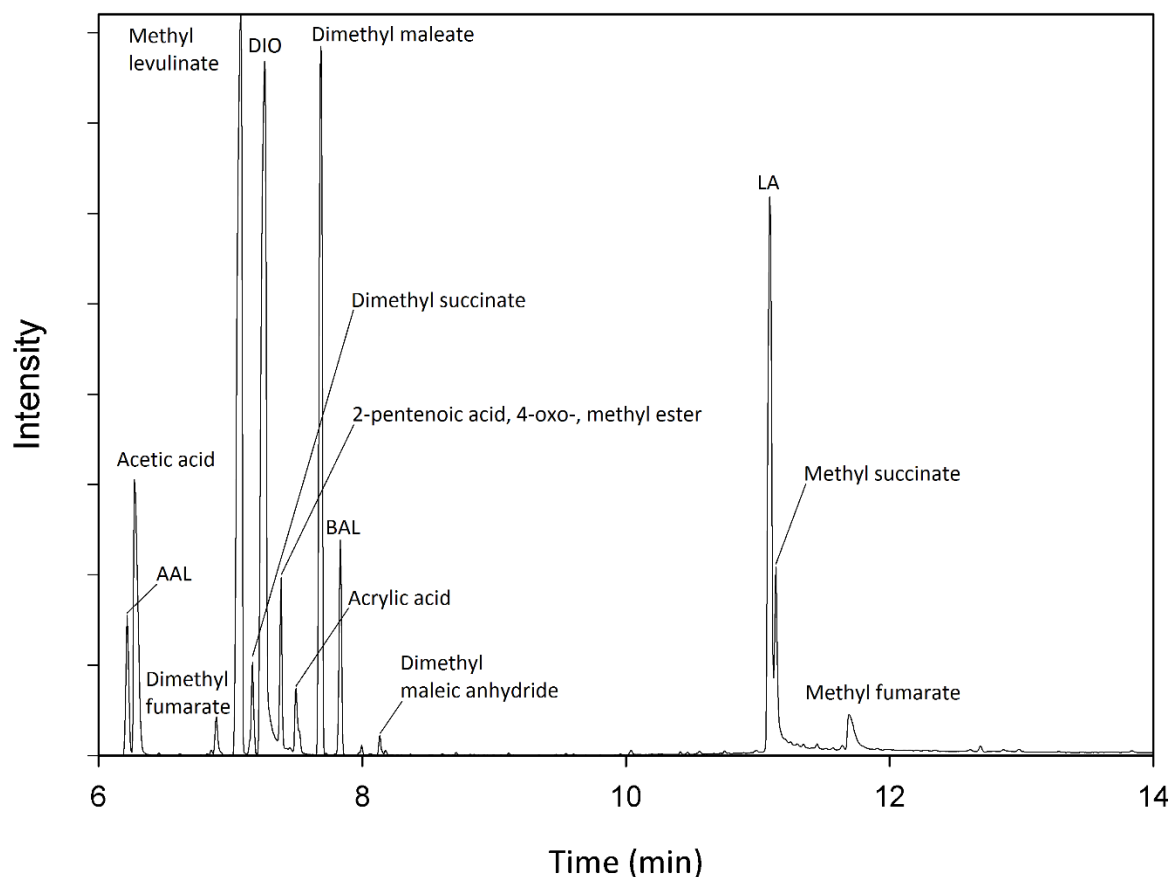
Figure 1 *GC-MS chromatogram of esterified product stream*

MA was quantified using an Agilent series 1100 HPLC equipped with a Hi-Plex column. For this analysis, we employed a pH 2 aqueous H_2SO_4 mobile phase and quantified MA concentrations using a variable wavelength detector (Agilent 1100 VWD). Because of the relatively high temperatures and low water partial pressures in our reactor, we anticipate that MA exits our reactor as its anhydride; however, because of the aqueous nature of our analysis, MA was quantified here as maleic acid. The vapor phase (CO_x) was sent to an in-line chromatograph (GC

7890 Agilent). CO_2 was resolved from CO using a packed column (Restek ShinCarbon ST Micropacked) and quantified via TCD response relative to a helium reference.

3.3   Results and Discussion

3.3.1   Angelicalactone Mediated Pathways Through the Dehydration of LA

At this point we will consider all the possible pathways that involve some transformation of the dehydration products of LA, α- and β-angelicalactones. Pathway 1 in Scheme 6 depicts a lactone mediated pathway for the oxidative cleavage of LA. From LA, a non-oxidative, acid catalyzed dehydration step results in the formation of α-angelicalactone (AAL, $\Delta G \approx$ -11 kJ mol^{-1} at 548 K), as depicted in Scheme 9. Subsequent migration of the double bond ($\Delta G \approx$ 1 kJ mol^{-1} at 548 K) yields β- angelicalactone
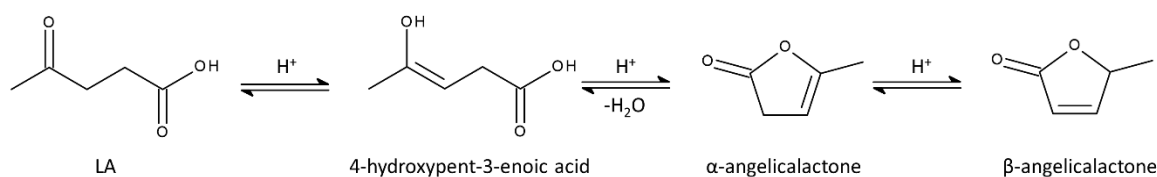
Scheme 9 *Dehydration of LA to the two lactone forms*

Oxidative cleavage of the methyl carbon in β-angelicalactone will yield MA. Furthermore, C_5 diones (DIO), specifically 1,3-cyclopentanedione (DIOS) and its dehydrogenated analog, 4-cyclopentene-1,3-dione (DIOU) are believed to be direct products from angelicalactones. DIOS is an isomer of α- and β-angelicalactone, and electronic structure calculations suggest that its formation from either angelicalactone (ANG) is slightly favorable, occurring with $\Delta G \approx -1$ to -2 kJ mol^{-1} at 548 K. DIOS is thus anticipated in appreciable quantities over this range of

temperatures, provided that its formation is not limited by the rate of ANG isomerization. Subsequently, ODH of DIOS should result in irreversible formation of its unsaturated analog, DIOU ($\Delta G \approx -177$ kJ mol^{-1} at 548 K). ODH is facile under high temperatures so DIOU should generally become the dominant DIO as temperature increases.

3.3.2 Direct Oxidative Cleavage of LA

The direct oxidative cleavage of the methyl carbon in LA has been considered in pathway 2 of Scheme 6. Oxidative cleavage over supported vanadates is common and has been reported for olefins such as 2-butene and simple methylketones like 2-butanone[27-29] as shown in Scheme 7. The ketone moiety in LA should undergo similar oxidative cleavage reactions. McCullagh et al. [32-34] showed that cleavage of 2-butanone is mediated through an enol intermediate. More specifically, any ketone can undergo acid or base catalyzed keto-enol tautomerism to its two possible enol forms. Subsequent cleavage occurs at the C-C double bond. For LA, the two possible enol forms are one with the C-C double bond in the internal position (C_2-C_3) and one with the C-C double bond in the terminal position (C_1-C_2) as depicted in Scheme 10.
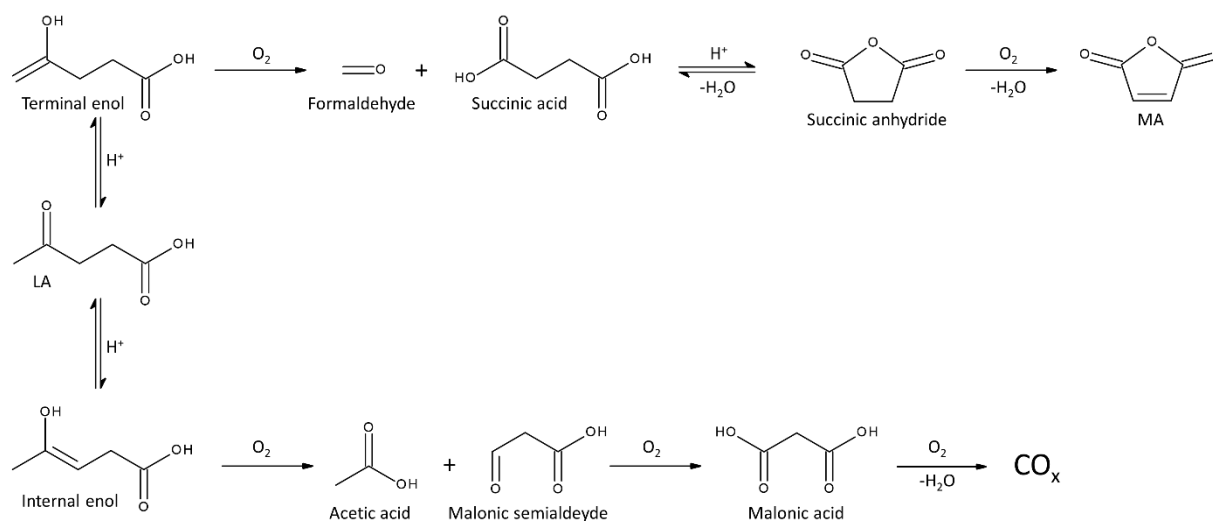
Scheme 10 *Pathways for the direct oxidative cleavage of LA*

Oxidative cleavage of the internal enol produces acetic acid and malonic semialdehyde, which is unstable and readily oxidizes to malonic acid. Traces of acetic acid were quantified; however, no malonic semialdehyde or malonic acid was observed which might indicate that cleavage between the C_2 and C_3 carbon is not favorable. Malonic acid is also not stable at temperatures above 453 K where its decarboxylation to acetic acid and CO_2 is very facile[35], complicating the quantification of internal cleavage products.

Anticipated products of the terminal C-C cleavage are formaldehyde and succinic acid (SA). This C-C scission proceeds irreversibly ($\Delta G \approx$ -326 kJ mol^{-1} at 548 K). Production of SA was reported by Dunlop; however, having employed similar catalysts and conditions as Dunlop, we recovered MA as our dominant product, whereas SA was recovered in trace amounts (<1%). A possible explanation for this is that cleavage occurs as indicated by Dunlop to form SA; however, under our reaction conditions SA, or its anhydride, undergoes secondary oxidative dehydrogenation (ODH) to form MA. ODH of SA to MA is kinetically possible and

thermodynamically favorable ($\Delta G \approx$ -157 kJ mol^{-1} at 548 K) over supported vanadates[36]. As a result, MA could form as the major product as long as the oxidative cleavage of LA is slower compared to SA oxidative dehydrogenation. Under reaction conditions, formaldehyde most likely oxidizes to CO_x.

At first glance, both pathways for the formation of MA, direct cleavage of the methyl carbon in LA and cleavage of the methyl carbon in AAL, seem plausible over vanadium oxide catalysts.

3.3.3 Influence of Temperature and Contact Time on Product Selectivities

In an attempt to further understand selectivity trends in LA oxidation, temperature and contact time were varied. In this system, contact time is defined as the ratio of total moles of vanadium present on the catalyst over the molar flowrate of the feed molecule. By decreasing the contact time of the reactant we can assess condition where the feed is more likely to react and form primary products, while the product stream at increasing reactant contact times will feature products of secondary, tertiary, etc., reactions. LA conversion increases with temperature and contact time up to a temperature of 598 K, where complete LA conversion is observed at all contact times. MA selectivity is favored by increasing reaction temperature, which suggests that oxidative cleavage of LA proceeds with a higher barrier than competing side reactions. At all temperatures, we further observe that MA selectivity improves with contact time even under conditions of complete LA conversion (see 598 K, Figure 2). This may indicate that MA forms as a secondary product during LA oxidation. MA being a secondary product is in line with all three proposed pathways. Over VO_x/γ-Al_2O_3, the highest MA selectivities (50–60%) were observed under conditions of complete LA conversion at 598 K and contact times from 4–16 min.
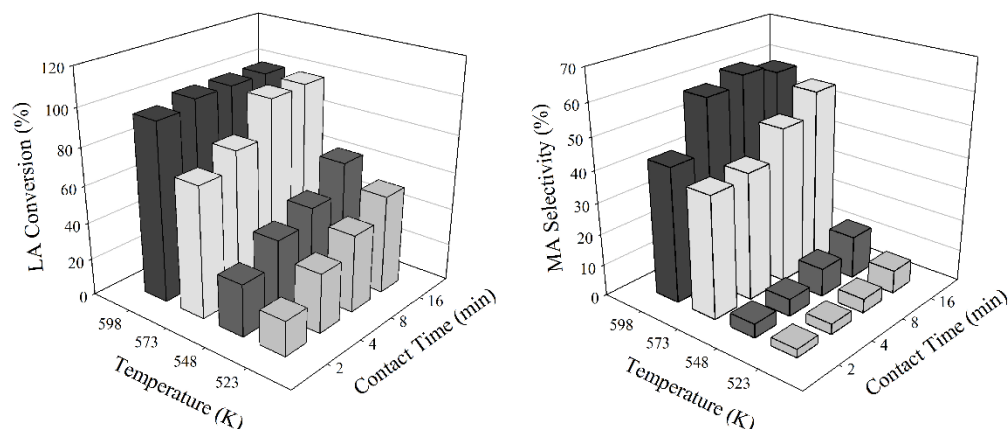
Figure 2 *LA conversion and MA selectivity as a function of temperature and contact time over VOx/γ-Al2O3. MA selectivity is defined as the molar quantity of MA formed normalized by the molar quantity of LA consumed. Contact times are calculated as the molar loading of vanadium in the reactor normalized by the molar feed rate of LA. p_{LA} = 0.016 bar, p_{O_2} = 0.33 bar.*

Because of the complexity of this reaction landscape, it is difficult to assign molar selectivities to all products as we have done for MA. Accordingly, Figure 3 summarizes complete carbon distributions for the reaction products recovered during LA oxidation over VOx/γ-Al$_2$O$_3$ Selectivities are presented for angelicalactones (ANG), diones (DIO), MA and CO$_x$. Acetic acid, acrylic acid, acetaldehyde, propionaldehyde and MVK were observed in sufficient quantities to warrant inclusion in the carbon balance (1−5%), and these species are lumped into the category "other".
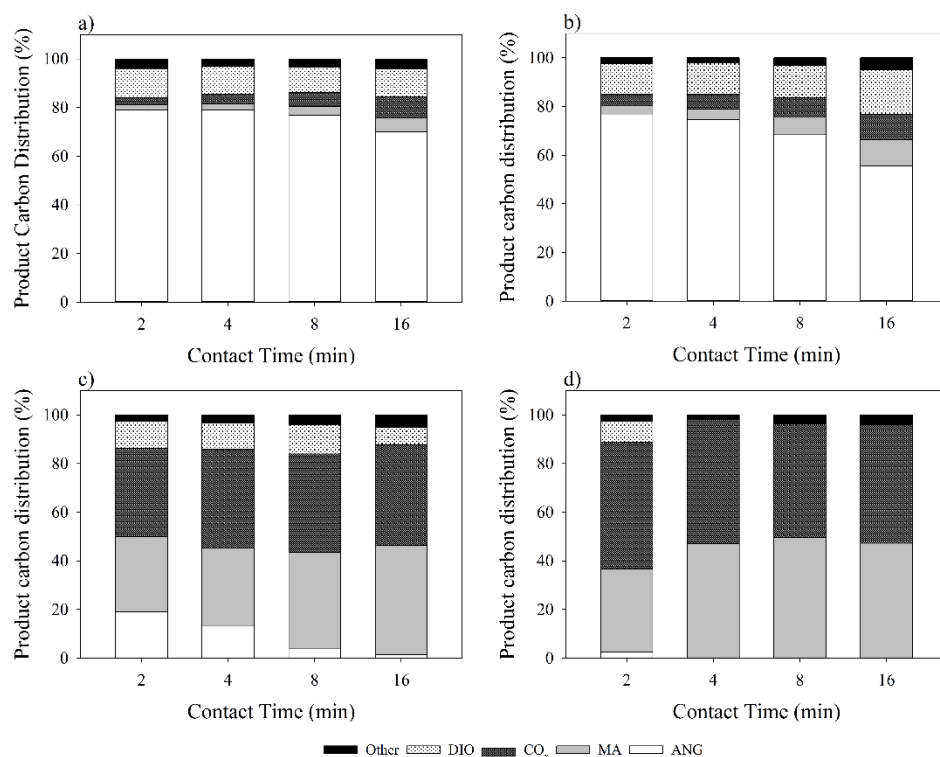
Figure 3 *Product carbon distributions as a function of contact time. (a) 523 K, (b) 548 K, (c) 573 K, (d) 598 K.*

Angelicalactones (ANG) and diones (DIO) dominate the landscape at low temperatures and low contact times. As temperature increases, selectivity changes are drastic. At high temperatures, selectivity switches to MA and CO_x; however, it is not clear whether MA forms via consumption of LA or ANG. In any case, the dehydration of LA to form ANG isomers is thermodynamically favorable, but likely equilibrium limited ($\Delta G \approx -7$ to -18 kJ mol^{-1}) between 523 to 598 K. We can thus consider two possible scenarios. In one scenario, MA is produced at the expense of LA, and ANG reverts back to LA due to the displacement of the equilibrium position by LA consumption. Assuming that oxidative cleavage has a higher barrier compared to dehydration, as temperature increases, selectivity shifts to MA while the DIO/ANG pool of species is swiftly converted back to LA as it is readily consumed for the production of MA, consistent with

pathway 2 from Scheme 6. In the second scenario, MA is produced by consumption of angelicalactones, consistent with pathway 1.

3.3.4   Influence of Oxygen Partial Pressure on Product Selectivities

Oxygen partial pressure was varied from 0.01 to 0.83 bar in order to study its influence on LA conversion and product selectivity.
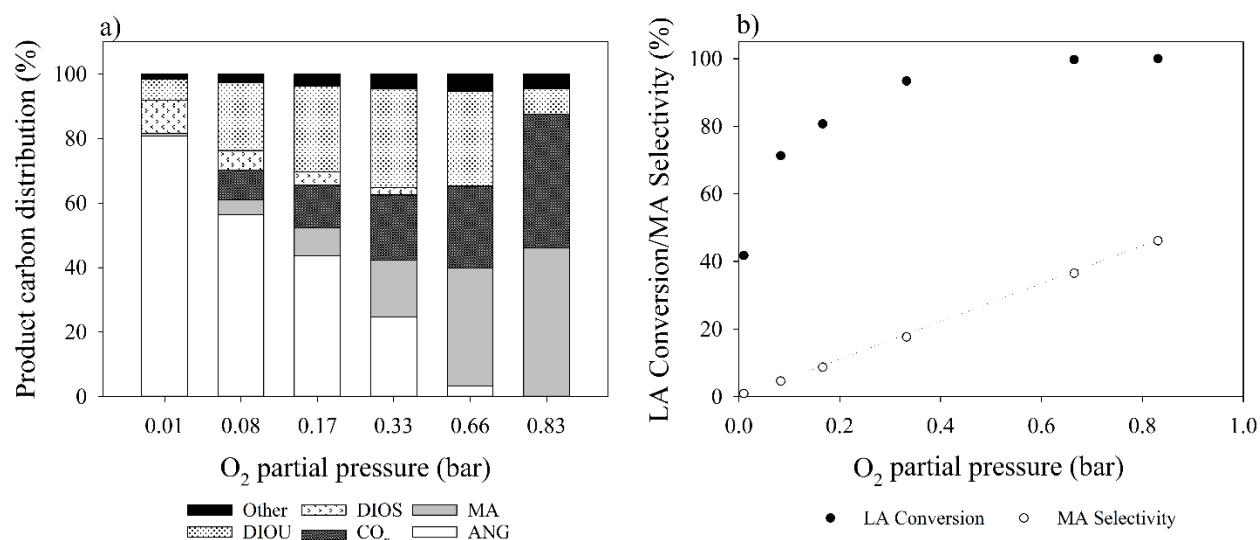
Figure 4 *Influence of O$_2$ partial pressure on LA conversion / MA selectivity. T = 623 K, pLA = 0.016 bar, WHSV = 0.128 min^{-1}*

Even under oxygen lean conditions (0.010 bar O$_2$, O$_2$:LA = 0.62), we observe baseline conversion of LA (Figure 4a). This is attributed to non-oxidative pathways, primarily dehydration, such that ANG comprised 80% of the product carbon distribution. An additional 16% of the product carbon existed as DIO, with DIOS and DIOU recovered in 5:3 molar ratio. It is worth noting that increasing O$_2$ pressure shifts the DIO distribution completely toward the unsaturated product, DIOU, which is consistent with our interpretation that DIOU forms via ODH of DIOS, especially at high temperatures (Scheme 6). LA conversion increases with O$_2$ partial pressure (Figure 4b), and we attribute this to an increase in the rates of irreversible,

oxidative reactions that allow complete consumption of LA, ANG, and DIOS and shift selectivity toward DIOU, MA, and CO_x. Increasing O_2 pressure initially favors DIOU formation, while further increments drive formation of MA and CO_x. Figure 4b illustrates a clear, first order dependence of MA selectivity on O_2 pressure. Since SA, MA, and DIOU all form irreversibly, this enhancement in MA selectivity is likely attributed to a disproportionate increase in the rate of LA oxidative cleavage relative to the rate of DIOS dehydrogenation in response to increases in O_2 pressure, i.e., irreversible oxidative cleavage of LA appears higher order in O_2 than does irreversible ODH of DIOS.

So far, no real claim can be made as to which is the dominant pathway in the conversion of LA to MA. The pathway involving cleavage of the methyl carbon in ANG is supported by the change in selectivity from ANG to MA with increasing temperature, contact time and O_2 partial pressure. Since LA and ANG are likely equilibrated the same can be said for LA, i.e., if one is consumed in a reaction leading to the production of MA the equilibrium will shift at the expense of the other.

3.3.5 Influence of the Metal Oxide Support

Comparison of the performance of all supported catalysts and bulk V_2O_5 is presented in Table 2.

Table 2 *Comparison of LA oxidation over bulk and supported vanadates. DIO includes both DIOS and DIOU*

Catalyst	T (K)	Contact time (min)	Conversion (%)	MA yield (%)	Carbon distribution					MA:CO_x	CB (%)
					ANG	MA	CO_x	DIO	Other		
VO_x/SiO_2	548	1.95	99	50	2	43	36	15	4	1.2	96
VO_x/TiO_2	548	0.39	93	26	3	25	61	8	3	0.4	89
VO_x/Al_2O_3	548	78	98	33	5	27	34	26	8	0.8	100
V_2O_5	548	280	97	18	12	15	21	45	7	0.7	98
VO_x/SiO_2	523	3.9	43	1	83	2	5	8	2	0.5	98
VO_x/SiO_2	548	3.9	100	48	1	44	35	14	6	1.3	88
VO_x/SiO_2	573	3.9	100	71	0	57	37	2	4	1.5	100

At 548 K, VO_x/SiO and VO_x/TiO_2 are significantly more active than $VO_x/\gamma\text{-}Al_2O_3$ and V_2O_5. Both achieve complete LA conversion at contact times below 2 min, whereas complete LA conversions were not achieved until contact times of roughly 80 min over $VO_x/\gamma\text{-}Al_2O_3$ and 300 min over bulk V_2O_5. Comparing selectivities at complete LA conversion, we observe that MA selectivity increases with catalyst identity in the order of $V_2O_5 < VO_x/TiO_2 < VO_x/\gamma\text{-}Al_2O_3 < VOx/SiO_2$. Each material showed comparable selectivities toward ANG (<15%), while the remaining product distribution varied with support identity. Bulk V_2O_5 appears relatively selective toward DIOU, which comprises 45% of the product carbon distribution. This suggests that bulk V_2O_5 facilitates DIOS dehydrogenation to a greater extent than it does LA cleavage. DIOU selectivity decreases over $VO_x/\gamma\text{-}Al_2O_3$ (26%) and further over VO_x/SiO_2 (15%) and VO_x/TiO_2 (8%). Over bulk V_2O_5, $VO_x/\gamma\text{-}Al_2O_3$, and VO_x/TiO_2, carbon selectivity towards CO_x exceeds that of MA, suggesting these materials promote combustion more so than oxidative cleavage. Only VO_x/SiO_2 achieves an $MA:COx$ carbon ratio greater than unity, implying that it is effective at limiting over-oxidation. Since VO_x/SiO_2 appeared to suppress both DIO and CO_x formation, it was further examined. Consistent with results obtained over $VO_x/\gamma\text{-}Al_2O_3$, MA selectivity increases dramatically with temperature over VO_x/SiO_2. At 573 K, we obtained an MA (carbon) selectivity of 57% and a $MA: CO_x$ ratio of 1.54, which corresponds to a molar MA yield of 71%. It is evident that the nature of the support can impact activity and selectivity in this system; however, each support employed here varies in its acid/base character, and the structure and function of VO_x clusters vary strongly with support and VO_x loading. VO_x speciation will be discussed in detail later on, while we will also attempt to shed light on the acidity of the support and how that might play a role in selectivity.

3.3.6 Contrasting Selectivities Between the Oxidative Cleavage of Levulinic Acid and Monofunctional 2-Pentanone

Oxidative cleavage of LA is likely to follow a similar pathway to that of monofunctional ketones, as was outlined earlier in Scheme 7. A number of studies on 2-butanone have shown that selectivity in these reaction is heavily skewed in favor of the oxidative cleavage of the internal enol[29, 33, 34] backed up by electronic calculations showing that the internal enol is by far the most dominant one[37]. In addition, enol formation is governed by Zaitsev's rule[38], stating that the thermodynamic enol will be created with the double bond on the side of the carbon that is more substituted, once again predicting that selectivity will favor the internal enol of any asymmetrical methylketone. A question therefore arises as to the unanticipated selectivity for terminal oxidative cleavage of LA which requires further investigation.

In order to make a preliminary comparison of selectivity, reactant feed was switched from LA to 2-pentanone and the results are presented in Table 3.

Table 3 Comparison of oxidative cleavage rates and C4 selectivities for LA and 2-pentanone on $VO_x/\gamma\text{-}Al_2O_3$

Feed	T (K)	Feed rate $(\mu mol\ min^{-1})$	τ (min)	Conversion (%)	Cleavage rate $(\mu mol\ min^{-1}\ g^{-1})$	C_4 (%)	Carbon Balance (%)
2-pentanone	573	79	7.80	14	22	1	96
2-pentanone	585	79	7.80	49	35	2	96
2-pentanone	598	79	7.80	95	59	3	96
LA	573	79	7.80	99	41	85	90
LA	598	79	7.80	100	50	89	90

Consistent with prior accounts of 2-butanone oxidation, during 2-pentanone oxidation, the product stream was overwhelmingly comprised of species resulting from cleavage of the internal C-C double bond. This pathway yields an equimolar mixture of acetic acid and propionaldehyde.

Our experimental findings, in good agreement with the literature [33, 34, 37], point to the internal or thermodynamic enol intermediate being the more stable one. During the oxidation of levulinic acid however, the terminal enol (forming at the C_4-C_5 position) is the dominant of the two resulting in high selectivities of MA. Indeed, over VO_x/γ-Al_2O_3 at 598 K (Conversion for both 2-pentanone and LA > 95%) 2-pentanone terminal cleavage product selectivity was a mere 3% while for LA it was 89%. The difference between LA and 2-pentanone is found in the carboxylic functionality of LA and it seems trivial that the contrasting selectivities should be attributed there. It is not clear however, if the carboxylic group influences selectivity just by changing the structural property of the molecule, i.e. creating steric effects, or by engaging in bond breaking/making, as is the case for the dehydration of LA to angelicalactones. It seems plausible that the carboxyl group plays an important factor in determining the rates of reaction by rendering the oxidative cleavage via the internal enol intermediate less likely. In this context, a broader screening of monofunctional ketones and ketoacids could prove valuable in the quest for deciphering the mechanism of oxidative cleavage in LA.

4 Mechanistic Aspects on the C-C Oxidative Cleavage of Simple Ketones

4.1 Introduction

LA is a solid at 298 K and when heated, especially over acid sites, dehydrates readily to ANG. Furthermore, major oxidation products such as MA and DIO have even lower vapor pressures than LA and are solids at 298 K. In order to understand selectivity trends we switch from bifunctional LA to monofunctional ketones, which are advantageous as feed molecules over LA for the following reasons; they tend to have much higher vapor pressures than LA and thus, are easier to vaporize. In addition, oxidative cleavage products are anticipated to be primary products rather than MA, which we have shown to be a secondary product, and finally, they do not tend to follow non-oxidative pathways unlike LA, which means that we can better control conversion. An experiment was designed to examine intrinsic oxidative cleavage rates of a number of different ketones with varying chain lengths, position of their carbonyl group and alkyl substitutions. In addition, ketoacids other than LA were also considered.

4.2 Materials and Methods

For the following experiments a new reactor was built (Scheme 11) that further allows gas phase analysis of all products including diacids through a simple and inexpensive design. Problems with temperature readout inside the reactor were also addressed by placing a thermocouple downstream from the catalytic bed. In addition, a new VO_x/Al_2O_3 was synthesized employing a different synthesis method. In detail, the catalyst was prepared by the incipient wetness method. γ-Al_2O_3 (Strem, 95%) was calcined at 723 K for 4 hours under 50 sccm of air (Airgas, Ultra Zero) prior to impregnation. A hot slurry of an ammonium metavanadate (Sigma, 99.5%) and oxalic acid (Acros, 99%) mixture (1:2 molar ratio) was prepared and the appropriate volume was

used to wet the support. The resulting wet powder was left in an oven at 338 K for 16 hours to

ensure the full removal of water. The catalyst was then calcined for 4 hours at 723K under 50

sccm of air (Airgas, Ultra Zero) and sieved to obtain a particle size of 45-90 μm.
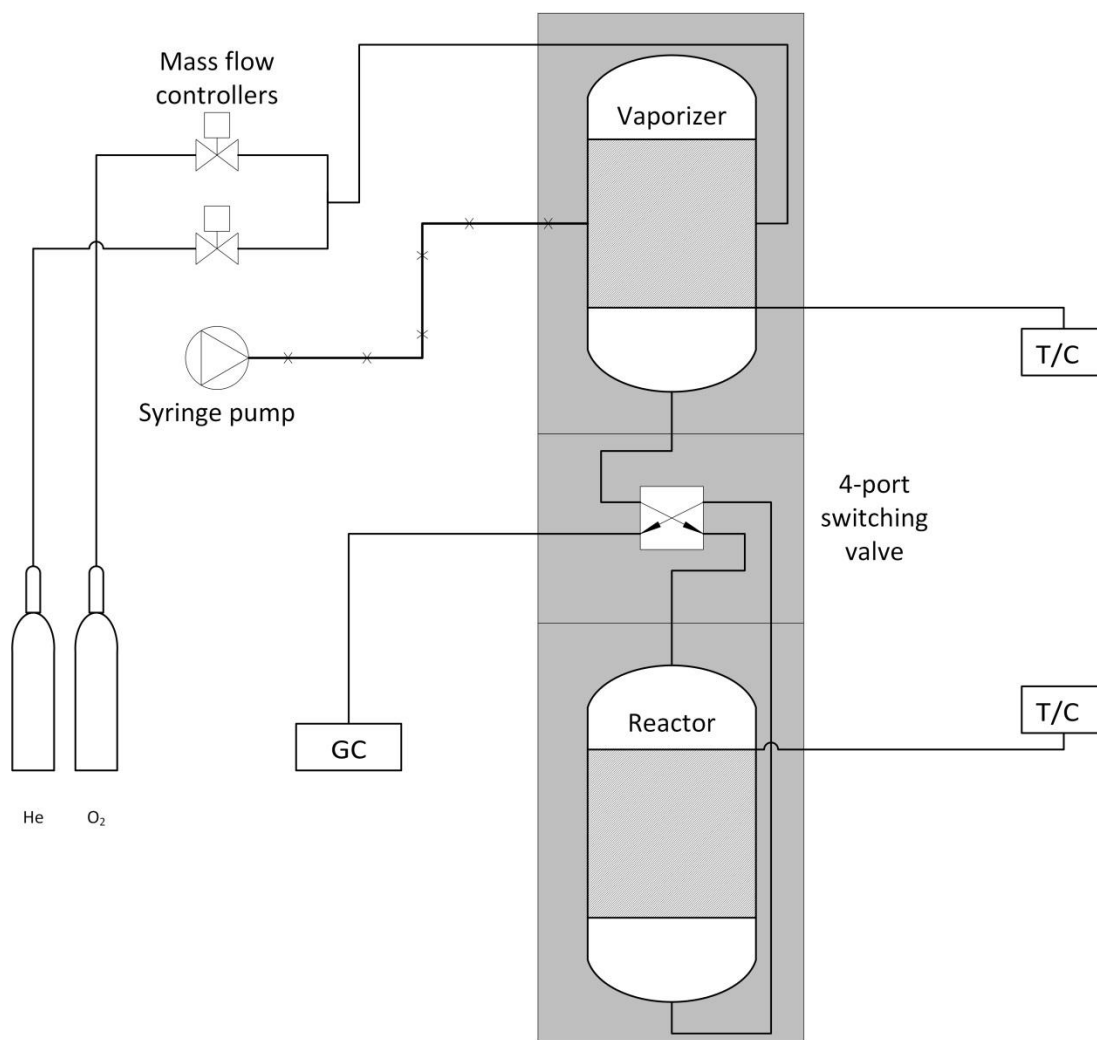
Scheme 11 *Redesigned oxidation reactor*

Acetone (Acros, 99%), 2-butanone (Acros 99%), 2-pentanone (Acros, 99%), 3-pentanone

(Sigma 99%), 2-hexanone (Acros 98%), 2 hepatanone (Acros, 98%), 2-octanone (Acros, 99%),

3-octanone (Alpha Aesar, 98%), 4-octanone (TCI, 98%), 3-methyl-2-pentanone (Sigma 97%), 4-

methyl-2-pentanone (Sigma, 99%), 3,3-dimethy-2-pentanone (Oakwood, 96%), 3-isopropyl-2-pentanone (MP Biomedicals), 3,3-dimethy-2-butanone (Alpha Aesar, 97%), 4,4-dimethyl-2-pentanone (Acros, 99%), levulinic acid (Acros, 98%) and 4-acetylbutyric acid (Alpha Aesar, 97%) were used as feed molecules. Acetic acid (Acros, 98%), propionic acid (Acros 99%), butyric acid (Acros 99%), valeric acid (Acros, 99%), Hexanoic acid (Acros, 99%), heptanoic acid (98%, Acros), 2,3-dimethylbutyric acid (Acros, 99%), 2-methylbutyric acid (Sigma, 98%), isobutyric acid (Acros 99%), maleic anhydride (TCI, 99%), glutaric acid (Acros, 99%) acetaldehyde (Sigma, ≥99.5%), propionaldehyde (Acros, 99%), butyraldehyde (Acros, 99%) valeraldehyde (Acros, 98%), hexanal (Alpha Aesar, 98%), CO (Airgas, 1%, 1% Ar, balance He) and CO_2 (Airgas, 1%, 1% Ar, balance He) were used for calibration of analytical instruments. Water was purified in house by sequential reverse osmosis, UV oxidation, and double ion exchange to >18.2 MΩ·cm (Spectrapure). He (Airgas, Ultra High Purity) and O_2 (Airgas, Ultra High Purity) were used as diluent and oxidant during reactor operation. Air (Airgas, Ultra Zero) was used for ex-situ calcination of all catalyst samples. 58 mg of the supported catalyst were mixed with 143 mg of quartz (45-90 μm) to act as a diluent and ensure uniform heat distribution and was put in an upflow ¼" stainless steel tubular reactor. The catalyst bed was held halfway through the tube between two pieces of quartz wool. The bottom of the tube was filled with quartz chips to ensure uniform mixing and minimize the dead volume of the reactor. Positioned downstream of the catalyst and right above the top quartz wool plug, a thermocouple was used to monitor the temperature in the tubular reactor as close to the catalytic bed as possible. An in house built tubular furnace was used to heat the reactor. Prior to each experiment, the catalytic reactor was calcined at 773 K for 4 hours before cooling down to reaction temperature. A preheated mixing section was held at a temperature of 393 K for the ketone experiments and at

433 K for the ketoacids, while separate feeds of the reactant were introduced using a syringe pump (Cole Parmer Series 100) and a gas stream consisting of O_2 and He (controlled by mass flow controllers, Brooks Model 5850S), were preheated and introduced to the mixing stage. The flowrates of ketones or keto-acids, O2, and He were adjusted to achieve the desired partial pressures. The entire delivery system was heat traced, in such way as to ensure that the partial pressures of all reagents were always held well below their respective vapor pressures to prevent condensation. The gaseous mixture was subsequently introduced into the reactor. All temperatures were monitored with K-type thermocouples (Omega) and controlled using PID controllers (Series 16A, Love Controls). At the exit of the catalytic reactor, the gaseous effluent was kept at high enough temperature to avoid condensation and was sent to an HP 5890 gas sampling chromatograph equipped with two split/splitless inlets and dual FID detectors. For the separation and quantification of C_4 and C_5 diacids, a Restek Rtx-1701 column was employed. An Agilent HP-INNOWAX column was used for the remainder of the analysis. The effluent was also sampled in tedlar bags and directed to a second gas sampling HP-5890 chromatograph equipped with a packed column (Restek ShinCarbon ST Micropacked) where CO and CO_2 were quantified via TCD response relative to a helium reference. Qualitative product identification was achieved using an Agilent 7890 GC-MS equipped with an Agilent 5975C MS detector and an HP-INNOWAX column.

Prior to each experiment, a steady state rate of 2-pentanone oxidative cleavage was established and used as reference. Typically, after contacting a different ketone or ketoacid on the catalyst, the feed was switched back to 2-pentanone to measure any loss in activity. For consistency in comparing production rates, wherever significant loss of activity ($\geq 5\%$) was recorded, rates were corrected accordingly by fitting a simple first order deactivation model. The catalyst used

was found to be fully regenerable through numerous reaction/regeneration cycles (>10) and was used for all of the reactions reported herein. For all experiments, the partial pressure of the reactant was always kept constant at 14.3 torr, while the weight hourly space velocity (WHSV) was also kept constant at 0.272 min^{-1}.

For all methylketones, internal cleavage rates were measured by rates of production of acetic acid, rather than the aldehyde counterpart. The aldehydes should be produced at identical rates as acetic acid; however, some of the aldehydes will undergo facile oxidation to their respective carboxylic acids or other cleavage products and make the quantification of rates more complex. Acetic acid is always a common product of internal oxidative cleavage across different methylketones and thus, constitutes the only reliable descriptor of internal cleavage rate. Terminal cleavage rates of methylketones were measured by rates of production of the corresponding carboxylic acid. The rate of the C_1 product resulting from terminal oxidative cleavage was not taken into account as it is possible that C_1 oxidation products, primarily COx, result from over-oxidation of some of the species that are in contact with the catalyst.

4.3   Building a Simple Mechanism to Understand Selectivity in C-C Oxidative Cleavage

To facilitate the selectivity discussion there is a need to identify a simple reaction mechanism for ketones over vanadium oxide catalysts. Oxidation reactions over vanadium oxides usually proceed through the Mars Van Krevelen mechanism[39]. During the catalytic cycle, fully oxidized supported vanadium participates in a series of steps involving the oxidation of the reactant by the loss of lattice oxygen atoms resulting in the reduction of the vanadium center. The cycle is completed by the release of the product and the repletion of oxygen vacancies by molecular oxygen.
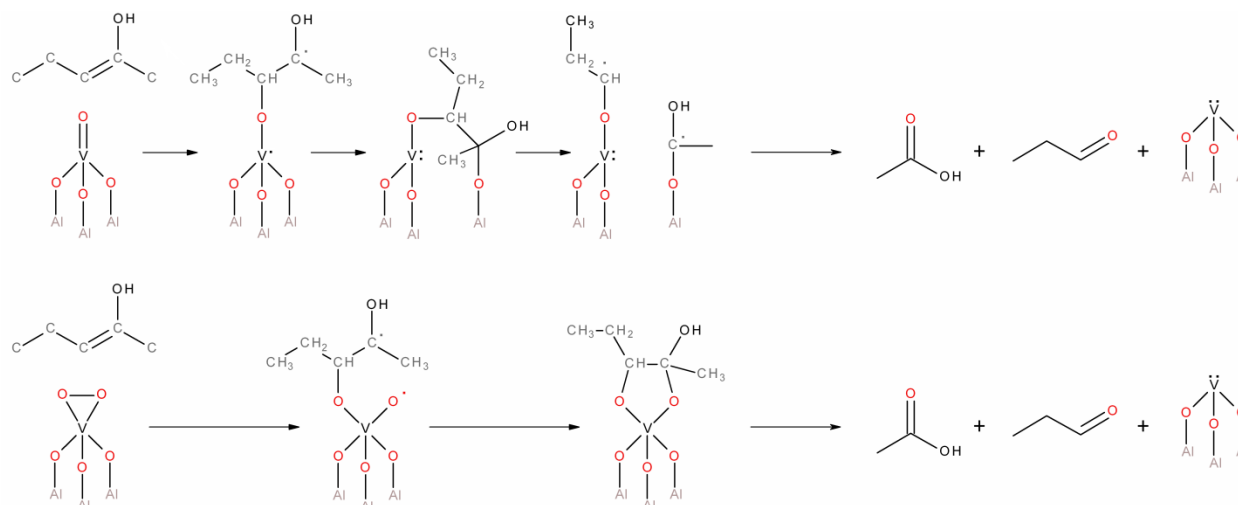
Scheme 12 Two p*ossible pathways for the oxidation of the internal enol form of 2-pentanone over vanadyl or peroxo-vanadate centers*

Seiyama et al. [27] suggested the oxyhydrative mechanism for the cleavage of olefins, involving a step of hydration of the olefin to the corresponding alcohol followed by the oxidation of the alcohol to the corresponding ketone. McCullagh et al. [32-34] provided a detailed mapping of the various pathways of 2-butanone oxidation over vanadium phosphorus oxide [33, 34]. In this scheme of different pathways, the one that leads to the C-C cleavage proceeds through an enol intermediate. More recently, Liu et al. simulated activation barriers for several pathways involving the oxidation of propylene over vanadium oxide supported on silica[40]. Both a vanadyl center and a peroxo-vanadate center were considered as the catalytic active sites. Based on all the above, Scheme 12 presents possible pathways for the oxidation of one of the enol forms of 2-pentanone over vanadyl or peroxo-vanadate centers. The enol formation is likely acid or base catalyzed. In the presence of the peroxo-vanadate center, the enol can coordinate with both oxygen atoms and form a vanadate ester which can cleave and further release acetic acid and propionaldehyde. In the case of the vanadyl oxygen, an extra oxygen is required and so the enol is shown to coordinate with a V-O-M bridging oxygen. Again, the O-C-C-O breaks to

release products of oxidative cleavage. The oxygen depleted vanadium center is oxidized through molecular oxygen, thus completing the Mars Van Krevelen catalytic cycle in both scenarios. As with the reaction pathways, these possible mechanisms are proposed based on literature reviews and are by no means conclusive. In fact, we are yet to identify which oxygen atoms participate in the reaction, an important piece of information in order to predict the correct mechanism. In addition, a number of characterization tools are required in order to assess the catalytic surface and vanadium speciation especially with different supports or different vanadium loadings, something that will addressed later on. Finally, since ketone oxidative cleavage proceeds with the insetion of two oxygen atoms, a pair of vanadium centers is likely required rather than a single surface bound vanadium species, we do however believe that for the following discussion the above scheme will be sufficient.

4.4 Results and Discussion

4.4.1 Effect of Chain Length on Cleavage Rates and Selectivities

We begin by probing the effect of chain length on ketone oxidative cleavage and for this purpose, rates and selectivities of oxidative cleavage were measured for linear methylketones (C_3-C_8) at 468 K. All linear methylketones showed above 90% selectivity towards the oxidative cleavage of the internal enol. Cleavage rates are reported in Table 4 (entries 1-9), while Figure 5 depicts selectivities for all linear methylketones. Oxidative cleavage rates appear to hit a maximum at 13.9 µmol g^{-1}min^{-1} with 2-butanone, while for the C_6, C_7 and C_8 methylketones, cleavage rates are invariant with chain length.

Table 4 *Total oxidative cleavage rates and selectivities to internal/terminal cleavage for all ketones/keto-acids*

Entry	Feed molecule	Total cleavage rate ($\mu mol \ g^{-1}min^{-1}$)	Selectivity to internal cleavage (%)	Selectivity to terminal cleavage (%)
Linear ketones (T=468 K), p_{ketone}=0.019 bar, WHSV=0.272 min^{-1}				
1	Acetone	5.7	n/a	
2	2-butanone	13.9	97	3
3	2-pentanone	10.0	91	9
4	3-pentanone	10.1	n/a	
5	2-hexanone	5.7	100	0
6	2-heptanone	6.0	100	0
7	2-octanone	6.6	100	0
8	3-octanone	5.0	59	41
9	4-octanone	6.5	52	48
Branched methylketones (T=468 K) , p_{ketone}=0.019 bar, WHSV=0.272 min^{-1}				
10	3,3-dimethyl-2-butanone	2.2	93	7
11	3-methyl-2-pentanone	83.7	100	0
12	3-isopropyl-2-pentanone	14.5	100	0
13	3,3-dimethyl-2-pentanone	5.7	96	4
14	4-methyl-2-pentanone	6.8	100	0
15	4,4-dimethyl-2-pentanone	5.9	86	14
Keto-acids (T=550 K) , p_{ketone}=0.019 bar, WHSV=0.272 min^{-1}				
16	2-pentanone	153.4	92	8
17	3,3-dimethyl-2-butanone	20.9	63	37
18	3,3-dimethyl-2-pentanone	17.3	74	26
19	4,4-dimethyl-2-pentanone	101.0	73	27
20	Levulinic acid	26.8	26	74
21	Acetylbutyric acid	26.7	51	49

The symmetric 3-pentanone was also fed to the reactor (Entry 4) and the rate of cleavage was identical to the total cleavage rate from 2-pentanone. We can conclude that oxidative cleavage selectivities are invariant with ketone chain length and that the same argument could be made for ketone chain length.

4.4.2   Effect of Carbonyl Position on Cleavage Rates and Selectivities

Next task was to probe the effect of the position of the carbonyl group on oxidative cleavage rates and selectivities. To achieve this, all of the three different linear octanone molecules were tested. Rates also appear to be identical between 2-, 3- and 4-octanone; however, shifting the carbonyl group strongly affects the cleavage selectivity. For 3-octanone, both α-hydrogens seem to participate equally in the enolization reaction to promote two stable enol forms. In comparison with 2-octanone, both α-carbons are equally substituted suggesting that Zaitsev's rule applies for this type of transformation. Once we further move the carbonyl to the 4 position, selectivities become statistically indistinguishable reinforcing the above. Oxidative cleavage of 4-octanone should result in an equimolar mixture of butyric acid and butyraldehyde. Rates of butyraldehyde production were substantially lower than butyric acid, while rates of butyric acid formation were higher than the total rate of cleavage from both 2- and 3-octanone. There is no apparent reason for this total rate difference and as we notice from entries 3-4 and 7-8 from Table 4, total rate of oxidative cleavage does not appear to vary with respect to the position of the carbonyl group. Thus, we speculate that butyraldehyde further oxidizes to butyric acid which leads to this disparity in the rates. To remedy this, the rates of C_4-C_5 cleavage reported here are an average of the rates of production of butyric acid and butyraldehyde. It appears that changing the position of the carbonyl position on a methylketone gravely affects selectivity but total cleavage rates remain unaffected.
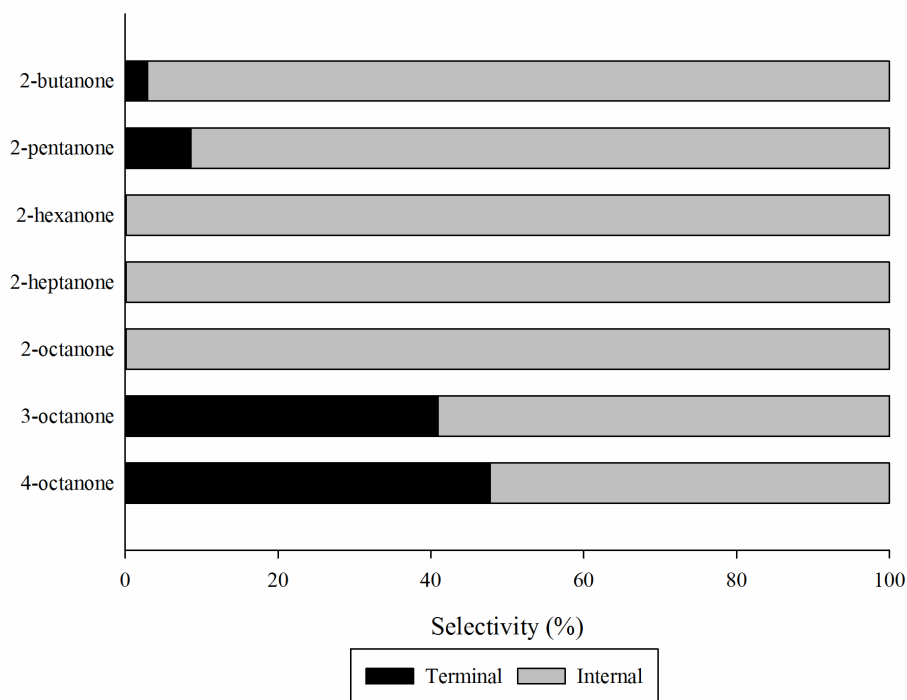
Figure 5 *Selectivities for the oxidative cleavage of linear methylketones (T=468 K, p$_{ketone}$=0.019 bar, WHSV=0.272 min^{-1})*

4.4.3 Effect of Alkyl Substitutions on Cleavage Rates and Selectivities

In an attempt to force the selectivity of methylketones toward the terminal cleavage, we turned our attention to ketones with a variety of alkyl substitutions. 2-pentanone was yet again considered as the base case and once again, the temperature in the bed was kept at 468 K. Table 4 (entries 10-15) presents a diverse range in total rates, while Figure 6 depicts differences in selectivities.

Rates for oxidative cleavage of 3-methyl-2-pentanone (84 μmol g^{-1}min^{-1}) were almost an order of magnitude higher than that of 2-pentanone (10 μmol g^{-1}min^{-1}). It is apparent that the change in substitution of the α-carbon is responsible for this jump in rate. Trying to interpret this high rate, we turn to the reaction mechanism and specifically to the third carbon, now a tertiary instead of a

secondary. We speculate that the rise in rate is a direct result of a more stable intermediate resulting from the transition from a secondary to a tertiary carbon, thus lowering the energy of the transition state for the cleavage of 3-methyl-2-pentanone. Once we replace the methyl group with an isopropyl group (3-isopropyl-2-pentanone), we still observe a higher cleavage rate (15 μmol g^{-1}min^{-1}) than 2-pentanone but much lower than that for 3-methyl-2-pentanone. This is not very surprising as the addition of the bulky isopropyl group might be creating steric effects that hinder the rate of oxidative cleavage.
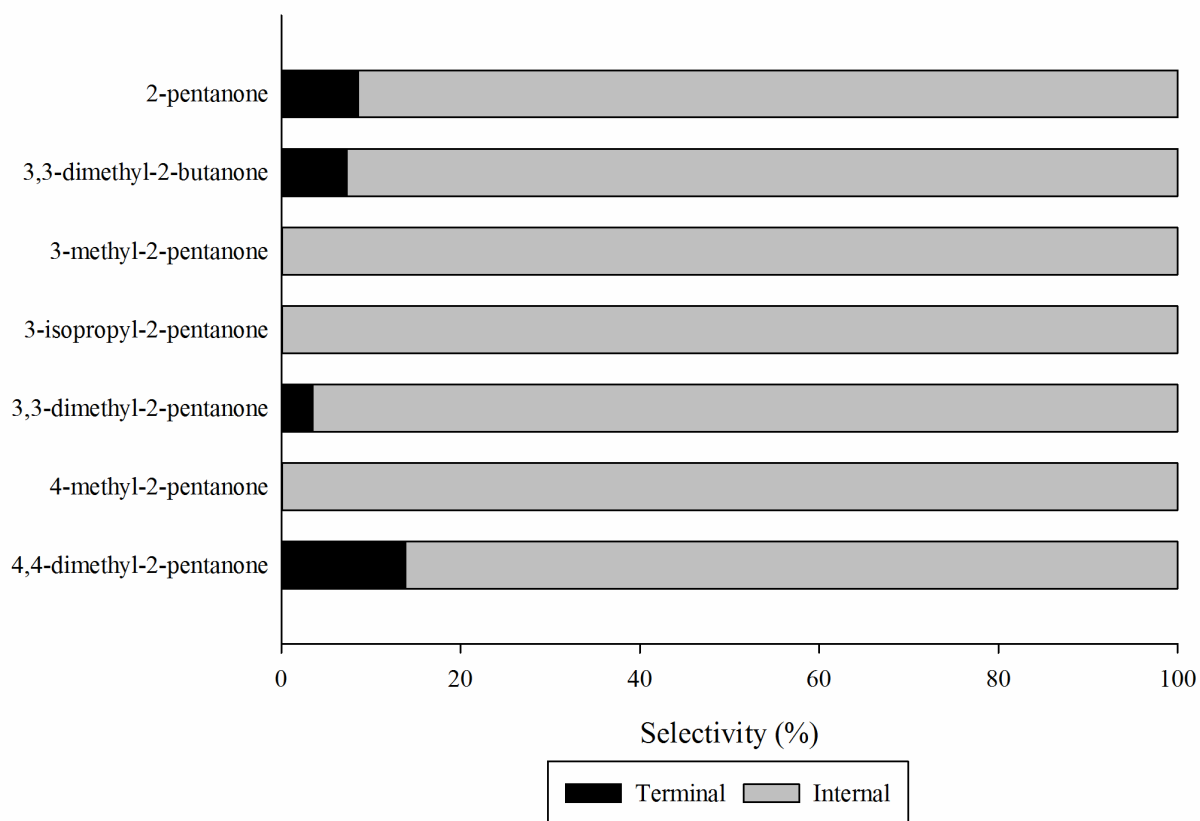
Figure 6 *Selectivities for the oxidative cleavage of alkyl-substituted methylketones (T=468 K, p_{ketone}=0.019 bar, WHSV=0.272 min^{-1})*

3,3-dimethyl butanone (pinacolone) and 3,3-dimethyl-2-pentanone were initially used for control experiments, i.e. molecules that cannot form internal enols, due to the lack of α-hydrogens and thus cleavage should exclusively occur on the terminal position. Surprisingly, in both cases we observed amounts of acetic acid in the reactor effluent. Apart from traces of contaminants we believe that a rearrangement including an alkyl shift is probably responsible for the acetic acid rates that we observed. More specifically, pinacolone can result in a rearrangement of pinacol (2,3-dimethylbutane-2,3-diol) in a mechanism known as the pinacol rearrangement[41].
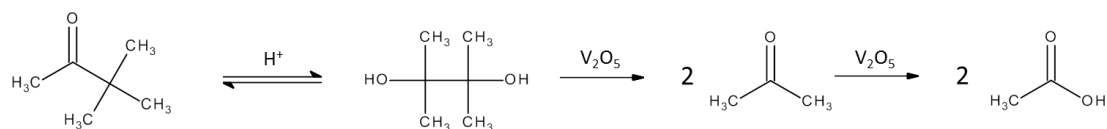
Scheme 13 *Reverse pinacol rearrangement and subsequent oxidative cleavage*

All steps in the pinacole rearrangement mechanism are reversible so it is very likely that a rearrangement of pinacolone under reaction conditions can yield the diol which can undergo oxidative cleavage yielding 2 equivalents of acetone (Scheme 13). Further oxidative cleavage of acetone will yield acetic acid. We postulate that a very similar pathway would produce acetic acid for the oxidation of 3,3-dimethyl-2-pentanone. This, however, is not a realistic pathway for any other ketone/keto-acid fed to the reactor due to the lower substitution of the terminal carbon. Low rates were recorded for terminal oxidative cleavage on both control molecules. It is possible that terminal cleavage (i.e. the stable formation of the terminal enol) requires higher temperature to achieve, a notion reinforced by the fact that significant terminal oxidative cleavage of LA to MA does not occur below 523 K.

In addition, 4-methyl-2-pentanone and 4,4-dimethyl-2-pentanone were fed to the reactor. For the 4,4-dimethyl-2-pentanone a significant increase in selectivity for terminal cleavage was observed. Of all the ketones fed, the latter bears more resemblance to LA exhibiting the bulky t-butyl group, similar to the carboxylic group in LA. Increase in terminal selectivity for 4,4-dimethyl-2-pentanone implies that steric effects might be in play.

4.4.4   Effect of Temperature on Cleavage Rates and Selectivities of Ketones and Ketoacids

To investigate all of the above, we focused to some of the more promising ketones. We included 2-pentanone as our referernce, while 3,3-dimethyl-2-butanone, 3,3-dimethyl-2-pentanone and 4,4-dimethyl-2-pentanone were also considered. This time the reactor was operated at a temperature of 550 K in order to increase rates of terminal oxidative cleavage. Rate data is presented in Table 4 (entries 16-21) and terminal cleavage selectivities for ketones and ketoacids are plotted in Figure 7. Reaction conditions are far from differential at this temperature, as conversions range from 20-50% depending on the feed and thus, data from this experiment is meant to give us a general idea of selectivity trends but in no way should it be considered for kinetic analysis. Total oxidative cleavage rate for 2-pentanone increased to 153 μmol g^{-1}min^{-1} almost a 15 fold increase from the oxidative cleavage rates at 468 K; however, selectivity towards terminal cleavage remained the same.
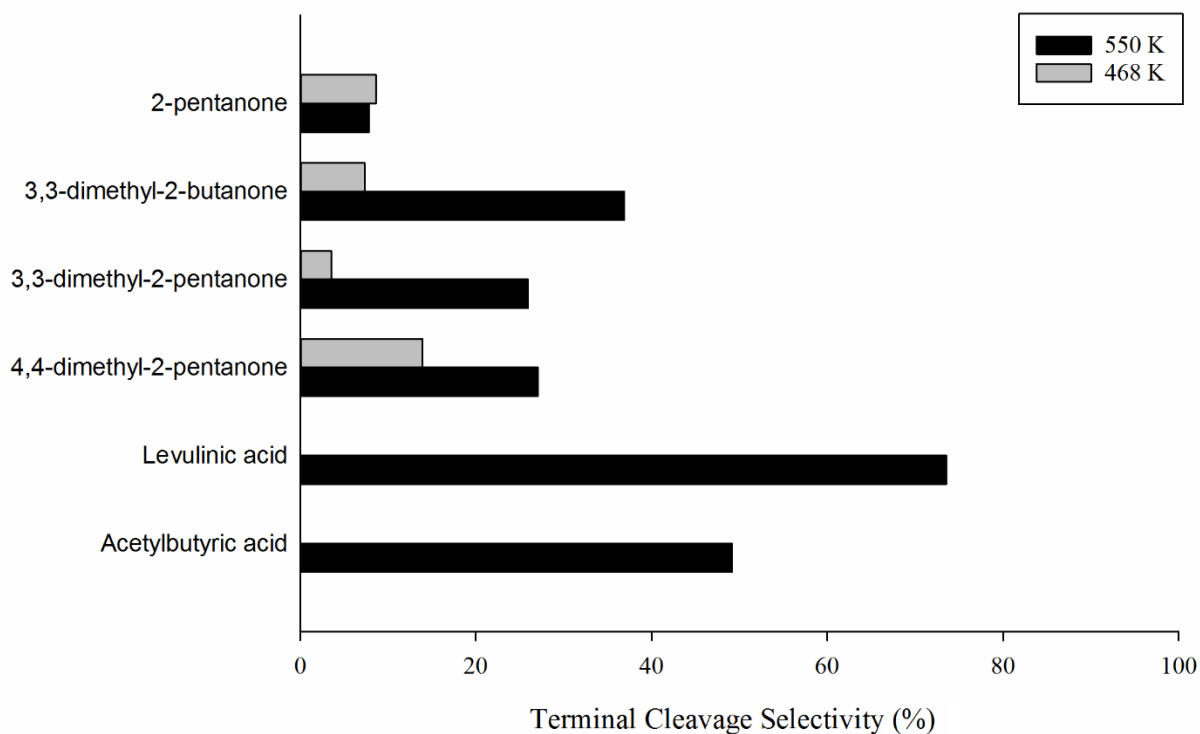
Figure 7 *Selectivity for the oxidative cleavage of the terminal carbon in ketones and ketocaids (T=550 K, p_{ketone}=0.019 bar, WHSV=0.272 min^{-1})*

This implies that higher temperatures equally promote the two cleavage pathways in the case of 2-pentanone. Internal cleavage rate for 3,3-dimethyl-2-butanone and 3,3-dimethyl-2-pentanone roughly doubled, while terminal cleavage rates went up by at least two orders of magnitude resulting in significant increase for terminal cleavage selectivity. This reinforces our previous speculation that a different mechanism is responsible for the production of acetic acid from the above molecules. Total oxidative cleavage rates for 4,4-dimethyl-2-pentanone increased in the same fashion as for 2-pentanone, though selectivity for terminal cleavage almost doubled. This disparity between 2-pentanone and 4,4-dimethyl-2-pentanone again points to the bulky t-butyl group and resulting steric effects. If this is true, a decrease in terminal selectivity should result from extending the straight carbon chain. To validate this we turned to keto-acids and,

specifically, LA and 4-acetylbutyric acid (5-oxohexanoic acid). The shorter acetoacidic acid (3-oxobutanoic acid) was not considered because malonic acid, which results from the terminal cleavage of acetoacetic acid, decarbonylates readily to acetic acid and CO_x which makes accurate rate and selectivity measurements very challenging. Indeed, while LA shows 74% selectivity towards terminal cleavage, for the longer 4-acetylbutyric acid terminal selectivity drops to 49%. Interpretation of this selectivity is nontrivial because, as with LA, 4-acetylbutyric acid also forms lactones and specifically the 6-methyl-3,4-dihydropyran-2-one (Scheme 14), a six membered ring whose oxidative cleavage could yield glutaconic acid (pent-2-enedioic acid) or its anhydride.
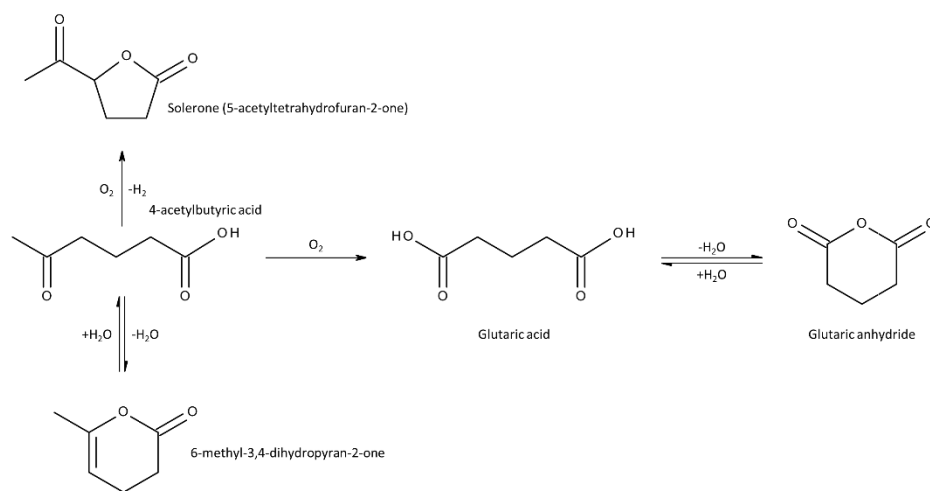
Scheme 14 *4-acetylbutyric acid oxidation pathways*

We do however observe glutaric acid or glutaric anhydride as the terminal cleavage product which might indicate that the reaction pathway is not mediated through the formation of the lactone; rather it is possible that the open chain cleaves similarly to simple methylketones. A question arises here as to why glutaric anhydride does not undergo oxidative dehydrogenation to glutaconic acid as SA does in pathway 2 of Scheme 6 towards MA. This step of SA

dehydrogenation is included in the mechanism to explain the formation of MA through the oxidative cleavage of the methyl carbon in LA. If MA though is produced directly from oxidative cleavage of the methyl carbon of angelicalactone, this step would not be necessary to explain the products. Furthermore, as we noted previously, ODH is not very favorable below 600 K and so it is possible that glutaric acid is the final product without undergoing any further reactions. If ketoacid oxidative cleavage is mediated through a lactone intermediate then in the case of 4-acetylbutyric acid, a simple question arises: why is glutaconic acid/anhydride not among the recovered products as would be anticipated by the cleavage of the methyl group in the 6-membered ring lactone. This could be attributed to the fact that the 6-membered lactone that forms from the dehydration of 4-acetylbutyric acid is not thermodynamically favorable and the equilibrium favors the acid. While it is usually assumed that six membered ring structures will be more stable due to their ability to rearrange in very stable conformations (chair, boat), when an exocyclic double bond is present, 5-membered lactones are far more stable than their 6-membered counterparts which tend to ring open and/or polymerize[42]. Additionally, GC-MS analysis reveals that the dominant lactone form is solerone or 5-acetyltetrahydrofuran-2-one, which is a 5-membered ring lactone, and thus, a more stable configuration (Scheme 14), so keto-acids will tend to arrange in 5-membered lactone rings if possible. This lactone, however, is not the result of dehydration but probably a result of a dehydrogenation pathway from 4-acetylbutyric acid.

To summarize, terminal cleavage rates at 550 K across 2-pentanone, 4,4-dimethyl-2 pentanone and the two keto-acids average 12 to 27 µmol $g^{-1}min^{-1}$, while internal cleavage rates average between 7 and 141 µmol $g^{-1}min^{-1}$. This data suggests that selectivity shifts because we are likely suppressing the formation of the internal enol rather than promoting the formation of the terminal

one. Terminal cleavage rates for 3,3-dimethyl-2-butanone (7.7 μmol g^{-1}min^{-1}) and 3,3-dimethyl-2-pentanone (4.5 μmol g^{-1}min^{-1}) are still low compared to the other ketones and keto-acids, something that could again be explained by steric effects, caused by the two methyl groups adjacent to the carbonyl, increasing the energy of the transition state. To increase our understanding of the mechanism of oxidative cleavage, we feel it is necessary to understand the interactions that simple ketones and ketoacids have with the catalytic surface of the supported vanadium oxides.

4.5   FTIR Study on the Interaction Between γ-Al$_2$O$_3$ and Adsorbed Acetone, Acetic Acid and LA

4.5.1   Introduction

Although it is evident that cleavage selectivity in ketones is controlled by the stability of the enol, the reasons for the disparity between 2-pentanone and LA or 4-acetylbutyric acid are still elusive. The only difference is the added carboxyl group and, in order to take a deeper look into the sterics argument, we shifted our attention to the catalytic surface and, in particular, to how carboxyl groups interact with it. For this purpose we tested how the previously synthesized VO$_x$/γ-Al$_2$O$_3$ along with pure γ-Al$_2$O$_3$ reacts to dosing of simple ketones, acids and ketoacids under an infrared beam. We chose the simplest ketone (acetone) and acetic acid along with LA in order to probe the interactions they have when they come in contact with the catalyst surface.

4.5.2   Materials and Methods

For each experiment, approximately 20 mg of $VO_x/\gamma\text{-}Al_2O_3$ catalyst were pressed into a pellet in

a Specac M26855 pellet press. The pellet was secured on the pellet holder which was placed in a

vacuum tee. This vacuum tee was especially designed in house and is shown in Scheme 15.
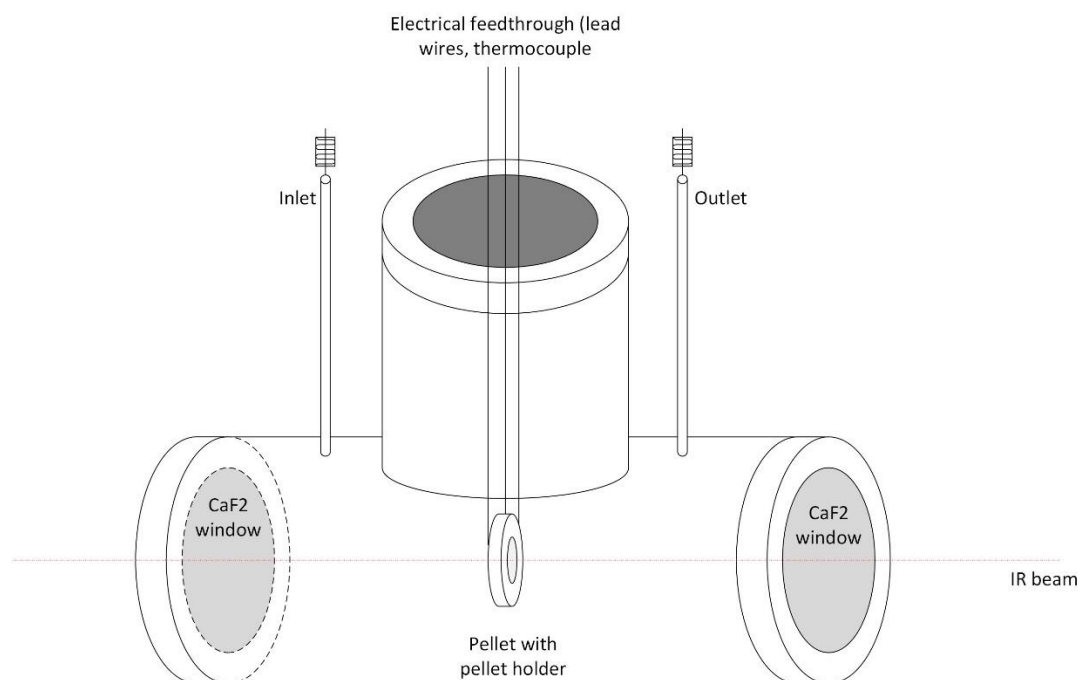
Scheme 15 *IR cell schematic*

Pellet temperature was controlled via two cartridge heaters and a type K thermocouple connected

to a Love Series 16A via a feedthrough vacuum fitting. IR transparent CaF_2 windows were

secured with an o-ring setup on two vacuum fittings allowing for the IR beam to hit the pellet

unobstructed. Two ¼" tubes were welded on the tee body, to allow for dosing and purging, while

two ¼" bellows valves were used to pressurize the whole cell if needed. The whole tee was

positioned inside a Nicolette 6700 (DTGS detector) FTIR and was fixed to the bottom plate.

Prior to positioning the pellet in the holder, the cell was purged with a He stream (Airgas, UHP)

that was passed through a liquid nitrogen trap followed by a moisture trap to ensure the removal of any water vapor. Subsequently, the temperature was raised to 423 K and kept there until the background signal on the FTIR was stabilized. This was used as the background spectrum and was thus subtracted from all future spectra taken during a single experiment. The pellet was then placed in the pellet holder and was left to calcine at 723 K for 4 hours under 100 sccm of air which was passed through a purge gas generator to remove any water and CO_2. The cell was left to cool down to 323 K. The outlet bellows valve was then closed and the whole cell was pressurized to a few atmospheres to not allow any room air to creep into the pellet. The cell was then moved into the oven of an HP 5890 GC where the inlet was reconnected to the same air supply. The outlet was guided to a 6-port gas sampling valve where gas injections were performed in order to analyze the effluent of the cell. A micro dosing procedure was employed to bring the reagents in contact with the pellet surface. 2-5 mL of reagent [Acetone (Acros 99%), Acetic acid (Acros 99.8%) and Levulinic acid (Sigma 98%)] was placed in a cylindrical glass bubbler which was placed in an acetone/liquid nitrogen cryo bath at a temperature of 179 K with the exception of LA, where the bubbler was kept at 298 K. Dry air from the purge gas generator was passed through the bubbler and the effluent was guided in the 5890 GC oven through one of the inlet port openings. The oven temperature was kept at 373 K throughout the dosing stage and the effluent was periodically sampled. Once the concentration of the effluent reached a steady value, flow was diverted from the bubbler and the cell was purged with dry air until there was no response from the FID detector, indicating that no appreciable amount of reagent was desorbing from the pellet. The oven was then cooled at 323 K, the bellows valves were sealed and the cell was moved back to the FTIR where it was left to further purge under dry air. Temperature was

ramped to 573 K at a rate of 3 Kmin[-1] and spectra were collected at 323, 373, 423, 473, 523 and 573 K.

4.5.3   Results & Discussion

Surface interactions of all probe molecules with gamma alumina and $VO_x/\gamma-Al_2O_3$ are presented in Figure 8. Together with all spectra taken we overlay, on top of each graph, the spectrum of a pure liquid film of all probe molecules. Spectra from all probes show a distinct peak at 1710 cm^{-1} which is associated with the carbonyl C=O stretch [43]. It is immediately apparent by looking at Fig. 9a and 9b that the interaction between acetone and either pure alumina or VO_x/Al_2O_3 is occurring through the carbonyl group due to the shift of the band assigned to ν(C=O) from 1716 cm^{-1} in pure acetone to 1695 cm^{-1} in gamma alumina and 1682 cm^{-1} in $VO_x/\gamma-Al_2O_3$. A band arises at 1620 cm^{-1} which gives place to new sharp feature at 1595 cm^{-1} as temperature increases. This band indicates the coordination of acetate species as it is associated with the acetate asymmetric stretch ν_{as}(COO[-]) at 1590 cm[-1][43]. We should also expect a band for the symmetric stretch, usually observed at 1470 cm^{-1} for alumina bound acetone. We do observe a band at 1452 cm^{-1} but we cannot be certain that acetone cleaves to acetic acid, especially at temperatures as low as 323 to373 K. Furthermore, acetone is known to transform to condensation products such as mesityl oxide (MSO) and diacetone alcohol (DAA), which is an intermediate for the production of MSO [44] over gamma alumina. Since this experiment was meant to probe the interactions between support and reaction species, it was performed under an oxygen rich stream to facilitate oxidation of surface bound species. By doing so we certainly favor oxidation pathways and we anticipate seeing oxidative cleavage products, but we can certainly not rule out interactions of condensation products with the alumina surface. Furthermore, when acetone is

dosed on VO_x/γ-Al_2O_3, we see a clear transition from a broad peak at 1660-1680 cm^{-1} to the two bands at 1455 and 1556 cm^{-1}, which are characteristic of acetate formation on metal oxides[45]. The spectrum of acetic acid on gamma alumina (Figure 8c) also indicates that the interaction is occurring through the carbonyl with a shift from 1715 cm^{-1} in pure acetic acid to 1660 cm^{-1}. Acetic acid exhibited strong adsorption bands at 1470-1490 cm^{-1} and 1560-1600 cm^{-1} signaling the formation of acetate species on the surface of the alumina.
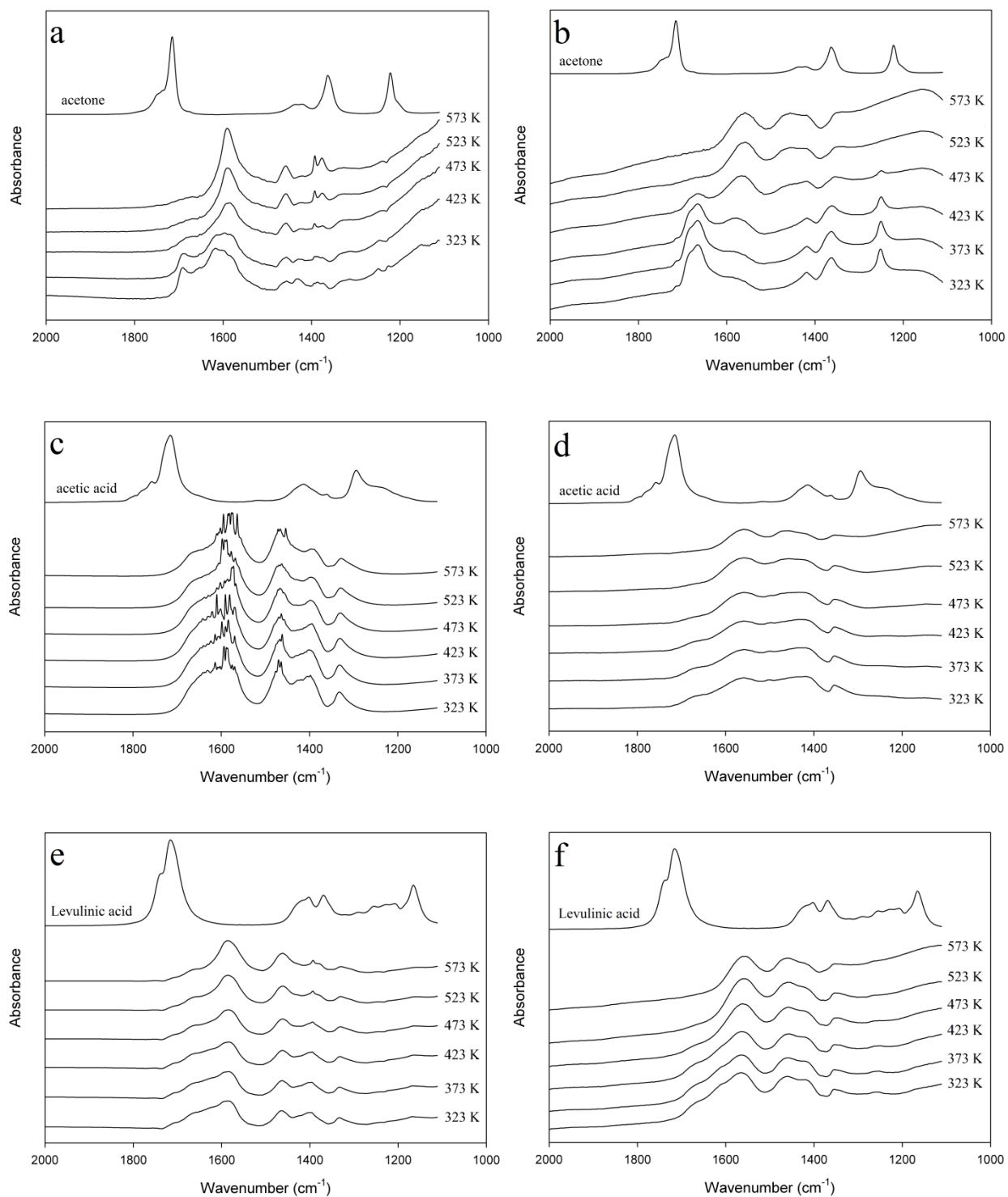
Figure 8 *Infrared spectra of interactions between a) acetone and γ-Al$_2$O$_3$, b) acetone and VO$_X$/γ-Al$_2$O$_3$, c) acetic acid and γ-Al$_2$O$_3$, d) acetic acid and VO$_X$/γ-Al$_2$O$_3$, e) levulinic acid γ-Al$_2$O$_3$, f) levulinic acid and VO$_X$/γ-Al$_2$O$_3$. For comparison, in each figure of stacked spectra the uppermost one belongs to the pure compound.*

On VO_x/γ-Al_2O_3 (Figure 8d), similar features were detected at 1460 and 1560 cm^{-1}. Those were anticipated spectra for acetic acid as it is expected to bind strongly on the catalyst and not be very reactive at these temperatures. When LA was dosed on γ-Al_2O_3 (Figure 8e), dominant bands were observed at 1462 and 1587 cm^{-1} signs of carboxylate formation. On VO_x/γ-Al_2O_3 (Figure 8f) a same pattern emerges and we see the characteristic carboxylate bands at 1461 and 1565cm^{-1} which persist at higher temperatures. For all spectra taken of the interaction between LA and VO_X/γ-Al_2O_3 a baseline was fit between 1200 and 1800 cm^{-1} and the peaks were deconvoluted in Matlab. They are stacked with ascending temperature from bottom to top in Figure 9. Deconvoluted spectra suggest that carboxylate species (1461 and 1565 cm^{-1}) form at very low temperatures and have a great affinity for the catalytic surface. Even at 573 K, while most peaks have either disappeared or have decreased in strength, carboxylate species still seem to bind very strongly. At reaction temperatures, carboxylates are the dominant surface species.

For all probe molecules, at temperatures up to 573 K, carboxylate species are not only present but dominate the surface interactions. For gamma alumina carboxylate formation persisted even at calcination temperatures (723 K) which is sufficient to lead to the assumption that at reaction temperatures, carboxylate species dominate the exposed alumina. Over VO_x/γ-Al_2O_3, and at higher temperatures than 573 K, the presence of redox sites enables the oxidation and combustion of persistent carboxylates. This persistence of carboxylate species could explain why we observe large amounts of CO_x at high temperatures during oxidation of LA.
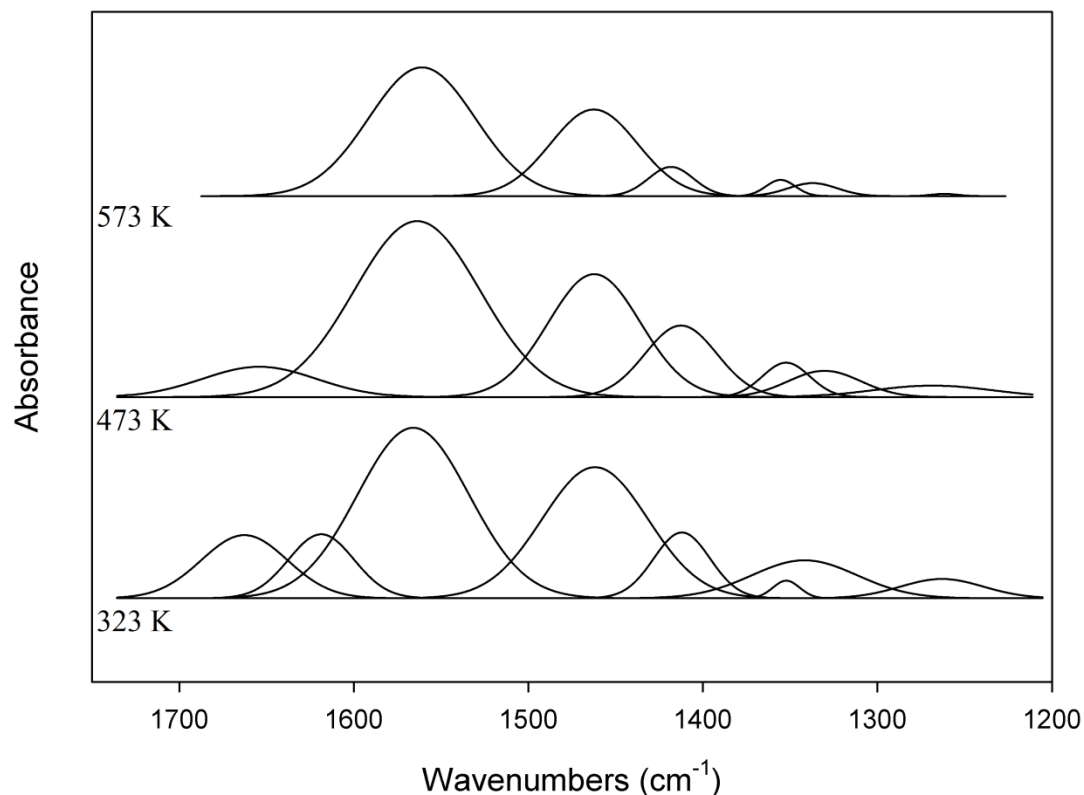
Figure 9 *Deconvoluted spectra of LA on γ-Al₂O₃ at different temperatures. The original spectrum was futher processed in Matlab where it was trimmed down to wavenumbers between 1200-1800cm⁻¹, a linear baseline was fitted and the signal was deconvoluted to multiple Gaussian peaks*

The exact nature of the coordination of LA might have significant impact on selectivity.

Assuming the pathway for oxidative cleavage of LA is enol mediated rather than lactone

mediated (Pathway 1 in Scheme 6), if LA coordinates exclusively through the ketone C=O then

oxidative cleavage is expected to proceed through a pathway similar to that of simple

methylketones and we should primarily expect products of internal cleavage. Alternatively, if LA

coordinates through the carboxylic C=O then, for oxidative cleavage to occur, the ketone must

form an enol and so the C=C must coordinate too. The further away the enolic C=C bond is from

the anchored carboxylate, the less sterically hindered the formation of the enol will be and thus,

the more favorable the internal enol will be at the expense of the terminal one. This could potentially explain why selectivity for products of terminal cleavage is much higher with LA than with simple methylketones. This might also explain the increased selectivity for internal cleavage in 4-acetylbutyric acid compared to LA. In conclusion, the IR studies did reinforce the idea that ketoacids such as LA coordinate strongly through the carboxyl group suggesting different mechanisms in the oxidative cleavage of ketoacids versus that of simple methylketones. It is highly likely that the internal C=C bond is less accessible for cleavage in the case of LA due to steric effects, rendering higher selectivities for terminal bond scission. It is, however, hard to assess whether the mechanism for LA cleavage is mediated through the angelicalactone foemation or through the direct scission of the methyl carbon in LA.

4.6 Contact Time Study on the Oxidative Cleavage of Angelicalactones and LA

In order to address the selectivity issue in a more conclusive manner, we designed an experiment where 2-pentanone, α-angelicalactone and LA were employed as feed molecules under a range of different contact times in order to assess product evolution from very short contact times. High liquid flowrates, especially for low vapor pressure compounds such as LA and α-angelicalactone, are a concern regarding complete vaporization. To reach short contact times while keeping liquid flowrates relatively low, a batch of 4.4 wt% VO_x/Al_2O_3 was prepared by diluting appropriate amounts of pure VO_x/Al_2O_3 with quartz in order to accurately load small masses of catalyst in our reactor. The real goal is to find a contact time where we can minimize the conversion of LA to angelicalactones. If MA production proceeds through angelicalactones then little to no rate should be recorded at those conditions, while if we change the feed from LA to α-angelicalactone we should expect to see appreciable rates of MA production. At higher contact times where LA conversion to angelicalactones increases and thus, angelicalactone

partial pressures increase, we expect the rates of MA to also increase. Reactor temperature was set at 420 K to minimize conversion, but also to operate at a temperature where oxidative dehydrogenation is unlikely.
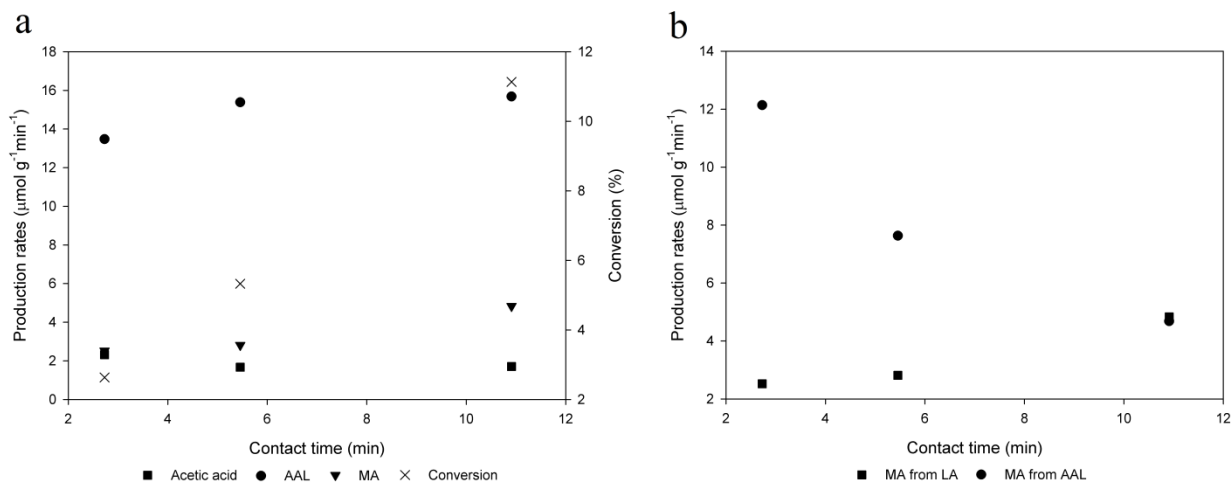
Figure 10 *Contact time study of the production of MA from LA and AAL. a) rates of product formation and total conversion from the oxidation of LA, b) Comparison of MA production rates from both LA and AAL at same contact times. LA and AAL partial pressures at 3.7 torr, O$_2$ partial pressure at 144 torr and temperature at 420 K.*

Figure 10a depicts production rates of acetic acid, AAL and MA at varying contact times. Once again we notice that MA rates increase monotonically with increasing contact time, a trait of non-primary reaction products. One more thing of importance that emerges from this figure is that the rate of production of acetic acid does not change with increasing contact times and one could argue that it is slightly higher at lower contact times giving it, in any case, a non-zero intercept, suggesting it is a primary product of oxidative cleavage as we have postulated earlier. Figure 10b is reinforcing the assumption that MA might be a primary product of AAL oxidative cleavage as its rate of formation exhibits a non-zero intercept and actually increases with decreasing contact time pointing to possible secondary reactions to overoxidation products. At a contact time of 2.3 min the rate of production of MA from AAL is 12.1 μmolg^{-1}min^{-1}, while from

LA it is almost a factor of 5 lower at 2.5 $\mu molg^{-1}min^{-1}$. As we increase the contact time to 10.9

min we see that the rates of production are almost identical at approximately 4.8 $\mu molg^{-1}min^{-1}$.

Furthermore, no appreciable rate of terminal cleavage was observed when 2-pentanone was

introduced into the reactor at a contact time 2.7 min. Even at a contact time of 10.9 minutes,

butyric acid production rate from 2-pentanone was 0.09 $\mu molg^{-1}min^{-1}$, 50 times lower than those

from either LA or AAL suggesting that terminal cleavage in 2-pentanone and terminal cleavage

in LA proceed with very different pathways. Acetic acid production rates across all contact times

from all three feeds were almost identical suggesting that internal cleavage proceeds through a

similar pathway for all three reactants.

At this point, the pathway leading to the formation of MA through the oxidative cleavage of the

methyl carbon in AAL seems very plausible. This does not mean that oxidative cleavage will not

occur on the methyl carbon of LA similar to 2-pentanone; the contribution to the total rate of

terminal cleavage will be very small. LA possesses a unique configuration as a γ-ketoacid,

meaning it can easily form lactones that are very stable and can undergo oxidative cleavage of

the methyl carbon more readily than LA or 2-pentanone. β-ketoacids have conjugated carbonyls

and tend to be very unstable, while longer chains such as δ-ketoacids will form bigger and more

unstable rings, unless they reconfigure to 5-membered ring lactones. LA is behaving as the

"Goldilocks" of ketoacids due to its unique oxidative cleavage behavior.

4.7 Oxidative Cleavage in Methyl Levulinate

In addition to LA and AAL, methyl levulinate (MLA), the methyl ester of levulinic acid was

shown to be prone towards terminal cleavage, achieving a 51% yield of MA (T= 588 K,

p_{MLA}=0.019, p_{O_2}= 0.205 bar, WHSV=0.272 min^{-1}). MLA is produced by sugar methanolysis and

is easier to work with due to its milder physical characteristics. While LA is solid at 25 °C, very viscous and polymerizes at high temperatures, MLA promises an easier downstream processing with a much lower melting point (-24 °C), higher vapor pressure and lower viscosity. Most biomass upgrading routes involve the production or side production of LA and levulinic esters. Both are targeted as platform molecules with the downstream processing aiming at the production of solvents, fuels, fine chemicals etc. We anticipate that higher yields are achievable, as we only tested the reaction under the above set of conditions over VO_x/Al_2O_3.

5 Vanadium Surface Speciation and Interaction with the Metal Oxide Support: Effects on the Intrinsic Properties of Catalysts.

5.1 Introduction

As outlined in the previous chapter, over reducible oxides, oxidative chemistries frequently proceed through a Mars-van-Krevelen mechanism, wherein atomic oxygen is transferred to adsorbed species by concurrent reduction of lattice heteroatoms. This forms reaction products, which desorb to expose an oxygen vacancy. Gas-phase molecular oxygen then facilitates re-oxidation of the lattice to complete the catalytic cycle [36, 46]. Because lattice oxygen plays such a critical role in Mars-van-Krevelen mechanisms, rates of heterogeneously catalyzed oxidations are often sensitive to changes in the nature of the oxygen-heteroatom bonds that comprise the active site [47-49]; however, there have been few prior investigations aimed at developing the structure-function relations that govern oxidative scission of ketones; accordingly, we take steps to do so here.

At vanadium oxide surfaces, oxygen atoms can be found in one of three bonding environments: vanadyl oxygens (V=O), vanadium-oxygen-vanadium bonds (V-O-V), and vanadium-oxygen-support bonds (V-O-M, where M is the heteroatom cation in the solid oxide support) [50, 51]. The oxygen distribution depends on the local structure adopted by vanadium oxides, of which one can identify three broad categories: isolated, tetrahedral vanadate monomers; oligomeric, surface vanadates that extend in one or two dimensions; and bulk, three-dimensional crystallites (e.g., V_2O_5) [52]. The vanadium oxide distribution is sensitive to the nature of the metal oxide support, the vanadium loading, the vanadium precursor, and the synthetic methodology [53-55]. As the character of the lattice oxygen population changes with the identity of the vanadium

phase, so may catalytic reactivity. Further, it is clear that changing the identity of the support cation, M, will perturb the electronic structure of the V-O-M bond, which can make its reduction more or less facile. If reduction or re-oxidation of the V-O-M vanadium is kinetically significant, this perturbation will directly impact oxidation kinetics [54]. In order to probe how intrinsic rates of ketone oxidation respond to changes in vanadate structure and support cation identity, we have prepared twenty catalysts by depositing vanadium at five different fractions of the theoretical monolayer coverage (0.0, 0.1, 0.5, 1.0 and 1.5) onto four oxide supports of varying cation reducibility (SiO_2, γ-Al_2O_3, TiO_2 and CeO_2). Physical and chemical properties of each catalyst were determined by FT-Raman spectroscopy, N_2 physisorption, and temperature-programmed surface oxidation (TPSO) of methanol. In order to build connections between active site structure and catalytic function, we have additionally quantified the activity of each catalyst during oxidation of 2-pentanone, which is a suitable probe reaction for investigating fundamental aspects of oxidative ketone scission.

5.2   Materials and Methods

5.2.1   Reagents

Cerium nitrate hexahydrate (Acros Organics, 99.5%), γ-alumina (Strem Chemicals, 95%), titanium dioxide (Acros Organics, Aeroxide® P25), amorphous silica (Sigma-Aldrich, Davisil Grade 633), ammonium metavanadate (Sigma-Aldrich, ≥99.5%) and oxalic acid (Acros Organics, 98%) were used in catalyst synthesis. Vanadium pentoxide (Acros Organics, 98+%) was used as supplied. 2-pentanone (Acros Organics, 99%) was used as a probe molecule. Formaldehyde (Sigma-Aldrich, 37wt.% in H_2O, 10-15% methanol as stabilizer), dimethyl ether (Aldrich Chemistry, ≥99%), acetaldehyde (Sigma-Aldrich, ≥99.5%), acetic acid (Acros

Organics, 99.8%), propionaldehyde (Acros Organics, 99+%), propionic acid (Acros Organics, 99%), n-butyric acid (Acros Organics, 99+%), CO (Airgas, 1%, 1% Ar, balance He) and CO_2 (Airgas, 1%, 1% Ar, balance He) were used for calibration of analytical instruments. Methanol (Fisher, Optima 99.9%) was employed for TPSO experiments. Water was purified in house by sequential reverse osmosis, UV oxidation, and double ion exchange to >18.2 MΩ cm resistivity (Spectrapure). He (Airgas, Ultra High Purity) and O_2 (Airgas, Ultra High Purity) were used as diluent and oxidant during reactor operation. Air (Airgas, Ultra Zero Grade) was used for ex-situ calcination of all catalyst samples.

5.2.2   Catalyst Synthesis

Cerium oxide was synthesized by calcination of cerium nitrate hexahydrate in static air at 823K (5K min^{-1}, 4 h) [56]. $CeVO_4$ samples were synthesized using an established co-precipitation method [57]. Specifically, an alkaline (NaOH) solution of ammonium metavanadate was reduced by sodium borohydride and subsequently reacted with cerium nitrate to precipitate $CeVO_4$. Vanadium oxides were supported on SiO_2, γ-Al_2O_3, TiO_2, and CeO_2. Vanadium mass loadings were varied on each support to achieve fractions $(0.1 - 1.5)$ of the theoretical monolayer coverage of VO_x units for that support.

Supported vanadium oxides were prepared by incipient wetness impregnation of ammonium metavanadate dissolved in aqueous oxalic acid. The molar ratio of ammonium metavanadate to oxalic acid was 2:1, and the molar concentration of ammonium metavanadate was varied as necessary to achieve desired vanadium loadings [54, 58, 59]. Resultant solids were dried at 338K, crushed to break aggregates, calcined under flowing air at 723K (60 sccm, 3 K min^{-1}, 4 h), crushed into fine particles, and graded through standard mesh sieves. Treating samples at 723K

in air is sufficient to decompose precursor salts, resulting in deposition of vanadium (+5) oxides

on the support surface [60, 61]. All characterization and reaction experiments were performed

using catalyst particles in the 45-90 μm range. In this manuscript, we refer to quantities defined

in Equations 1 – 3, which specify vanadium loadings in several dimensions.

$$V_A = \frac{N_V \cdot N_A}{m_s SA_s} \tag{1}$$

$$V_M = \frac{N_V}{N_V \cdot MW_V + m_s} \tag{2}$$

$$V_W = V_M \cdot MW_V \cdot 100 \tag{3}$$

In these equations, V_A is the areal density of atomic vanadium (V nm^{-2}); V_M is the molar loading

of vanadium per unit mass of catalyst (μmol V g^{-1}); V_W is the mass percentage of vanadium in a

given catalyst; N_V is the total moles of vanadium in a given catalyst preparation; N_A is

Avogadro's number; m_S is the mass of support used in a given catalyst synthesis; SA_S is the

support surface area per unit mass determined by N_2 physisorption; and MW_V is the atomic mass

of vanadium.

5.2.3 Surface Area and Pore Measurements

Surface areas and average pore sizes for each catalyst and support were determined by N_2

physisorption at 77K (Micromeritics, ASAP 2020). Prior to N_2 dosing, samples were outgassed

under vacuum for 4 hours at 523K. Total surface areas were determined by BET analysis.

Average pore diameters were determined from BJH analysis of the desorption branch of N_2

uptake isotherms [62, 63].

5.2.4 Raman Spectroscopy

Raman spectra were acquried using a Bruker FRA 106 FT-Raman spectrometer equipped with an Nd:YAG laser emitting at 1064 nm. Prior to spectral acquisition, samples were dehydrated ex situ in a home-built cell. 50 – 60 mg of powdered catalyst were loaded into a quarter inch borosilicate tube and held in place with two quartz wool end plugs. Samples were then calcined under a flow of zero-grade air (723K, 3 K min^{-1}, 4h, 60 sccm) that was further dried by passing through a moisture trap (Agilent, MT200-4). After cooling to room temperature under continuous purge, the cell was pressurized (2.4 bar, absolute pressure), sealed using block valves, and transferred into the FT-Raman sample chamber. Spectra were obtained at a resolution of 2 cm^{-1} at room temperature using a laser power of 200 mW with an accumulation of 200 scans. Before each measurement, the instrument focus was tuned using an external V_2O_5 standard. Full width at half maxima (FWHM) were computed for individual Raman bands by fitting each peak to a normal distribution function, which generates regressed values for the peak location and standard deviation (σ) for the distribution. For Gaussian peaks, the FWHM is calculated as a function of standard deviation (Equation 4):

$$FWHM = 2\sqrt{2 \cdot \ln(2)} \cdot \sigma \qquad (4)$$

5.2.5   Temperature Programmed Surface Oxidations

The oxidative capacity of each catalyst was quantified using temperature programmed surface oxidation (TPSO) of chemisorbed methanol [58, 59, 64, 65]. 100 – 400 mg of powdered catalyst were supported between two quartz wool plugs inside of a 1/2″ quartz tube, which was then positioned inside of a high-temperature ceramic furnace (Omega, CRFC). Samples were calcined under zero-grade air (50 sccm, 723 K, 4 h) and subsequently cooled to 373 K. The process gas was then switched from air to a Helium/Methanol blend (100 sccm, 22 Torr methanol, balance

He), which was was prepared by vaporizing a continuous flow of liquid methanol into a Helium sweep. The methanol feed was controlled using a syringe pump (Cole Parmer series 100) and introduced to the He stream through a capillary tube. The catalyst sample was contacted with methanol until reaching its saturation uptake (typically within 30 minutes), which was determined by monitoring the effluent methanol concentration using an online, mass-selective residual gas analyzer (RGA, Stanford Instruments RGA 100). After surface saturation, the sweep gas was switched to 100 sccm of a Helium blend containing 1% argon (internal standard), and the sample was purged until no further evolution of methanol was observed ($\approx$ 60 min). The cell temperature was then ramped to 773 K at a rate of 10 K min^{-1}. During the temperature ramp, MS signals corresponding to formaldehyde ($m/z = 29$), carbon monoxide ($m/z = 28$), carbon dioxide ($m/z = 44$), dimethyl ether ($m/z = 45$), methanol ($m/z = 31$) and argon ($m/z = 40$) were monitored continuously. RGA response factors were determined, relative to the argon internal standard, for each species. All MS signals were corrected for fragmentation interferences. Temperature in the furnace was measured using a type K thermocouple (Omega) and controlled using a PID temperature controller (Love Controls, Series 16A).

Total oxidation site densities were determined from quantities of evolved formaldehyde (HCHO), carbon monoxide (CO), and carbon dioxide (CO_2), which are all products of methanol oxidation. Unfortunately, as methanol TPSO was performed under inert atmospheres and high temperatures, there is ambiguity in assigning the precise stoichiometries leading to formation of HCHO, CO, and CO_2. For example, HCHO can form by either oxidative or non-oxidative dehydrogenation of methanol. In turn, CO might form either through oxidative or non-oxidative dehydrogenation of formaldehyde. This uncertainty further propagates into the stoichiometry of CO_2 evolution. In our analysis, we have assumed that each carbon atom observed in the reactor

effluent is generated from one molecule of chemisorbed methanol, and that hydrogen atoms not recovered in formaldehyde are oxidized fully to form water. The former assumption is straightforward, while the latter is based on the fact that we observed limited evolution of molecular H_2 (m/z = 2.0) relative to observed quantities of HCHO and CO during control experiments. Since methanol TPSO was conducted under an inert atmosphere (He), stoichiometric quantities of oxygen must be provided by reduction of the catalyst. Accordingly, as summarized in Equations 5 – 7, we take evolution of formaldehyde (HCHO) to indicate titration of a single accessible oxygen atom, carbon monoxide (CO) to indicate titration of two accessible oxygen atoms, and carbon dioxide (CO_2) to indicate titration of three accessible oxygen atoms. Weighing evolved quantities of HCHO, CO, and CO_2 in this manner, we estimate the total number of redox accessible oxygen atoms per gram of catalyst.

$$CH_3OH + O \rightarrow HCHO + H_2O \tag{5}$$

$$CH_3OH + 2O \rightarrow CO + 2H_2O \tag{6}$$

$$CH_3OH + 3O \rightarrow CO_2 + 2H_2O \tag{7}$$

5.2.6 Catalytic Activity Testing

Although our motivating interest is the oxidation of levulinic acid, we have examined, as a model system, the catalytic activity of each material in the oxidative scission of 2-pentanone. There are several reasons for doing so. First, levulinic acid and its dominant oxidation product (maleic anhydride) have low vapor pressures, which complicates partial pressure control and online chromatographic analysis, both of which are essential to rigorous kinetic analysis of gas-phase reactions [66]. In contrast, vaporization of 2-pentanone is facile, and it produces a suite of $C_1 – C_4$ monofunctional hydrocarbons that have relatively high vapor pressures and are easily

resolved and quantified by online GC analysis. Second, levulinic acid is thermally unstable. Under oxidative reaction conditions, it is consumed in parallel by a number of facile, non-oxidative pathways, which complicates quantitative determination of oxidation reaction rates [4]. 2-pentanone, on the other hand, is consumed primarily by oxidative scission pathways. Finally, whether one considers levulinic acid oxidation or 2-pentanone oxidation, the central chemistry involves oxidative cleavage of the C-C bond between the ketone carbonyl and one of its alpha carbons. Accordingly, 2-pentanone oxidation captures the fundamental essence of ketone oxidation, and any insights generated regarding oxidative scission of ketones are broadly applicable to levulinic acid oxidation.

2-pentanone oxidation was carried out in the gas phase using an up flow, packed bed reactor. To mitigate exothermicity, sieved catalyst powders (45 – 90 µm) were diluted 1:4 in sieved quartz powder (45 – 90 µm). The diluted catalyst bed was positioned at the midpoint of a 7 ½" x ¼" stainless steel tube and held in place with two quartz wool plugs. The upstream section of the reactor tube was filled with quartz chips. The packed bed was then placed inside of a high temperature furnace and connected to the gas manifold using compression fittings. Prior to subjecting catalysts to ketone oxidation conditions, each bed was calcined in situ at 723 K for 4 hours under an O_2/He (1:5) gas mixture. Reactor gas feeds were comprised of 2-pentanone vaporized into an O_2/He blend. The setup employed is identical to the one shown in Scheme 11. The O_2/He blend was prepared by combining O_2 and He in desired ratios using mass flow controllers (Brooks 5850S). It was subsequently fed, alongside liquid 2-pentanone, into a ½" stainless steel vaporizer that was packed with quartz granules and held at 393K. 2-pentanone was introduced into the vaporizer through a capillary tube, and its flow rate was controlled using a syringe pump (Cole Parmer series 100). This configuration provided complete vaporization of 2-

pentanone over the range of partial pressures and space velocities reported here. The vaporizer effluent was fed into a 6-port valve, which was used to direct the process stream either into the packed bed reactor or to a bypass. During startup, the process gas was fed into the bypass and monitored by online GC until reaching steady state, while the reactor tube was purged with an O_2/He mixture. Subsequently, the 6-position valve was switched to divert the process stream into the packed bed reactor. The time of this switch is defined herein as zero time-on-stream. Feed mole fractions were controlled at 0.015 2-pentanone, 0.164 O_2, and 0.821 He. All reactions were carried out at a total system pressure of 915 Torr, and the pressure gradient across the catalyst bed was always less than 100 Torr or roughly 11% of the inlet pressure. Space velocities were adjusted to maintain 2-pentanone conversions below 4% for all catalysts under all reaction conditions. Reported reaction temperatures reflect the internal reactor temperature, which was measured immediately downstream of the catalyst bed using an inline, Type K thermocouple. Comparison to control experiments revealed that, for the range of feed rates and conversions reported here, the temperature gradient across the catalyst bed was always less than 1°C. The above observations suggest the differential reactor approximation is reasonable; accordingly, we take kinetic data reported here to reflect reaction rates obtained under isothermal conditions at 466K and under an atmosphere of 13.7 Torr 2-pentanone, 150 Torr O_2, and 751 Torr He.
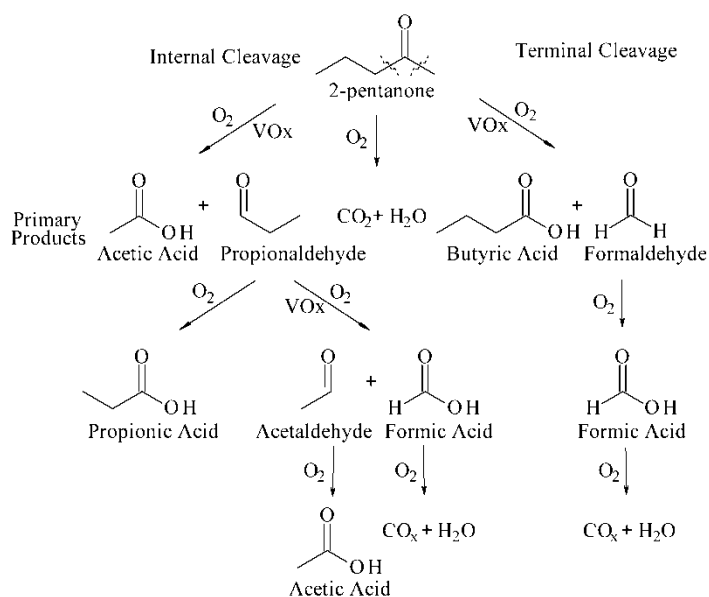
Scheme 16 *Primary and secondary reactions observed during 2-pentanone oxidation*

For product analysis, the reactor effluent was passed to an online GC through a stainless steel transfer line that was maintained at 423K, which was sufficient to prevent condensation of all species at their representative partial pressures. Species concentrations were determined using an HP 5890 GC equipped with two inlets, two columns, and two detectors. A Restek ShinCarbon ST Micropacked Column connected to a TCD detector was used for resolution and quantification of O_2, CO, and CO_2. An HP-INNOWAX column coupled to an FID detector was used for resolution and quantification of all other species, which included carboxylic acids, aldehydes, and ketones. Temperatures in the reactor and all auxiliary heated zones were monitored with K-type thermocouples (Omega) and controlled using PID temperature controllers (Love Controls Series 16A). Carbon balances closed to within 5%.

As illustrated in Scheme 16, there are three primary pathways of 2-pentanone oxidation; further, the products formed therein are generally susceptible to secondary oxidation. Since we have controlled only partial pressures for oxygen and 2-pentanone, the only meaningful kinetic

analysis is one that considers rates of primary reactions consuming 2-pentanone; however, the prevalence of secondary and tertiary reactions makes their quantification nontrivial. To aid in our analysis, we generated Scheme 16 through a set of control experiments designed to distinguish stable products from those that undergo further conversion. This topic will be detailed in a forthcoming manuscript; however, we briefly summarize key aspects here in order to justify the convention we have used in defining primary rates of 2-pentanone oxidation.

The three primary pathways that consume 2-pentanone are (1) direct combustion to form CO_2 and H_2O, neither of which undergoes further conversion; (2) oxidative scission of the C_2-C_3 bond (internal cleavage) to form acetic acid and propionaldehyde; and (3) the oxidative scission of the C_1-C_2 bond (terminal cleavage) to form butyric acid and formaldehyde. Under the conditions reported here, we observe less than $\approx 10\%$ selectivity to direct combustion pathways. With respect to internal cleavage products acetic acid is stable, while propionaldehyde is consumed by both direct oxidation to form stable propionic acid, and oxidative cleavage to produce acetaldehyde and formic acid. Formic acid decomposes to water and carbon oxides [67, 68]. Acetaldehyde does not undergo further C-C scission under our reaction conditions; however, it is oxidized to form acetic acid. In contrast, terminal cleavage of 2-pentanone forms butyric acid and formaldehyde. As with acetic and propionic acid, butyric acid is stable under our reaction conditions. Formaldehyde is oxidized to formic acid, which forms water and carbon oxides [68, 69]. Due to their facile oxidation/decomposition, neither formaldehyde nor formic acid were observed in our system; their presence in this landscape is inferred through analysis of plausible ketone oxidation mechanisms [32, 70]. Finally, control experiments revealed trace background activity resulting in formation of acetaldehyde, propionaldehyde, and acetic acid. As all of these species are observed during 2-pentanone oxidation over supported vanadates, background molar

flow rates for each compound were determined for each reaction condition and subtracted from extensive production rates of acetaldehyde, propionaldehyde and acetic acid prior to evaluation of reaction rates (Equations 8 and 9).

From Scheme 16, the total rate of internal cleavage for 2-pentanone (R_I) can be determined based on background-corrected molar flowrates of acetaldehyde (F_A), propionaldehdye (F_P), acetic acid (F_{AA}), and propionic acid (F_{PA}) as shown in Equation 8.

$$R_I = \frac{F_A + F_P + F_{AA} + F_{PA}}{2} \tag{8}$$

Butyric acid is stable even under our most severe conditions. Accordingly, from Scheme 16, one can establish the rate of terminal scission (R_T) based solely on observed quantities of butyric acid (F_{BA}) as shown in Equation 9:

$$R_T = F_{BA} \tag{9}$$

Under all reported conditions and excluding direct combustion of 2-pentanone, selectivity toward the internal cleavage pathway is >95%; thus, to streamline discussion, we present only the rate of internal oxidative cleavage (R_I). Based on our analysis, kinetic trends observed for terminal scission are identical to those observed for internal scission; accordingly, little is gained from a parallel consideration of terminal scission rates in this analysis.

In comparing catalytic activities, we employ site-time yields (STY), which are defined as the measured rate of internal oxidative cleavage of 2-pentanone (R_I) per unit oxidation site (Equation 10). As such, they approximate a turnover frequency. The total number of oxidation sites in a

catalyst bed is computed as the product of catalyst mass loading (m_{cat}) and the oxidation site

density determined by methanol TPSO (ρ_S).

$$STY = \frac{R_I}{m_{cat} \cdot \rho_S} \qquad (10)$$

Catalysts in this system always undergo a period of deactivation, and they generally reach steady

state within 50 hours on stream. As different catalysts on different supports may undergo

different extents of deactivation, it is difficult to directly compare steady state activities in two

different systems. Accordingly, we report only initial rates of reaction at zero-time on stream,

which were estimated by fitting experimentally measured decay profiles to a first order

deactivation model. Finally, we are confident that data reported here reflect intrinsic kinetics and

are not obscured by mass and heat transfer artifacts as is presented in the following section.

5.2.7 Heat and Mass Transport Limitation Criteria

This study considers rates measured over supported vanadium oxides having varied vanadium

loadings (active sites) for each support. Site time yields (STY) were estimated based on

measured rates of oxidative cleavage and the number of active sites as determined by TPSO of

adsorbed methanol. For the majority of our catalyst series, we observe variation in STY with

vanadium loading. This may indicate reaction rates that are controlled by mass or heat

transfer[71]; however, it is also possible that oxidative cleavage of ketones is a structure

sensitive reaction or that other artifacts obscure a true site-time yield. The possibility of a

structure sensitive reaction makes it difficult to apply a Madon-Boudart type test in this system,

as changing the vanadium loading will generally also change the structure of supported

vanadates. In order to exclude the possibility that transport limitations obscure true reaction

rates in this system, we tabulate theoretical criteria for maintaining kinetic control. Further, we consider the effect of particle size on measured reaction rates in our most demanding system.

Threshold criteria were evaluated at the maximum rate of oxidative cleavage observed for each support under reaction conditions (T = 466K, P = 915 Torr, $P_{2\text{-}P}$ = 14 Torr). Data used in estimating mass and heat transfer coefficients are summarized in Table 5. In certain cases, there is flexibility in assigning a parameter value. For example, the reaction enthalpy listed in Table 5 represents that for complete combustion of 2-pentanone to CO_2 and H_2O. Although we observe very little actual yield of CO_2 under our reaction conditions, this represents the most constrained situation for heat transfer—that of a strongly exothermic combustion. Throughout our analysis, we have employed this approach of using relatively conservative values that we believe represent the most difficult scenarios for maintaining kinetic control. We assume that if criteria are satisfied under these conditions, they are also satisfied at the remainder of experimental conditions, where reaction rates are slower than those compiled here, and actual exothermicity is far less than that given by total pentanone combustion.

Table 5 *Parameters used in evaluating criteria for assessing the extent of transport control during reaction*

Physical Quantity	Symbol	Value	Units
Catalyst particle radius	r_p	4.5×10^{-5}	m
2-pentanone concentration	C_b	0.48	mol/m^3
Tubing radius	r_t	2.3×10^{-3}	m
Total gas flow rate	Q	1.3×10^{-6}	m^3/s
Density of gas mixture	ρ	0.27	kg/m^3
Viscosity of gas mixture	μ	2.8×10^{-5}	Pa·s
Porocity of the catalysts	Φ_p	0.40	
Diffusivity of gas mixture	D_m	1.3×10^{-4}	m^2/s
Reynold number	Re	6.9×10^{-2}	
Mass transfer coefficient	k_c	1.5	m/s
2-pentanone diameter	D_{2-p}	7.0×10^{-10}	m
Average Velocity	$\tilde{v}$	340	m/s
Mean free path	λ	1.6×10^{-6}	m
Specific Heat for gas mixture (466 K)	Cp	4.5	kJ/kg K
Reaction enthalpy	ΔH	-2900	kJ/mol
Activation energy for CO2 reaction	Ea	91	kJ/mol
Thermal conductivity of gas mixture	k_g	0.16	Wm^{-1}K^{-1}
Prandtl number	Pr	0.78	
Heat transfer coffeicients	h	770	Wm^{-2}K^{-1}

Since 2-pentanone partial pressure was maintained at a dilute 14 Torr for all reactions, bulk properties of the flowing gas were evaluated with assumption that the process gas is binary mixture of helium (763 Torr) and oxygen (153 Torr). The total gas flowrate was 60 ml min^{-1} at STP, which corresponds to 1.3×10^{-6} m^3 s^{-1} at our reaction temperature and pressure. Diffusivity of helium and oxygen gas mixtures was computed under reaction conditions based on the work of Wasik and McCulloh.[72] Mass and heat transfer coefficients were obtained using methods in *Transport Processes and Unit Operations* by Geankoplis [73] and in *Unit Operations of Chemical Engineering* by McCabe, Smith, and Harriott.[74] Mean free path, average velocity and Knudsen diffusion were computed using correlations in *Kinetics of Catalytic Reactions* by Vannice.[75] We have estimated the diameter of 2-pentanone based on its density, molecular weight, and assumption of spherical molecular shape. Thermal conductivity of the gas mixture

was calculated using Wilke's rule. [76] The apparent activation energy for combustion was estimated from yields of combustion products observed in our system over a range of reaction temperatures. In addition to the generic system parameters summarized in Table 5, Table 6 lists the maximum observed rates for each support alongside the different physical properties. Since our computed mean free path is larger than the pore diameters in our catalyst supports, we assume that the effective diffusivity in a given system is equal to the Knudsen diffusivity. Although there is considerable uncertainty in estimating diffusivity, we note that these values are in the range of $1.0 \times 10^{-6} \ m^2 \ s^{-1}$, which is relatively conservative for gas diffusion.

Table 6 *Parameters used in evaluating criteria for each support.*

	Support			
	SiO$_2$	γ-Al$_2$O$_3$	TiO$_2$	CeO$_2$
Pore Size (Å)	68	75	320	160
Density (g m^{-3})	1.6×10^6	2.4×10^6	2.5×10^6	4.3×10^6
Knudsen diffusity (m^2/s)	7.7×10^{-3}	8.4×10^{-3}	3.8×10^{-2}	1.8×10^{-2}
Thermal conductivity (W m^{-1} K^{-1})	1.4	23	6	5
r''' (μmol g^{-1} min^{-1})	42	29	27	31
r''' (mol m^{-3} s^{-1})	1.1	1.2	1.1	2.2

Mass and heat transfer threshold criteria were calculated from equations 11 through 14. Results of the calculations with the set of parameters and reaction properties listed in Table 5 and Table *6* are shown in Table 7. Equation 11 was taken from *"Kinetics of Catalytic Reactions"* by Vannice[77], and equation 12 to 14 were taken from *"The Microkinetics of Heterogeneous Catalysis"* by Dumesic[78].

Weisz-Prater Criteria for excluding intraparticle diffusion limitations for a second order reaction:

$$\frac{r'''r_p^2}{C_b D_{eff}} < 0.3 \tag{11}$$

Criteria for excluding interphase mass transfer limitations

$$\frac{r'''r_P}{C_b k_c} < 0.15 \tag{12}$$

Criteria for excluding intraparticle Heat Transfer Limitations

$$\frac{|\Delta H_{rxn}| r''' r_P^2}{\lambda T_s} \cdot \frac{E_A}{RT_s} < 0.75 \tag{13}$$

Criteria for excluding interphase heat transfer limitations:

$$\frac{|\Delta H_{rxn}| \cdot r''' \cdot r_P}{h T_b} \cdot \frac{E_A}{RT_b} < 0.15 \tag{14}$$

Table 7 *Summary of threshold criteria for 2-pentanone internal oxidative cleavage reactions over each supports at the highest initial production rates.*

Support	Mass Transfer		Heat Transfer	
	Intraparticle	Interphase	Intraparticle	Interphase
SiO2	0.24	6.9×10^{-5}	2.4×10^{-4}	2.1×10^{-2}
Al2O3	9.8×10^{-2}	7.2×10^{-5}	2.5×10^{-4}	2.3×10^{-2}
TiO2	2.0×10^{-2}	7.0×10^{-5}	2.4×10^{-4}	2.2×10^{-2}
CeO2	2.8×10^{-2}	1.4×10^{-4}	4.8×10^{-4}	4.2×10^{-2}

According to tabulated criteria, even under the most constraining conditions (i.e., highest measured initial rates of reaction), threshold criteria are met in this system. However, the Weisz-Prater criterion for SiO_2 supported catalyst is approaching the threshold value. This is attributed to the fact that VO_x/SiO_2 catalysts at 1.0 and 1.5 monolayer loadings had the highest measured oxidation site densities of any catalyst tested in this study and thus the highest measured rates of oxidation per unit volume of catalyst; thus, the VO_x/SiO_2 system is the most demanding for satisfying kinetic control. Because threshold criteria cannot definitively exclude the possibility of intraparticle diffusion limitations, it was necessary to probe them experimentally.
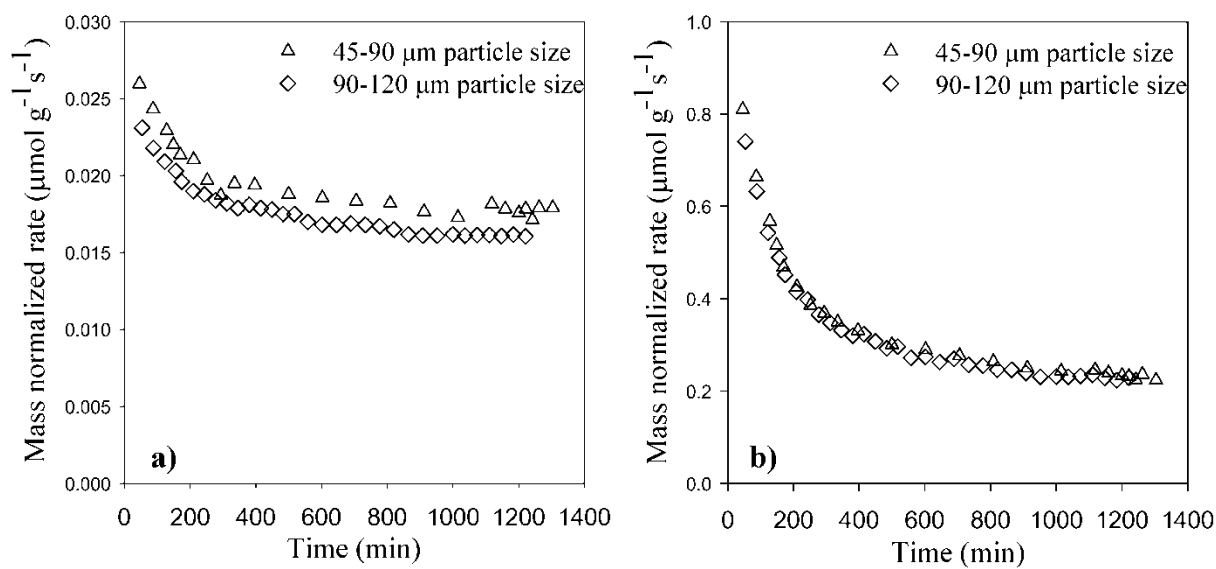
Figure 11 *Deactivation profiles of 2-pentanone oxidative cleavage reaction over 1.0 monolayer VOx/SiO2 catalyst with two different particle size: a) terminal cleavage, b) internal cleavage.*

To do so, we measured the rate of 2-pentanone oxidative cleavage on two VO_x/SiO_2 catalysts of different particle sizes prepared at 1.0 monolayer loading. Specifically, we measured the rate of oxidative cleavage on the 1.0 monolayer VO_x/SiO_2 sample in a sieve cut of particles ranging in diameter from 45-90 μm (T = 466K, P_{2-P} = 14 Torr). A second 1.0 monolayer VO_x/SiO_2 sample was pelletized, crushed, and sieved to obtain a larger particle size distribution (90-120 μm), which was then employed for oxidative cleavage of 2-pentanone under identical conditions. Figures Figure *11*a and Figure *11*b illustrate the deactivation profiles of the same catalyst with two different size ranges, and it is clear that oxidation rates are independent of particle size in this range. Initial rates for terminal and internal bond scission were estimated by fitting a first order decay model to the temporal profiles shown in Figures Figure *11*a and Figure *11*b. Since 2-pentanone oxidative cleavage is exothermic, the high conversion at zero time on stream will generate heat, resulting in a rise in temperature downstream of the catalyst bed (about 3-4 K at

our condition), suggesting non-isothermal operation during initial startup. The bed temperature stabilizes after roughly 150 minutes, whereafter a maximal gradient of 1K across the bed is indicated; consequently, only data measured after 150 minutes were used in estimating the initial reaction rate. Over the $90 - 120$ μm sieve cut, the internal cleavage rate (R_I) was 0.61 ± 0.04 μmol s^{-1}g^{-1} and the terminal cleavage rate (R_T) was 0.022 ± 0.002 μmol s^{-1}g^{-1}. Comparing with the smaller sized catalyst ($D_p = 45\text{-}90$ μm), the internal cleavage rate was 0.59 ± 0.04 μmol s^{-1}g^{-1} and the terminal cleavage rate was 0.025 ± 0.003. All estimations are indistinguishable within statistical precision, and we conclude that the rates measured on the two samples have no dependence on particle size and are therefore free of intraparticle transport limitations. As this material presented the highest rate per volume in the set of catalysts considered here, we assume this conclusion extends to all other materials considered in this study.

5.3   Results and Discussion

Vanadium loadings are summarized in Table 8. The molar loading of vanadium at monolayer coverage was calculated as the product of the support surface area and the areal density of dispersed VO_x sites at monolayer coverage; thus, a low areal vanadate density does not necessarily mean a low vanadium loading. For example, because of its relatively low hydroxyl surface density, silica will accommodate a lower monolayer coverage of vanadium oxides (≈ 2.3 VO_x nm^{-2}) [61] than supports with higher hydroxyl densities, such as $\gamma\text{-}Al_2O_3$, TiO_2, and CeO_2 ($\approx 8 - 9$ VO_X nm^{-2}) [52, 55, 58]; however, SiO_2 has a relatively high surface area per unit mass, which facilitates substantial mass percentages of vanadium despite a low hydroxyl density. As the solid oxides employed here are a somewhat heterogeneous class of materials, "monolayer coverages" reported in the literature are not taken as rigorously quantitative; rather, they are used to provide benchmarks that guide the vanadium loadings required to achieve vanadate densities

above and below monolayer coverage. Vanadium speciation is sensitive to coverage; thus, this approach should yield catalysts where vanadium oxides exist in a range of local environments, which aids in connecting structure and function [53, 79]. For convenience, catalysts are nominally described using their theoretical fraction of monolayer coverage (0.0, 0.1, 0.5, 1.0, and 1.5).

Table 8 Vanadium content of supports, bulk vanadates, and supported vanadium oxides [52, 58, 61, 80]. The BET surface areas for the supports used in these syntheses were: SiO_2 (490 m^2 g^{-1}), Al_2O_3 (231 m^2 g^{-1}), TiO_2 (49 m^2 g^{-1}), and CeO_2 (75 m^2 g^{-1}).

Support	Fraction of monolayer	V Coverage (V nm^{-2})	V loading (wt.%)	V loading ($\mu mol g^{-1}$)
SiO_2	0.1	0.23	0.939	185
	0.5	1.16	4.42	862
	1	2.3	8.15	1600
	1.5	3.45	11.4	2236
γ-Al2O3	0.1	0.799	1.52	298
	0.5	3.99	6.86	1347
	1	7.99	12.2	2399
	1.5	12	16.5	3245
TiO_2	0.1	0.812	0.335	65
	0.5	4	1.61	316
	1	8	3.13	614
	1.5	12	4.56	897
CeO_2	0.1	0.857	0.536	104
	0.5	4.25	2.56	503
	1	8.49	4.89	962
	1.5	12.8	7.05	1382

To probe vanadium speciation, we employed Raman spectroscopy, which is useful in distinguishing dispersed (1D and 2D) vanadium oxide phases from those present as bulk crystallites [36, 53, 81-84]. Figures Figure *12* through Figure *15* present full scale Raman spectra for all catalysts and supports indicated in Table 8. Since the most informative region for gauging the relative populations of dispersed and bulk phases is between 600 and 1200 cm^{-1} [85]. Figures

Figure *17* through Figure *20* are cropped in order to focus on that spectral window; moreover, specific features within this region reveal additional details regarding the extent of oligomer formation in networks of surface vanadium oxides [86-88]. Spectra in Figures Figure *12* through Figure *15* and Figure *17* through Figure *20* were normalized to the support features indicated in the figure caption; accordingly, spectra within a given support series may be taken as a semi-quantitative assessment of vanadium coverage and speciation. In addition, Figure 16 shows full scale spectra of the bulk structures of V_2O_5 and $CeVO_4$ indicated in subsequent analysis.
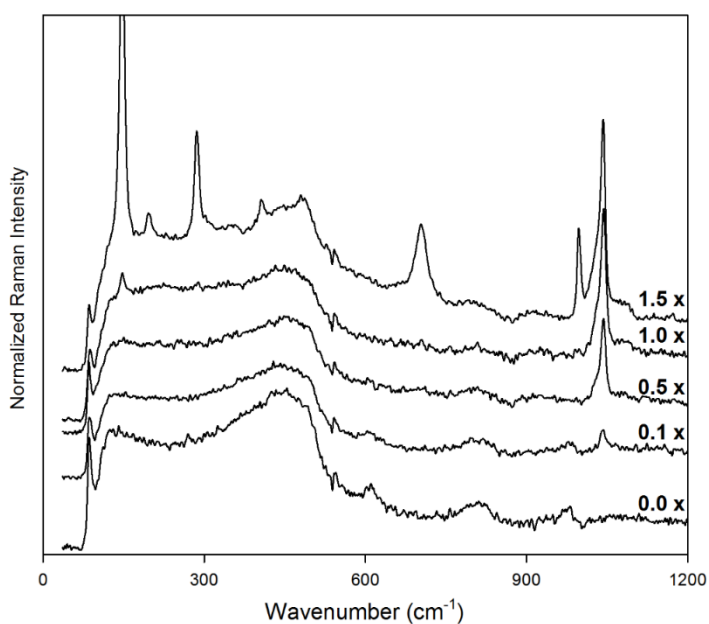
Figure 12 *Full Raman spectra of supported vanadates on SiO_2, VO_x/SiO_2. The spectra were normalized to the peak intensity of the broad SiO_2 band at 460 cm^{-1}.*
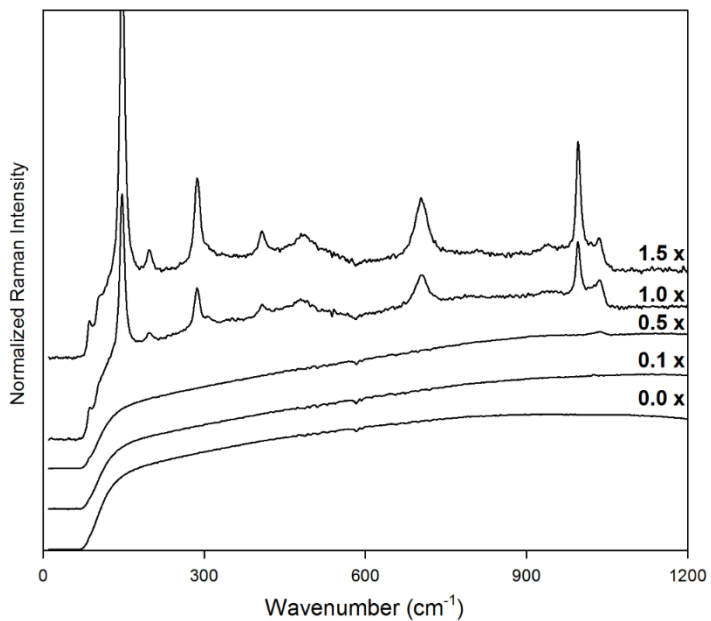
Figure 13 *Full Raman spectra of supported vanadates on γ-Al$_2$O$_3$, VOx/ γ-Al$_2$O$_3$. Due to the absence of support bands, VOx/Al$_2$O$_3$ spectra were normalized to spectral intensity at 1100 cm^{-1}.*
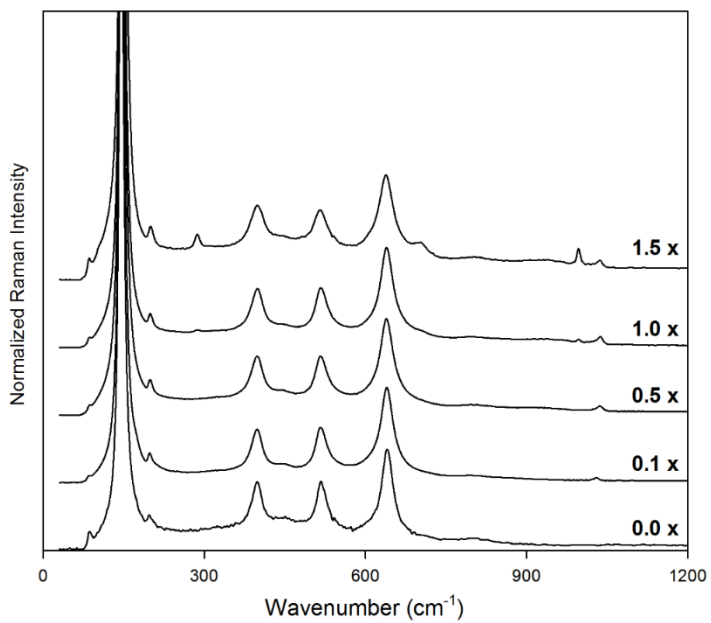
Figure 14 *Full Raman spectra of supported vanadates on TiO$_2$, VO$_x$/TiO$_2$. The spectra were normalized to the TiO$_2$ band at 640 cm^{-1}.*
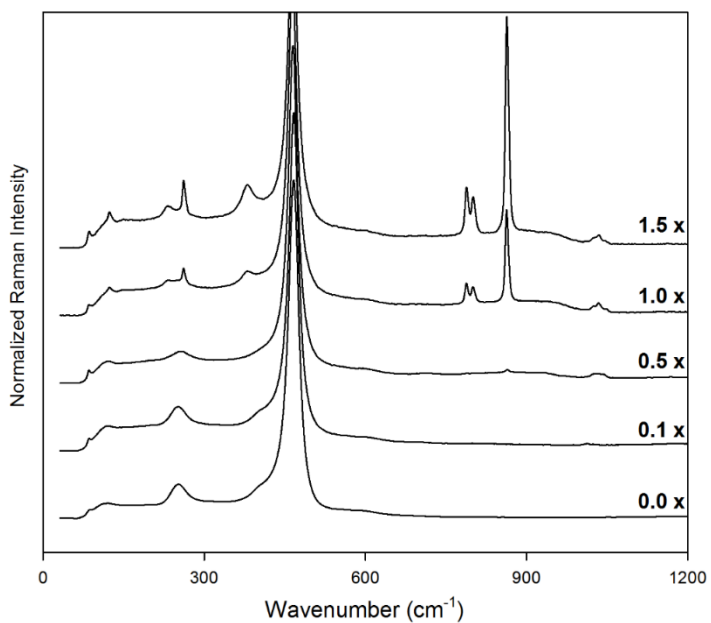
Figure 15 *Full Raman spectra of supported vanadates on CeO$_2$, VO$_x$/CeO$_2$. The spectra were normalized to the ceria band at 467 cm^{-1}*
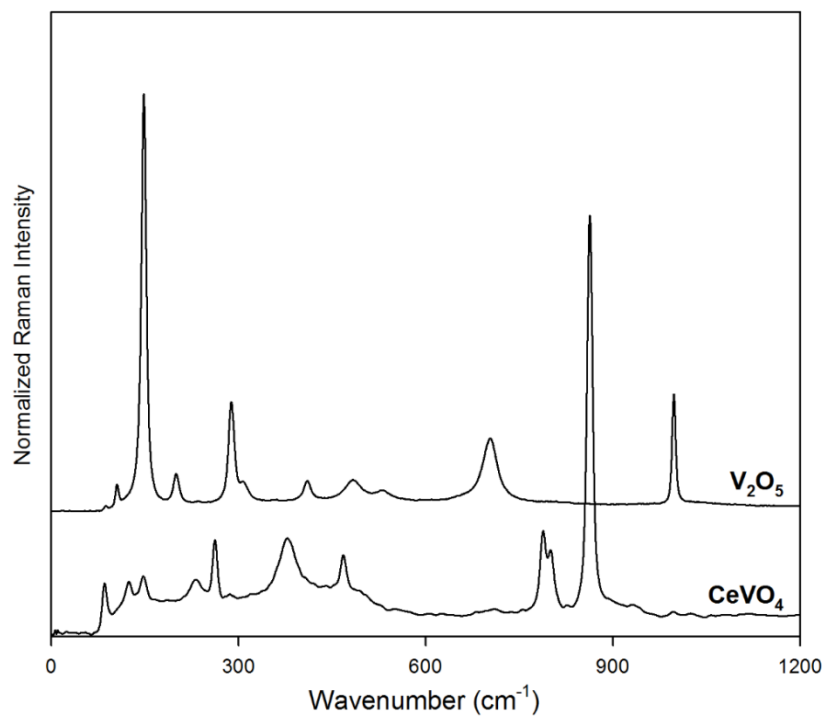
Figure 16 *Raman spectra of crystal V$_2$O$_5$ and CeVO$_4$. The V$_2$O$_5$ spectrum was normalized to band at 147 cm^{-1}, and the CeVO4 spectrum was normalized to band at 860 cm^{-1}.*
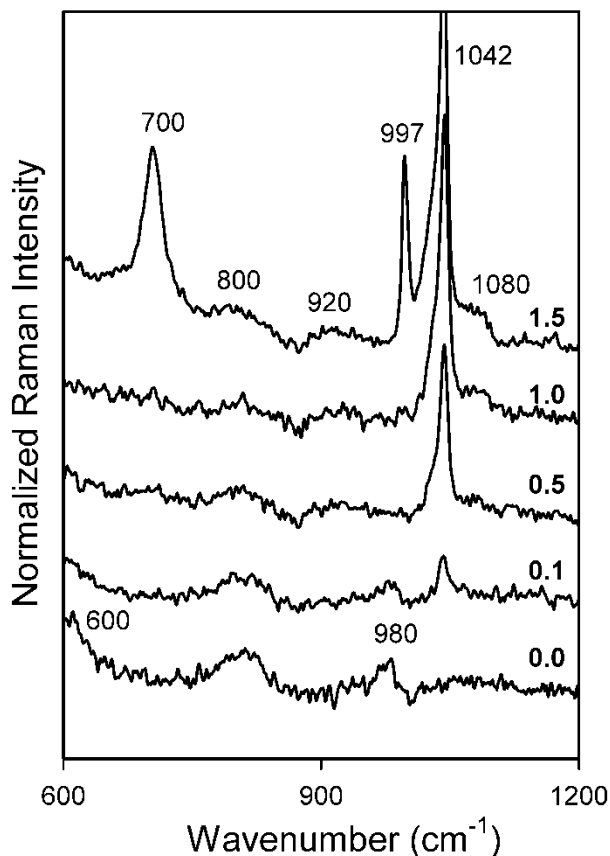
Figure 17 Raman spectra between 600 and 1200 cm^{-1} of supported vanadates on SiO$_2$, VOx/SiO$_2$. The spectra were normalized to the peak intensity of the broad SiO$_2$ band at 460 cm^{-1}.

Raman spectra for our VO$_x$/SiO$_2$ samples are presented in Figure 17, and our discussion highlights trends observed with increasing vanadium loading. First, the spectrum for the SiO$_2$ support (0.0) has broad bands at 600, 800 and 980 cm^{-1}. The band at 600 cm^{-1} corresponds to tricyclosiloxane rings, which are produced by the condensation of surface hydroxyls [89-91]; the band at 800 cm^{-1} is associated with Si-O-Si bonds [30, 92, 93]; and the band at 980 cm^{-1} is assigned to the stretching mode of surface silanols (Si-OH) [30, 92, 93]. As vanadium loadings increase, (0.1), SiO$_2$ bands remain evident; however, we also note the appearance of a band at

1042 cm^{-1}, which is assigned to the stretching mode of the V=O in the dispersed vanadate

species [94-96]. For VO$_x$/SiO$_2$ samples, this band is generally attributed to an isolated VO$_4$ in a

tetrahedral coordination environment [88, 95, 97]. As vanadium loading continues to increase

(0.5 – 1.5), we observe increasing intensity of the 1042 cm^{-1} band alongside decreasing intensity

of the bands at 600 cm^{-1}, 800 cm^{-1}, and 980 cm^{-1}. This stands to reason as increased vanadate

coverages should be facilitated by conversion of surface silanols and/or siloxanes into Si-O-V

bonds. At vanadium loadings above the theoretical monolayer coverage (1.5), we observe

formation of prominent bands at 700 and 997 cm^{-1}, which are associated with bulk V$_2$O$_5$

crystallites [98, 99]. As these bands are absent at and below 1.0 loadings, we conclude that

samples prepared from 0.1 to 1.0 vanadium loadings have primarily dispersed vanadium oxide

phases with minor fractions of bulk vanadates, while those prepared above 1.0 have both

dispersed and bulk phases. Interestingly, as one transitions from 0.1 to 1.5 vanadium loadings,

the intensity of the band at 1042 cm^{-1} increases without substantial broadening or peak shift. This

suggests that, despite a clear increase in vanadium oxide surface density, the nature of the

dispersed vanadate phase (e.g., monomeric vs. oligomeric) changes little in this set of materials

[100]. With increased vanadium loading, we also observe the appearance of bands at 920 cm^{-1}

and 1080 cm^{-1}; unfortunately, there has thus far been no conclusive structural assignment for

these bands. Most likely, they are attributed to Si-O$^-$ and Si-(O$^-$)$_2$ species perturbed by the

formation of V-O-Si bonds [81, 101] or, perhaps, to the V-O-Si bond itself [48, 102, 103]. We

see no definitive evidence of bands associated with V-O-V bonds, which should be observed in

the 750 cm^{-1} – 820 cm^{-1} range for VO$_x$/SiO$_2$ samples [48]. Note that the broad feature at 800 cm^{-1}

in the 1.5 sample may be attributed either to vibrational modes of SiO$_2$ (see 0.0) or to bulk V$_2$O$_5$

(see Figure 16); as such, we cannot take this band as a definitive polyvanadate signature. Based

on this this observation and the fact that increasing vanadium loading leads to neither broadening nor shift of the 1042 cm^{-1} band, we conclude that surface vanadates are mostly likely present as VO_4 monomers in this set of VO_x/SiO_2 samples. At coverages above 1.0, we also observe evidence of V_2O_5 crystallites.

Figure 18 summarizes Raman spectra obtained for VO_x/Al_2O_3 samples. γ-Al_2O_3 exhibits strong fluorescence, which dominates Raman spectra for 0.0, 0.1, and 0.5 samples. That said, a small band at 1024 cm^{-1} is evident in the 0.1 monolayer sample, and this band is shifted to 1037 cm^{-1} in the 0.5 monolayer sample (see inset). Raman bands in the region from 1020 cm^{-1} to 1040 cm^{-1} are assigned to terminal V=O stretching modes in the dispersed vanadium phase [87, 102, 104, 105]. The clear shift in the band position from 1024cm^{-1} to 1037cm^{-1} is most likely attributed to a transition from monomeric VO_4 in the 0.1 sample (1024 cm^{-1}) to polymeric vanadates in the 0.5 sample (1037 cm^{-1}) [51]. This conclusion is supported by the co-emergence of a broad band at 930 cm^{-1}, which is attributed to a V-O-V stretching mode [36, 82, 106]. We additionally note that, for 0.1 and 0.5 samples, there is no band at 997 cm^{-1}, which suggests that vanadium distributions in low-loading samples are comprised entirely of surface vanadates rather than a mixture of surface and bulk vanadium oxides. Transitioning to 1.0 and 1.5 monolayer samples, the band at 930 cm^{-1} (V-O-V) is shifted to 945 cm^{-1}, and its intensity increases. This suggests increased oligomerization of surface vanadium oxides in 1.0s and 1.5 samples. Further, the Raman bands at 700, 800 and 997 cm^{-1} become more pronounced in the 1.0 and 1.5 monolayer samples, which clearly indicates formation of bulk V_2O_5 crystallites at and above theoretical monolayer loadings [98, 99]. To summarize, in the VO_x/Al_2O_3 series, Raman spectra suggest that, as vanadium loadings increase, there is a transition from dispersed monomeric vanadium

oxides (0.1), to polymeric vanadates (0.5), to a mixture of polymeric vanadates and bulk V_2O_5

crystallites (1.0 and 1.5).
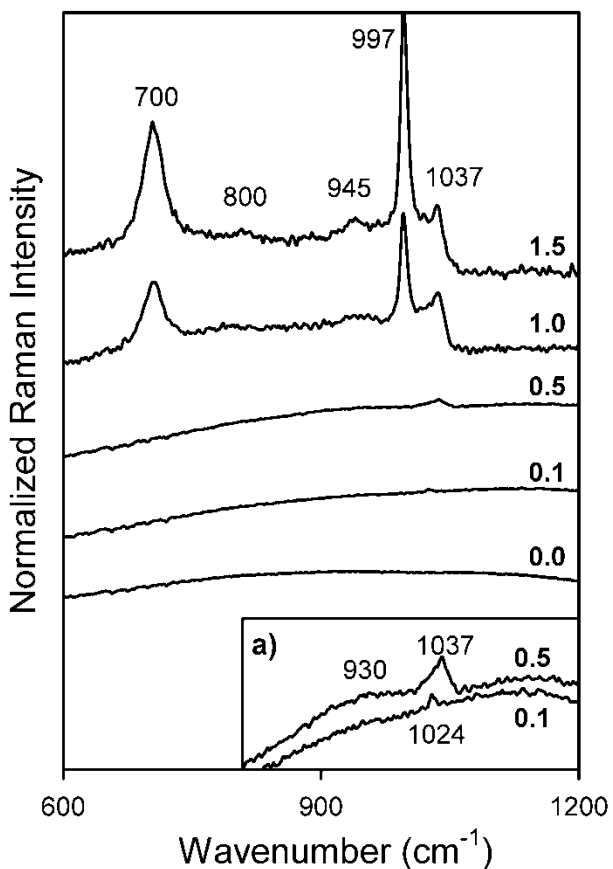
Figure 18 *Raman spectra* between 600 and 1200 cm^{-1} *of supported vanadates on γ-Al$_2$O$_3$, VO$_x$/Al$_2$O$_3$. Due to the absence of support bands, VO$_x$/Al$_2$O$_3$ spectra were normalized to spectral intensity at 1100 cm^{-1}, a) inset highlighting weak Raman bands in 0.1 and 0.5 monolayer samples.*

Raman spectra are summarized for the VO_x/TiO_2 samples in Figure 19. In all samples, the

prominent bands at 640 and 796 cm^{-1} are assigned to vibrations associated with the anatase phase

of TiO_2 [107, 108]. As VO_x loadings increase on the TiO_2 support, we observe a band at 1030

cm^{-1} (0.1), which is assigned to V=O stretching modes in dispersed vanadium oxides on the TiO_2

surface [83]. At higher loadings (0.5 – 1.5), this band's intensity increases slightly, and it shifts

to 1037 cm^{-1}, which likely reflects increasing oligomerization of surface vanadium oxides [80, 109]. This is supported by the concurrent emergence of a band at 920 cm^{-1} (0.5), which is attributed to V-O-V stretching modes in 2-dimensional polyvanadates [80, 109]. As vanadium loadings increase further (1.0 and 1.5), the intensity of this band increases, and it shifts to higher wavenumber, both of which are consistent with increased oligomerization of surface vanadium oxides [95]. Bands at 700 and 997 cm^{-1}, which are associated with V_2O_5 crystallites [98], are clearly observable alongside the 1037cm^{-1} band for 1.0 and 1.5 samples. Similar to the VO_x/Al_2O_3 series, we conclude that, as vanadium loading on TiO_2 increases from 0.1 to 1.5, there is a transition from monomeric tetrahedral vanadates, to polymeric vanadates, to a mixture of 2D (surface) and 3D (bulk crystalline) phases.
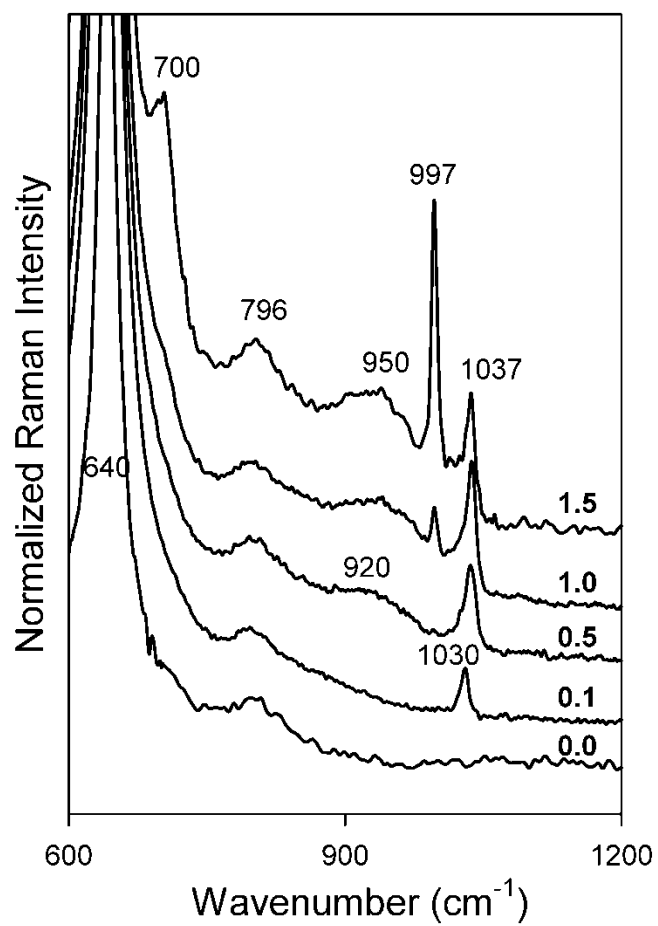
Figure 19 *Raman spectra* between 600 and 1200 cm^{-1} *of supported vanadates on TiO$_2$, VO$_x$/TiO$_2$. The spectra were normalized to the TiO$_2$ band at 640 cm^{-1}.*
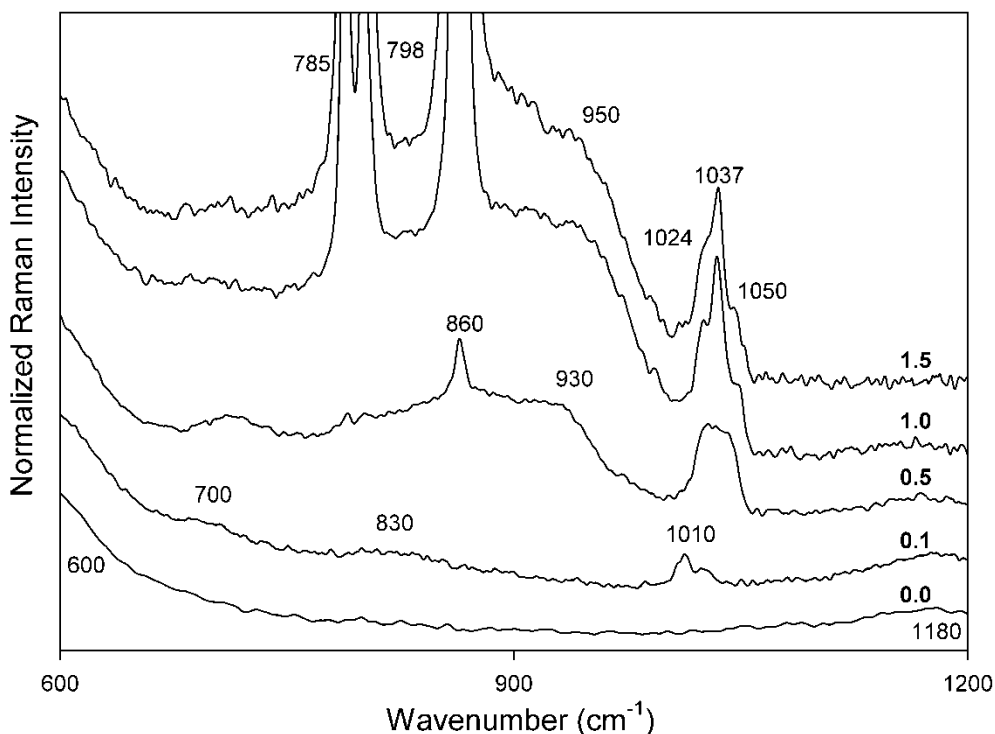
Figure 20 *Raman spectra* between 600 and 1200 cm^{-1} *of supported vanadates on CeO$_2$, VO$_x$/CeO$_2$. The spectra were normalized to the ceria band at 467 cm^{-1}.*

Finally, we consider Raman spectra for a series of VO$_x$/CeO$_2$ samples (Figure 20). In this spectral region, CeO$_2$ (0.0) has no strong Raman bands. At the lowest vanadium loading (0.1), we observe broad Raman bands at 700 cm^{-1} and 830 cm^{-1}, both of which are associated with the formation of V-O-Ce bonds [84, 110]. Further, we observe a more prominent band at 1010 cm^{-1}, which has a shoulder at 1024cm^{-1}. As in preceding discussions, bands in the 1010cm^{-1} – 1050cm^{-1} region are associated with V=O stretching modes in dispersed vanadium oxides [86, 111, 112]. The lower end of this wavenumber range is generally attributed to monomeric vanadates, while shifts to higher wavenumber are associated with increasing oligomerization in the dispersed vanadate phase [113]. Accordingly, we conclude that the vanadium oxide distribution in the 0.1 sample includes both monomers and oligomers; however, the size of the shoulder relative to that

of the main band suggests limited formation of an oligomer network. With increased vanadium loading (0.5), Raman bands corresponding to the V-O-Ce bond shift to higher wavenumbers (720cm^{-1} and 840cm^{-1}). Further, the vanadyl band at 1015 cm^{-1} is broadened and shifted to $\approx$1030 cm^{-1}, which suggests increased oligomer formation [88, 113]. In parallel, we observe concurrent appearance of a broad feature near 930 cm^{-1}, which is attributed to vibrational modes of V-O-V bonds and is thus consistent with increasing polyvanadate formation [52, 82, 86]. Finally, in the 0.5 sample, we begin to observe formation of a $CeVO_4$ phase, which is clearly indicated by pronounced Raman bands at 789, 801 and 863 cm^{-1} [114-116]. As loading increases further in 1.0 and 1.5 samples, we observe extensive formation of $CeVO_4$ aggregates, evidenced by the strong bands as 789 cm^{-1}, 801 cm^{-1}, and 863 cm^{-1}. Further, in these high loading samples, the surface vanadate distribution is dominated by polymeric species, which are indicated by V=O signatures at 1024cm^{-1}, 1037cm^{-1}, and 1050 cm^{-1} and by V-O-V modes at 950 cm^{-1}. All of these bands are shifted to higher wavenumbers relative to those observed in monomer-rich distributions, which is consistent with increasing polyvanadate formation.

A meaningful discussion of oxidative cleavage rates measured over catalysts that have varied supports and vanadium speciation necessitates approximation of turnover frequencies such that activity can be compared on a unit active site basis. This requires quantification of oxidation site densities in each material. To do so, we rely on methanol TPSO. Table 9 compiles evolved oxidation products and total oxidative capacity for all catalyst/support systems and bulk structures indicated by analysis of Raman spectra (V_2O_5 and $CeVO_4$). For reference, BET surface areas for all materials are additionally compiled in Table 9.

Table 9 *BET surface areas and oxidation site densities measured through methanol TPSR for all catalysts and supports.*

Support	Fraction of monolayer	Surface Area $(m^2\ g^{-1})$	HCHO $(\mu mol\ g^{-1})$	CO $(\mu mol\ g^{-1})$	CO_2 $(\mu mol\ g^{-1})$	Total O	
						$(\mu mol\ gcat^{-1})$	$(\mu mol\ \mu molV^{-1})$
	0	490	68	112	9	319	--
	0.1	501	44	96	3	245	1.33
SiO_2	0.5	442	176	248	27	753	0.87
	1	367	350	462	84	1526	0.95
	1.5	320	481	412	67	1506	0.67
	0	231	26	165	12	392	--
	0.1	234	24	168	10	390	1.31
γ-Al_2O_3	0.5	219	102	300	23	771	0.57
	1	176	206	187	21	643	0.27
	1.5	161	246	161	20	628	0.19
	0	49	23	54	2	137	--
	0.1	52.3	28	86	15	245	3.78
TiO_2	0.5	53.2	16	103	29	309	0.98
	1	47.1	45	112	17	320	0.52
	1.5	32.5	29	65	6	177	0.2
	0	75	10	205	4	432	--
	0.1	79.6	17	250	5	532	5.11
CeO_2	0.5	67.1	36	147	34	432	0.86
	1	48.2	53	55	8	187	0.19
	1.5	42.4	53	64	3	190	0.14
$CeVO_4$	--	24.1	30	18	4	78	0.02
V_2O_5	--	3.9	5	3	1	14	0.0013

Products from methanol TPSO include formaldehyde, carbon monoxide and carbon dioxide, and each product arises from methanol oxidation. Water is assumed as a co-product, and the requisite oxygen is assumed to come from reduction of the catalyst. Accordingly, we take the weighted sum of evolved quantities (equations 5 – 7) to give the total number of oxygen atoms that are both accessible and bound to a heteroatom that is feasibly reducible under TPSO conditions. Before proceeding, we offer the caveat that this titration method will interrogate sites that are active for methanol oxidation, and these sites are not necessarily identical to those

participating in oxidative ketone cleavage. Further, methanol TPSO provides no clear way to distinguish between distinct types of reducible surface sites. For example, methanol TPSO cannot resolve whether oxidation occurs at a single monomeric VO_4 site or at a vanadium center within an oligomeric phase. Finally, it is clear from data in Table 9 that supports (SiO_2, γ-Al_2O_3, TiO_2, and CeO_2) and bulk vanadium oxides (V_2O_5, $CeVO_4$) have latent oxidative capacity, which might arise either from inherent support reducibility or from the presence of reducible contaminants. Methanol TPSO lumps all of this complexity into a single site count, and it is important to bear these potentially confounding artifacts in mind when using this method to define site-time yields.

We next highlight meaningful trends in TPSO data. First, the total oxidation site density generally increases with vanadium loading. Despite the aforementioned uncertainty, this suggests that the bulk of oxidative capacity arises from vanadium species; however, the trend does not apply universally. Oxidation site counts often decrease as one exceeds theoretical monolayer loadings, and VO_x/CeO_2 catalysts display a contrasting trend in which oxidation site counts decrease with increasing vanadium loading. As discussed in detail below, these trends reflect both support contributions and changes in accessible vanadia surface area as speciation shifts from dispersed vanadium oxides to bulk aggregates.

The final column of Table 9 reports oxygen availability normalized by the total quantity of vanadium in each sample. Essentially, this presents a vanadium-normalized "dispersion" of oxidation sites. Methanol oxidation is generally accepted to occur through a Mars-van-Krevelen mechanism, which is predicated upon reduction of vanadium centers via transfer of lattice oxygen to surface adsorbates [36, 117]. The number of oxygen atoms contributed by a single vanadium center is dependent upon how deeply it is reduced during the catalytic cycle. For

example, an isolated VO_4 cluster could theoretically donate 4 oxygen atoms under conditions that are sufficiently reducing to form vanadium metal; however, this is implausible under the inert atmosphere of our TPSO experiments. In this case, vanadium atoms are reduced by donation of oxygen atoms to surface bound hydrocarbons, and formation of zerovalent vanadium seems unlikely. Typically, for a Mars-van-Krevelen mechanism, vanadium centers are assumed to cycle between V (5+) (e.g., a VO_4 site) and V (3+) (e.g., a VO_3 site), which suggests that each vanadium atom will contribute one oxygen atom per catalytic cycle [117, 118]. Accordingly, we expect that the upper limit of oxidation site dispersions should be 1.0 for 1D or 2D vanadium oxides as 100% of the vanadium centers are theoretically accessible in these cases. That said, Table 9 indicates that dispersions are always greater than one for 0.1 monolayer samples. Since deep reduction of VO_x clusters is unlikely, we attribute oxidation site dispersions above 1.0 to a substantial contribution of the support, and we again note that each support considered here has latent oxidative capacity during methanol TPSO. Consistent with this interpretation, apparent dispersions for 0.1 monolayer catalyst samples increase in the order $VO_x/SiO_2 \approx VO_x/ \gamma\text{-}Al_2O_3 <$ $VO_x/TiO_2 < VO_x/CeO_2$, a trend which likely reflects the increase in support reducibility as one moves from generally non-reducible SiO_2 and $\gamma\text{-}Al_2O_3$ to readily reducible CeO_2.

For each VO_x/support family, oxygen dispersions decrease monotonically with vanadium loading, and the extent of the decrease is support dependent. For example, the VO_x/SiO_2 series has dispersions ranging from $1.3 - 0.7$, while the VO_x/CeO_2 series is far more extreme, ranging from $5.1 - 0.14$. As noted above, dispersions larger than 1.0 are attributed to support contributions to the site count, which increase with support reducibility. Dispersions below 1.0 are attributed to the formation of bulk crystallites, which include V_2O_5 (SiO_2, $\gamma\text{-}Al_2O_3$ and TiO_2) and $CeVO_4$ (CeO_2). Both bulk structures have low surface areas (Table 9), which means that the

majority of their oxidation sites are inaccessible to adsorbates. Specifically, TPSO results indicate that there are, respectively, 0.0013 and 0.020 accessible oxygen atoms per vanadium atom in V_2O_5 and $CeVO_4$. Raman spectra broadly indicate that bulk structures become increasingly prevalent at high vanadium loadings and that the onset and extent of bulk phase formation increases in the order $VO_x/SiO_2 > VO_x\ TiO_2 \approx VO_x/\ \gamma\text{-}Al_2O_3 > VO_x/CeO_2$. This observation suggests that vanadium dispersions (i.e., the number of accessible oxidation sites per unit vanadium atom) should decrease in the same order, which is consistent with trends in oxidation site dispersions determined by methanol TPSO (Table 9).

The catalytic activity of each material during the oxidative cleavage of 2-pentanone is summarized in Figure 21. Rates are presented as site time yields, which represent the rate of oxidative cleavage of 2-pentanone (internal) per accessible lattice oxygen atom titrated by methanol TPSO (Table 9). All rates reflect initial reaction rates, i.e., those at zero time on stream. Error bars indicate 95% confidence intervals on the initial rate of reaction estimated from each decay profile. Although all supports considered in this study display some oxidative capacity, only CeO_2 is intrinsically active for 2-pentanone oxidation. This underscores the aforementioned concern that the spectrum of active sites sampled by methanol TPSO may not contribute equally to the oxidative cleavage of ketones, making it somewhat challenging to precisely define a site-time yield. Based on Figure 21, we conclude that observed rates of ketone oxidation over VO_x/SiO_2, $VO_x/\gamma\text{-}Al_2O_3$, and VO_x/TiO_2 are attributed entirely to vanadium oxides, whereas reactivity observed over VO_x/CeO_2 is likely comprised of separate contributions from CeO_x, VO_x, and $CeVO_x$ phases. We next focus on establishing the intrinsic reactivity of surface vanadium oxides in each catalyst system.
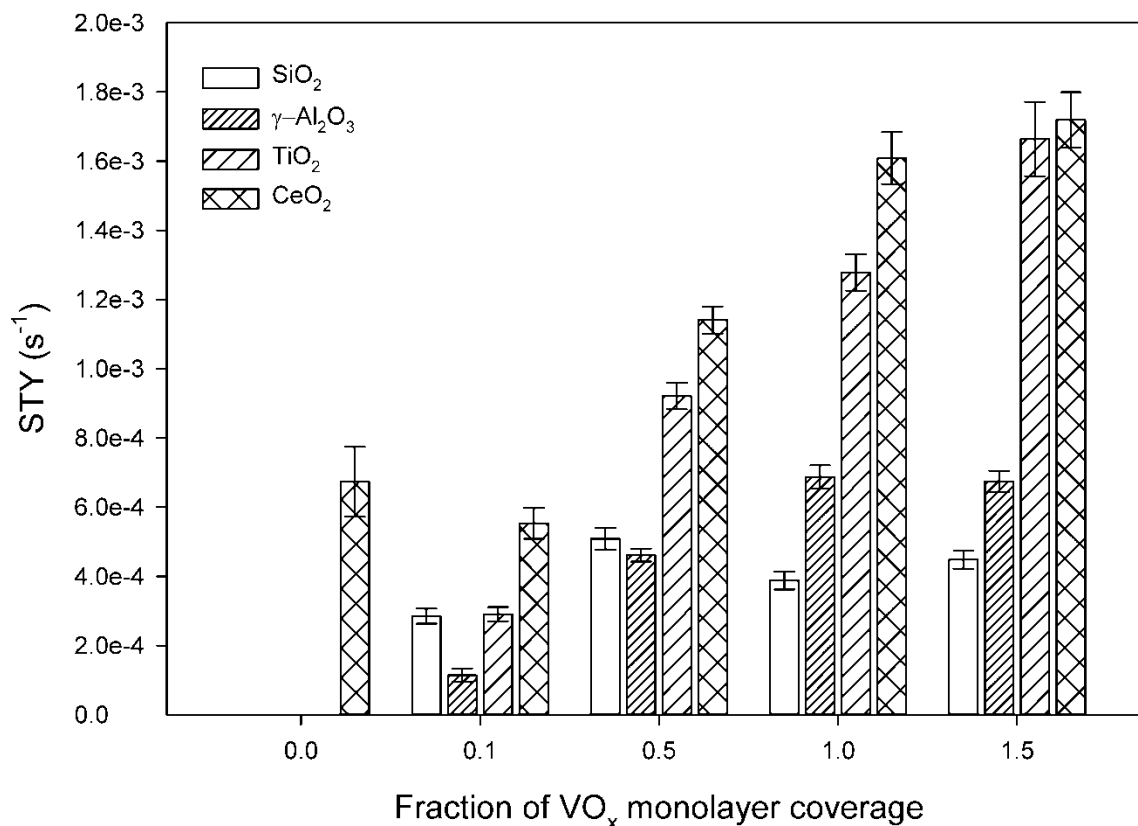
Figure 21 *2-pentanone internal oxidation turnover frequencies over VO$_x$ supported on SiO$_2$, γ-Al$_2$O$_3$, TiO$_2$, and CeO$_2$. T = 466K, 10 Torr 2-pentanone.*

In Figure 21, one observes that samples in the VO$_x$/SiO$_2$ series display site time yields ranging from 2.9 ± 0.2 x 10^{-4} s^{-1} (0.1 monolayer) to 5.1 ± 0.3 x 10^{-4} s^{-1} (0.5 monolayer). Values scatter around a mean of 4.1 ± 1.0 x 10^{-4} s^{-1}, suggesting that, in the VO$_x$/SiO$_2$ series, vanadium loading has little influence over site-time yields in the span of $0.1 - 1.5$ monolayer loadings. This is consistent with our Raman analysis which suggests that surface vanadium oxides in this VO$_x$/SiO$_2$ series are primarily monomeric and relatively insensitive to vanadium loading. Assuming that all reactivity can be attributed to dispersed vanadium oxides, there no reason to anticipate a change in activity as a function of vanadium loading in this system. For all other

catalyst series (excluding bare CeO_2), site time yields clearly increase as a function of vanadium loading, generally reaching a plateau in the $1.0 - 1.5$ monolayer range. There are two plausible explanations for this, which are addressed in detail below.

The first explanation is that oxidative cleavage is a structure sensitive reaction, and that intrinsic reactivity changes as vanadium distributions shift from monomer-rich to oligomer-rich on γ-Al_2O_3, TiO_2, and CeO_2. Specifically, oxidative ketone cleavage may require a pair of VO_x centers in close proximity. This mechanistic detail *could* manifest as an increase in observed site-time yields as vanadium speciation shifts away from isolated monovanadates and toward polyvanadates. At and above the monolayer limit, polyvanadates comprise the dominant dispersed vanadium oxide phase in all our samples, which should lead to a plateau in site-time-yields near monolayer coverage since the nature of surface sites become insensitive to vanadium loading in this regime. We further note that evidence of structure sensitivity over VO_x/Al_2O_3, VO_x/TiO_2, and VO_x/CeO_2 does not conflict with a lack thereof in our VO_x/SiO_2 samples. Raman analyses of the former materials show clear transitions from monomeric to polymeric vanadates in the range of 0.1 to 1.5 vanadium loadings, while Raman analysis of VO_x/SiO_2 suggests surface vanadates are primarily monomeric at all vanadium loadings. In general, pronounced sensitivity to the proximity of vanadium active sites is not widely reported for oxidative chemistries; however, the majority of prior reports consider alcohol oxidation [52, 118, 119] and alkane oxidative dehydrogenation [51, 54, 120, 121], which require transfer of a *single* lattice oxygen to complete the catalytic cycle. In contrast, although elementary mechanisms and rate controlling steps are not well-established for oxidative ketone scission, it is clear that transforming a ketone into carboxylic acid and aldehyde co-products requires transfer of two oxygen atoms. It is

therefore plausible that intrinsic rates of ketone oxidation might be higher at vanadium site pairs (e.g., in polyvanadates) than they are at isolated VO_4 monomers.

The second explanation for increasing site time yields as a function of vanadium loading is that oxidation site counts inferred from methanol TPSO include contributions from both the support and from vanadium oxides (Table 9); however, only vanadium oxides (with the exception of CeO_2) are active for oxidative cleavage under our reaction conditions. Because the supports are generally inert to oxidative ketone cleavage, active oxidation sites are over-counted by methanol TPSO when the support is partially exposed. This is especially problematic at low vanadium loadings and for samples that have poor vanadium dispersion as, in these cases, one expects sparse VO_x coverages and large fractions of exposed support surface area. This is supported by our observation of oxygen dispersions well above 1.0 for all of the 0.1 monolayer samples (Table 9). Inflated site counts would lead to artificially low site time yields on sparsely covered surfaces. As the VO_x coverage increases up to and beyond monolayer coverage, one expects that the majority of the exposed surface area in a given material becomes dominated by VO_x species rather than the bare support. At high loadings of vanadium on Al_2O_3, TiO_2, and CeO_2, all sites counted by methanol TPSO are attributed to a relatively uniform population of surface sites (i.e., those in polyvanadates). As the support no longer contributes to the active site count, observed site time yields no longer vary with vanadium loading.

Unfortunately, the characterization methods employed here are unable to quantitatively resolve the surface distribution of mono- and polyvanadate species, which makes it difficult to answer the question of whether reactivity indeed scales with the proximity of VO_x clusters. However, with the exception of the VO_x/SiO_2 series, we can state with some confidence that a) the accessible surface area in 1.0 and 1.5 monolayer catalyst samples is likely dominated by

vanadium oxides rather than exposed support and b) the distribution of accessible surface vanadium oxide sites in 1.0 and 1.5 monolayer samples is polyvanadate rich. (Note that VO_x/SiO_2 is excluded from this group since Raman spectra do not provide definitive evidence of polyvanadate formation on VO_x/SiO_2, whereas it is clearly indicated at high vanadium loadings on VO_x/Al_2O_3, VO_x/TiO_2, and VO_x/CeO_2.) Accordingly, we take site time yields estimated for VO_x/Al_2O_3, VO_x/TiO_2, and VO_x/CeO_2 in the high coverage limit to represent the intrinsic reactivity of dispersed, polymeric VO_x sites on each support. Based on the average of site time yields estimated at 1.0 and 1.5 monolayer coverages, intrinsic activities of supported vanadium oxides increase in the following order: VO_x/γ-Al_2O_3 (6.8 ± 0.1 x 10^{-4} s^{-1}) < VO_x/TiO_2 (15 ± 2.7 x 10^{-4} s^{-1}) $\approx VO_x/CeO_2$ (17 ± 0.8 x 10^{-4} s^{-1}). This result is in line with the frequent observation that support reducibility is a strong predictor of reactivity in heterogeneously catalyzed oxidations [55, 122-124]. An increase in intrinsic reactivity with the reducibility of the support cation suggests that reduction of the V-O-M bond is kinetically significant, which implies a Mars-van-Krevelen redox mechanism. Finally, it is worth noting that bare CeO_2 is intrinsically active for 2-pentanone oxidation, presenting a site time yield of 6.7 ± 1.0 x 10^{-4} s^{-1}. This is roughly a factor of 2 lower than that observed on vanadium oxide sites dispersed onto a CeO_2 support (17 ± 0.8 x 10^{-4} s^{-1}).

Despite their low surface areas and oxidation site counts (Table 9), bulk V_2O_5 and $CeVO_4$ have appreciable intrinsic activity during ketone oxidation. Under identical conditions to those used to generate Figure 21, measured site time yields of 2-pentanone oxidation over V_2O_5 and $CeVO_4$ are 25 ± 2.0 x 10^{-4} s^{-1} and 21 ± 0.9 x 10^{-4} s^{-1}. On a per-active site basis, bulk vanadate structures thus have comparable intrinsic reactivity to the most active of our supported vanadates. Raman spectra (Figures Figure *17* through Figure *20*) also indicate that catalysts with high vanadium

loadings are rich in bulk structures. Rates reported here are estimated based on species production rates, which are extensive quantities that reflect the sum of background reactivity, support reactivity, reactivity associated with dispersed vanadium oxides, and reactivity associated with bulk vanadium oxides. We have corrected data for background reactivity and have demonstrated (Figure 21) that, with the exception of CeO_2, supports do not contribute substantially to measured rates of oxidative cleavage under our reaction conditions. However, because bulk vanadate phases display a high intrinsic activity toward oxidative cleavage, and because Raman spectra indicate extensive formation of bulk phases in many samples, it is reasonable to ask whether they contribute substantially to measured reactivity in our system.

Based on their low surface areas and poor oxidation site accessibility, it is tempting to dismiss potential contributions of bulk structures outright; however, this depends on crystallite sizes for the bulk structures on the various supports. Nanoscale particles of either bulk phase could have appreciable surface area relative to their volume and thus display a higher oxidation site dispersion than the bulk samples that we have characterized in Table 8. We have not quantitatively assessed particle size distributions for bulk vanadium oxide structures present in supported catalysts; however, detailed analysis of Raman spectra is sufficient to exclude substantial bulk vanadate contributions to reactivity. In general, the width of Raman peaks scales inversely with the size of crystalline domains [125-129]. Single crystals display the lower limit on peak width, large bulk particles approach this limit, and small nanostructures show substantial broadening relative to this limit. Accordingly, Table 10 summarizes full width at half maxima (FWHM) for V_2O_5 and/or $CeVO_4$ phases where they are observed on VO_x/SiO_2, $VO_x/\gamma\text{-}Al_2O_3$, VO_x/TiO_2, and VO_x/CeO_2.

Table 10 *FWHM of peaks corresponding to V_2O_5 or C_eO_4 at 148, 285, 997,863 cm^{-1} for all the catalysts and the bulk structures.*

Peak location (cm^{-1})	V_2O_5	$CeVO_4$	SiO₂				γ-Al₂O₃				TiO₂				CeO₂			
			0.1	0.5	1.0	1.5	0.1	0.5	1.0	1.5	0.1	0.5	1.0	1.5	0.1	0.5	1.0	1.5
148	11	--	--	--	18	19	--	--	13	17	Nr	nr	nr	nr	--	--	--	--
285	12	--	--	--	24	17	--	--	14	18	--	--	10	11	--	--	--	--
997	9	--	--	--	Nr	nr	--	--	11	16	--	--	7	9	--	--	--	--
863	--	11	--	--	--	--	--	--.	--	--	--	--	--	--	--	--	10	8

A detailed analysis of peak widths indicates little difference between V_2O_5 and or $CeVO_4$ bands in supported catalysts and those in bulk samples, which suggests similarly sized crystalline domains. Therefore, where bulk structures are present in supported catalysts, their oxidation site densities can be reasonably approximated by those measured on bulk samples: 14 µmol g^{-1} for V_2O_5 and 78 µmol g^{-1} for $CeVO_4$. Based on these site densities, if one assumes the entire mass content of vanadium in VO_x/SiO_2, $VO_x/γ$-Al_2O_3 and VO_x/TiO_2 series is present as bulk V_2O_5, one predicts oxidation site counts that range from 0.1 – 1.1 µmol g^{-1}. Experimentally, methanol TPSO indicates oxidation site densities that are at least two orders of magnitude larger than this (Table 9), which suggests a minimal contribution from the bulk phase in VO_x/SiO_2, $VO_x/γ$-Al_2O_3 and VO_x/TiO_2 catalysts. Similarly, if one assumes the entire vanadium content in the VO_x/CeO_2 series is present in bulk $CeVO_4$ structures, one predicts oxidation site densities ranging from 2.1 to 27.5 µmol g^{-1}. These values are, in the most extreme case, an order of magnitude smaller than observed oxidation site densities, again suggesting that the bulk phase does not contribute substantially to measured site densities or reactivity in VO_x/CeO_2 samples.

5.4   Conclusions

In the loading ranges considered here, VO_x supported on SiO_2, $γ$-Al_2O_3, and TiO_2 exist as a diverse population of bulk V_2O_5 nanoparticles and dispersed, mono- and polyvanadates, whereas VO_x/CeO_2 exhibits surface mono- and polyvanadates and a bulk $CeVO_4$ phase. Based on

methanol TPSO and reactivity data, we conclude that both bulk V_2O_5 and $CeVO_4$ have considerable intrinsic reactivity toward the oxidative cleavage of 2-pentanone; however, their low surface areas translate to poor dispersion of reducible oxidation sites, and they have low activities per unit mass. When bulk structures are present alongside surface vanadates in a supported vanadium oxide, they do not contribute substantially to total site counts or rates of oxidative cleavage. Likely, this is due to the persistence of relatively large crystalline domains, which limits oxidation site accessibility and thus their extensive contributions to reactivity. When using methanol TPSO to assess oxidative capacity, exposed support surface area can contribute substantially to the total oxidation site count; however, SiO_2, γ-Al_2O_3, and TiO_2 are inert toward 2-pentanone oxidation under our reaction conditions. CeO_2 displays innate activity during the oxidative cleavage of 2-pentanone, but it is less active than vanadium oxides dispersed on the surface of CeO_2. We observe that site time yields for the oxidative cleavage of 2-pentanone increase with the extent of polyvanadate formation across multiple supports, which provides some evidence of structure sensitivity in this reaction; however, this conclusion is tempered by uncertainty in the use of methanol TPSO for the titration of oxidation sites. Measured site time yields in 2-pentanone oxidation also appear support-dependent, increasing in the order VO_x/γ-Al_2O_3 < VO_x/TiO_2 < VO_x/CeO_2, which likely reflects the underlying trend in support reducibility.

6 Developing Better Tools for Understanding the Acidity of Solid Acid Catalysts

6.1 Introduction

Lactone formation is one of the plausible pathways through which LA is transformed to MA. α-angelicalactone is formed by dehydration of LA (Scheme 17) which is most likely an enol mediated pathway.
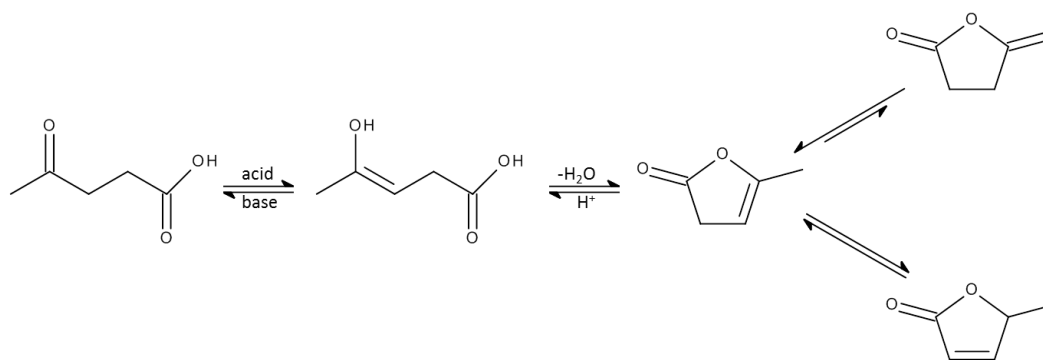
Scheme 17 *Angelicalactone formation through acid catalyzed dehydration of levulinic acid*

Acidity is required for the dehydration step and it is likely that the support might play an important role. The vanadium oxide catalysts we use always consist of a vanadia phase deposited on some metal oxide such as γ-Al_2O_3, SiO_2, TiO_2 and CeO_2 in order to attain well dispersed, high surface area, active catalysts. Some of these supports exhibit acidic properties and it is essential to develop the proper characterization tools so we can have a better understanding of the role that acidity plays in our system. Solid acid catalysts can have both Lewis and Brønsted acid sites. Basic molecules such as amines are used to titrate and characterize solid acids and among the methods used, the more popular ones are infrared spectroscopy (IR) and temperature

programmed desorption (TPD) of solid acid catalysts dosed with appropriate amines. Since vanadium oxide catalysts have a very diverse surface, including acid/base sites and redox sites in order to develop our understanding for the characterization methods we turned our attention to catalysts with a more uniform site distribution like aluminosilicates, including zeolites and amorphous silica alumina catalysts. Zeolites are probably the best known solid acid catalysts and while they occur naturally, development has led to the production of more than two hundred synthetic zeolites. Aluminosilicate zeolites are very well structured crystals composed of TO_4 tetrahedra, where T=Si, Al. For T=Si then the structure has a net charge of zero; however, for every Al atom inserted in the framework, a charge imbalance is created, which is mediated by the presence of a cation which, in the case of aluminosilicate zeolites, is usually a proton creating a Brønsted acid site[130]. Through previous attempts at solid acid characterization[63, 131] on amorphous silica alumina and MFI zeolites, we wanted to try and identify a universal probe that will adequately characterize a wide range of solid acids and that could also be used as an *in situ* titrant for determination of acid site density under reaction conditions. A broad range of zeolites was considered (ZSM-5, Zeolite beta, Zeolite Y, Mordenite and Ferrierite), while through a recent collaboration we had an opportunity to acquire three silicoaluminophosphate zeolites (SAPO-34, SAPO-56 and DNL-6). Additionally, two amorphous aluminosilicates ASA and gamma alumina were considered. Zeolites used in this study varied in SiO_2/Al_2O_3 ratio, framework type and subsequently pore size. Among the above zeolites, ZSM-5 was the most used in this study and while the framework is identical for all ZSM-5 catalysts, different SiO_2/Al_2O_3 ratios can be obtained. Accordingly, ratios ranged from 23:1 to 570:1. Pore size is another interesting parameter and varies with different zeolite frameworks.

Silicoaluminophosphate zeolites exhibit smaller pore sizes than ZSM-5, while beta, zeolite Y and mordenite have larger pore diameters than ZSM-5.

6.2   Materials and Methods

Physical properties of all the zeolites and amorphous materials are listed in Table 11.

Table 11 *Physical properties of aluminosilicate and silicoaluminophosphate catalysts*

Entry	Material	Framework type	Pore size (Å)	S_{BET} (m^2g^{-1})	SiO_2/Al_2O_3 molar ratio	SiO_2 wt.%	Al_2O_3 wt.%
1	SAPO-34	AFX	3.4 x 3.6	520			
2	SAPO-56	CHA	3.8 x 3.8	360			
3	DNL-6	RHO	3.6 x 3.6	140			
4	ZSM-5 (23:1)	MFI	5.1 x 5.5 / 5.3 x 5.6	343	23:1		
5	ZSM-5 (30:1)	MFI	5.1 x 5.5 / 5.3 x 5.6	380	30:1		
6	ZSM-5 (50:1)	MFI	5.1 x 5.5 / 5.3 x 5.6		50:1		
7	ZSM-5 (80:1)	MFI	5.1 x 5.5 / 5.3 x 5.6	390	80:1		
8	ZSM-5 (200-400:1)	MFI	5.1 x 5.5 / 5.3 x 5.6	360	200-400:1		
9	ZSM-5 (400-570:1)	MFI	5.1 x 5.5 / 5.3 x 5.6	360	400-570:1		
10	Beta	BEA	6.6 x 6.7 / 5.6 x 5.6		25:1		
11	Zeolite Y	FAU	7.4 x 7.4		12:1		
12	Mordenite	MOR	6.5 x 7.0 / 2.6 x 5.7		20:1		
13	Ferrierite	FER	4.2 x 5.4, 3.5 x 4.8		20:1		
14	SiAl 3113	n/a	mesoporous	610		85.1	13.7
15	SiAl 3901	n/a	mesoporous	420		77.8	12.4
16	γ-alumina	n/a	mesoporous	231		0	100

6.2.1   Temperature Programmed Desorption of Amines (TPD)

Brønsted site densities were determined using temperature programmed desorption (TPD) of alkylamines. Amines are typically dosed on a catalytic surface in order to titrate acid sites. Quantification of the desorbed amines gives a quantitative acid site count based on the assumption that each acid site is titrated by one amine molecule. The most common amine is ammonia which is also usually the most popular probe. Ammonia however, fails to discriminate

between Brønsted and Lewis acid sites which is often important, as certain reactions are Brønsted catalyzed while others are Lewis catalyzed[132]. One such type of exclusively Brønsted catalyzed reaction is the deamination of alkylamines, a Hoffman type elimination reaction that produces equimolar amounts of alkene and ammonia[133]. Furthermore, ammonia desorption happens at very low temperatures and it is impossible to distinguish between an ammonia molecule that was physically adsorbed and one that was chemically adsorbed, rendering acid site counting really challenging. Physical properties of the characterized materials are critical when choosing an appropriate probe molecule for characterization. This is true especially for zeolites as topography of those materials ranges based on framework type and thus, amines with kinetic diameter larger than the pore size of the zeolite will not be a good choice of probe. Silicoaluminophosphates for example, have pores of sizes up to 3.8 Å in diameter and cannot accommodate pyridine, which has a kinetic diameter of 5.85 Å similar to that of benzene[134]. For this reason, we used an array of different amines to probe the acidity of our catalysts ranging from the linear ethylamine to the bulky t-butylamine.

Silicoaluminophosphates (entries 1-3 in Table 11) were kindly provided from Moises Carreon at the Colorado School of Mines and their preparation is described elsewhere[135]. ZSM-5 zeolites (entries 4-8, 10-13) were obtained from Alfa Aesar in ammonium form, while ZSM-5 (400-570:1) was obtained from Acros Chemicals. Amorphous silica alumina catalysts were provided from Grace Davison and γ-alumina was obtained from Strem Chemicals. Prior to any experiments, all catalysts were heat treated at 723 K for 4 hours under 50sccm of air (Airgas, Ultra Zero) to remove impurities and bring zeolites to their H^+ form. In order to map out acid site densities, two characterization methods were employed; initially all catalysts underwent amine

temperature programmed desorption (TPD) and subsequently, Brønsted to Lewis acid site ratios were determined via pyridine FTIR.

Ammonia (Airgas, 1% NH3, 1% Ar, Balance He) Ethylamine (Sigma, 99%, canister under pressure), n-propylamine (Acros, 99%), 2-propylamine (Acros, 99%), n-butylamine (Acros, 99%) and tert-butylamine (Acros, 99%) were used as probe molecules. In a typical experiment, 50–150 mg of powdered catalyst were loaded onto a quartz wool plug inside of a ½" quartz tube. The tube was left to degas under vacuum at 523 K for 4 hours in a Micromeritics ASAP 2020 in order to accurately measure the dry mass of catalysts prior to any further steps. Subsequently the cell was positioned in a high temperature furnace (Omega, CRFC) and connected to a gas flow manifold as shown in Scheme 18. Catalysts were calcined for 4 hours at 723 K under 50 sccm of dry air (Airgas, Ultra Zero), cooled to 423 K, and purged for at least 120 min under 100 sccm of He that was dried over molecular sieves. Samples were then held at 423 K and contacted, until saturation, with the amine of choice. All amines except ammonia and ethylamine were vaporized at a partial pressure of 11 torr into a dry He sweep (100 sccm). Ammonia was dosed directly through the gas manifold, while ethylamine was introduced into the He stream via a 25µm ID capillary tube in order to create a pressure drop and permit introduction of ethylamine at low partial pressures. Saturation uptake was determined by continuously monitoring the amine signal in the off-gas using an online, mass-selective residual gas analyzer (Stanford Instruments RGA 100). Appropriate mass to charge ratios for all amines and alkenes are detailed in Table 12.
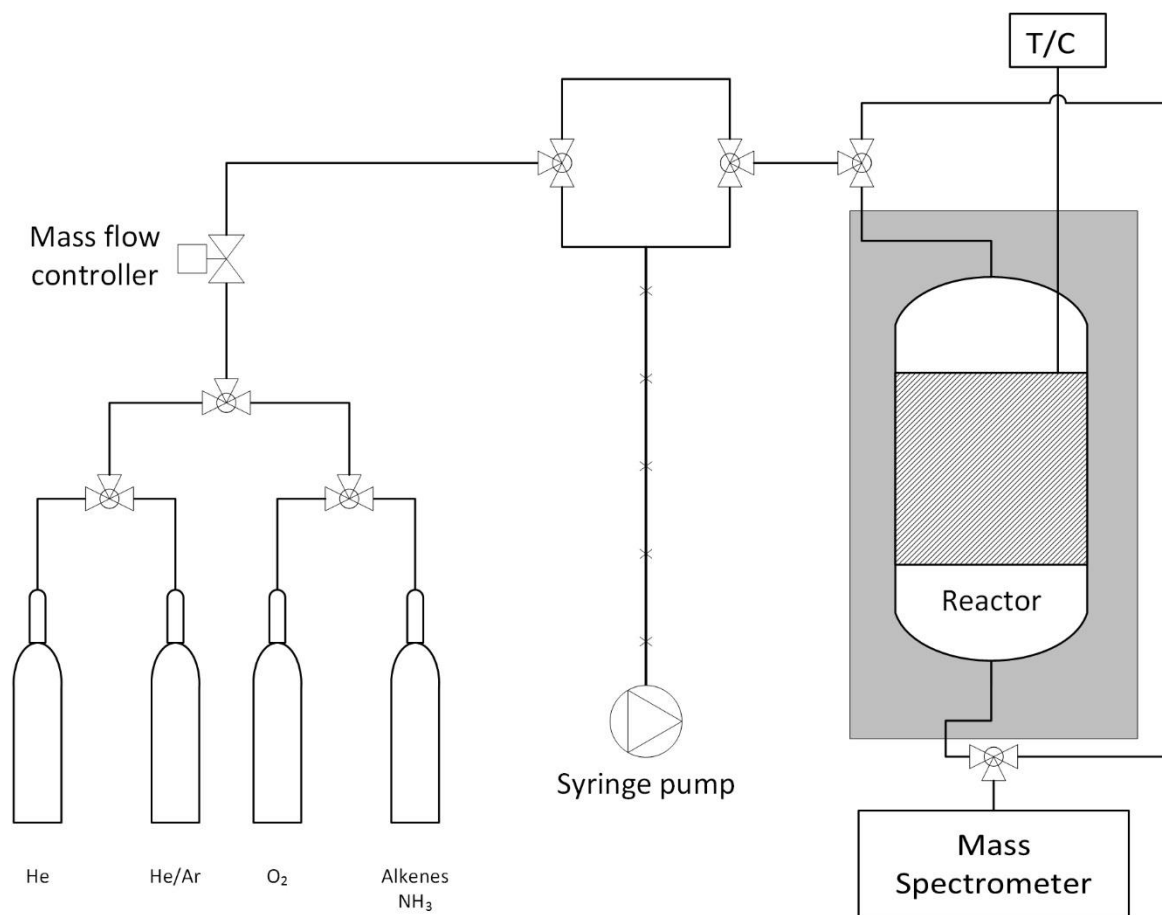
Scheme 18 *Temperature programmed desorption experimental setup*

Table 12 *Mass to charge ratios of monitored signals during temperature programmed desorption of amines*

Evolved species	Mass to charge ratio (m/z) of monitored signals
Ammonia	16
Ethylamine	30
n-propylamine	30
2-propylamine	44
n-butylamine	30
tlamine	58
Ethylene	27
Propylene	41
Butylene	41

After saturation, the cell was purged with 400 sccm of dry He for 60 minutes to remove

physisorbed amine and was then ramped to 973 K at a rate of 10 Kmin^{-1} under 400 sccm of dry

He containing 10,000 ppm of Ar as an internal standard. During the temperature ramp, the

effluent was monitored using the mass selective detector described above, which tracked signals

for Ar, molecularly desorbed amine, and evolved alkene. Raw MS signals were deconvoluted to

account for interference in the fragmentation patterns of the amine and the corresponding alkene.

Specifically, ethylamine and ethylene both yield an identical fragment (m/z = 27). Thus, the

signal for the apparent ethylene evolution (m/z = 27) was adjusted by subtracting 13.5% of the

m/z = 30 fragment in co-evolved ethylamine. 13.5% corresponds to the ratio of the intensity of

the m/z = 27 fragment to the m/z = 30 fragment in the MS pattern of ethylamine[136]. Likewise

5% of the signal of the m/z=30 fragment of n-propylamine was subtracted from the signal of

evolved propylene (m/z=41), while 3% of the m/z=30 of n-butylamine was subtracted from the

signal of evolved butylene (m/z=41) and finally, 20% of the m/z=58 of t-butylamine was

subtracted from the signal of evolved butylene (m/z=41). Brønsted site densities were calculated

from the corrected total evolved alkene based on the assumption that one molecule of alkene

forms at each accessible Brønsted site. Total Brønsted site density for each catalyst is presented

in Table 13.

Table 13 *Total site densities via ammonia TPD and Brønsted site densities via alkylamine TPD.*

Entry	Material	% of Brønsted acid sites (Pyridine FTIR)	Total acid site density (μmolg^{-1}) (NH$_3$ TPD)	Brønsted acid site density (μmolg^{-1}) (Alkylamine TPD)				
				C2	n-C3	i-C3	n-C4	t-C4
1	SAPO-34		507	442	107	0	0	0
2	SAPO-56		533	262	0	0	0	0
3	DNL-6		272	139	0	0	0	0
4	ZSM-5 (23:1)	95	997	1018	1185	1184	1028	1122
5	ZSM-5 (30:1)	92	488	690	741	699	622	616
6	ZSM-5 (50:1)	92	306	341	362	371	341	383
7	ZSM-5 (80:1)	92	181	320	313	327	282	351
8	ZSM-5 (200:1)	92	59	73	56	69	56	81
9	ZSM-5 (500:1)	94	48	33	29	28	26	60
10	Beta	64	439	404	734	834	682	902
11	Zeolite Y	74	528	494	626	653	534	785
12	Mordenite	97	912	1143	1181	1123	899	310
13	Ferrierite	96	563	944	938	558	842	12
14	SiAl 3113	26	242	86	68	164	147	311
15	SiAl 3901	39	223	43	13	82	51	190
16	γ-alumina		125	30	14	23	63	57

6.2.2 Pyridine FTIR

Furthermore, pyridine FTIR experiments were conducted on all zeolites, with the exception of silicoaluminophosphates, the pores (3.8Å in diameter) of which pyridine cannot access due to its large diameter (5.8 Å). The FTIR setup described previously in Scheme 15 was used for this set of experiments as well and pyridine dosing was performed *in situ*. Approximately 15-20 mg of catalyst was pressed into a thin pellet and loaded into the pellet holder where it was calcined at 723 K for 4 hours under 50 sccm of dry air from a purge gas generator. The cell was cooled down to 423 K and it was further purged with 100 sccm of dry He passed through a liquid nitrogen trap followed by a moisture trap. A spectrum of the clean catalyst was taken prior to dosing pyridine. Pyridine (Sigma, 99%) was then introduced into the He stream at a partial pressure of 10 torr until saturation of the pellet. He flow rate was increased to 400 sccm and the

cell was left to purge for approximately 2 hours to remove physisorbed pyridine. The spectrum of the clean catalyst was then subtracted from the chemisorbed pyridine spectrum resulting in a spectrum containing only the interactions between chemisorbed pyridine and catalyst surface. The two bands of interest (Figure 22b) are located at 1545 and 1455 cm^{-1} and reflect adsorbed pyridinium ion and pyridine, indicative of the adsorption of pyridine onto Brønsted and Lewis sites respectively[134].
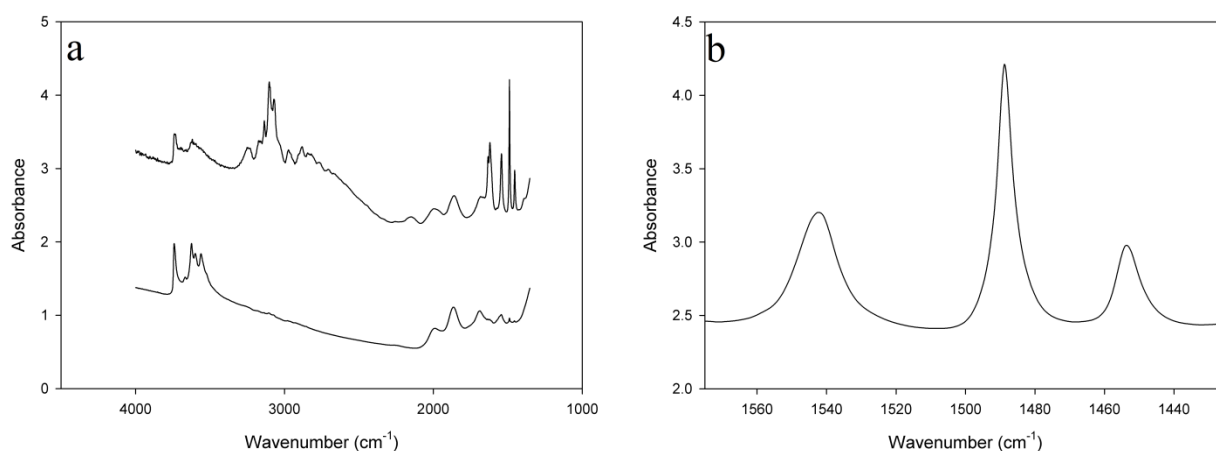
Figure 22 *a)Typical pyridine adsorption spectrum from FAU and b) detail on the interaction of pyridine with both Brønsted ans Lewis acid sites. The contribution at 1485 cm^{-1} comes from both types of acid sites and is therefore, not considered*

Appropriate molar extinction coefficients[137] were applied to the integrated areas of the two peaks before calculating the Brønsted to Lewis ratio. Brønsted to Lewis ratio is calculated based on Equation 15 and the % of Brønsted acid sites is presented in Table 13 along with the TPD data.

$$B:L = \frac{A_B/\varepsilon_B}{A_L/\varepsilon_L}, \quad \varepsilon_B = 1.67 \text{cm μmol}^{-1} \quad \varepsilon_L = 2.22 \text{cm μmol}^{-1} \tag{15}$$

where A_B and A_L are the areas of the Brønsted and Lewis peaks, and ε_B, ε_L the molar extinction coefficients.

6.3   Results and Discussion

At first glance, it is obvious that the only alkylamine suitable for determination of Brønsted site density in the silicoaluminaphosphate, small pored zeolites, is ethylamine. Any other alkylamine fails to access the pores of those zeolites which is not surprising as their pore openings range from 3.4x3.6 to 3.8x3.8 Å similar to the kinetic diameter of very small organic molecules such as methane and carbon monoxide[138]. The only other probe employed, capable of accessing the pores of silicoaluminaphosphate catalysts is ammonia. MFI zeolites (ZSM-5) show remarkable consistency when titrated with different types of amines. This is not surprising as ZSM-5 is known to have strong and very uniform acidity[132] and should only carry Lewis sites due to extra framework alumins (EFAL). Indeed, site counts from ammonia TPD agree well with site counts from alkylamine TPD. Size of probe molecule does not seem to affect the site count of ZSM-5. MFI pores have a diameter of 5.6 Å and can accommodate even the larger t-butylamine in the pores. Brønsted and total acid site densities decrease with increasing SiO_2/Al_2O_3 ratio, consistent with the drop in number of framework aluminum which is responsible for the bulk of acid sites in ZSM-5. Furthermore, FTIR data suggest that acidity in MFI seems to be very uniform despite changes in SiO_2/Al_2O_3 ratio, with Brønsted sites being responsible for 92-95 % of total acid sites. It is important to note here that while our characterization arsenal can predict acid site type and density, we cannot comment on the acid strength for any of the materials tested. As we move down along Table 13, the other two materials that are almost exclusively Brønsted acidic are Mordenite and Ferrierite (Entries 12-13). Acid site densities for MOR, with a 97% concentration of Brønsted acid sites, are consistent across all of the amines, with the

exception of t-butylamine. Total acid site count from ammonia agrees well with Brønsted site count as one would expect on a purely Brønsted catalyst. The reason for the low t-butylamine count might be due to sterics. MOR has a 12 ring channel with 7.0x6.5 Å opening and an 8 ring channel with a much smaller 2.6x5.7 Å pore opening. It is possible that t-butylamine can easily access Brønsted sites located in cavities accessed through the 12-ring channel (Figure 23a) but not the ones that require access through the narrower 8-ring channel[139]

a   b
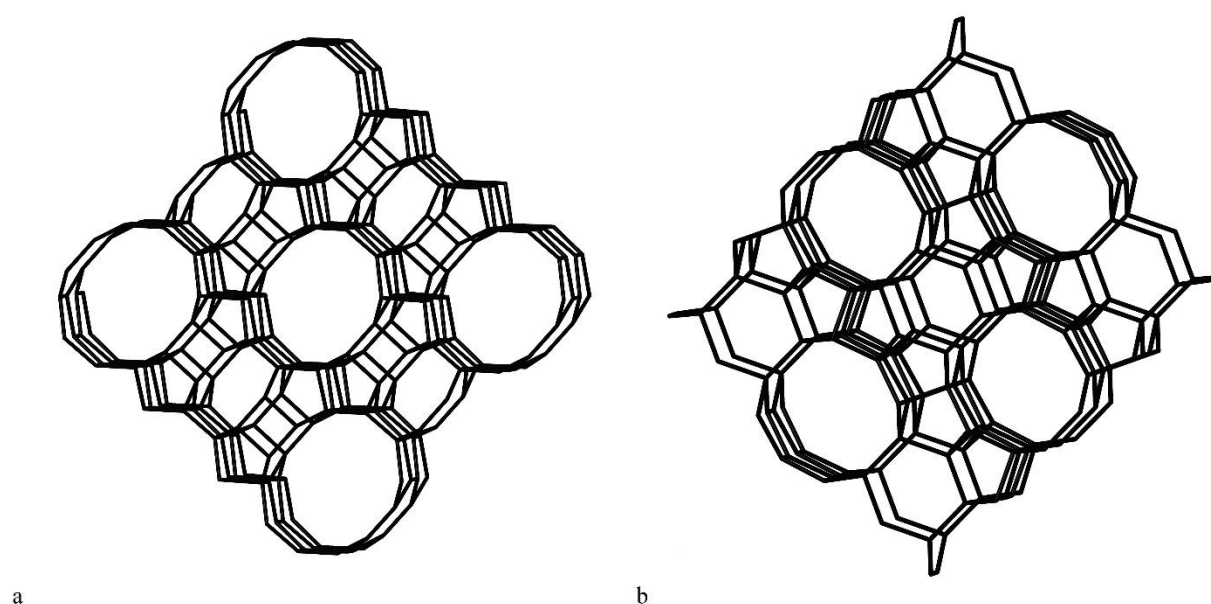
Figure 23 *a) MOR framework showing the larger 12-ring and smaller 8-ring channels, b) FER framework showing the larger 10-ring and smaller 8-ring channels[140].*

Ferrierite (Figure 23b) has a large 4.2x5.4 Å 10-ring channel system but it also has a narrower 3.5x4.8 Å 8-ring channel. Kinetic diameter data for alkylamines is hard to find; however, the kinetic diameter of isopropanol which we will assume is very similar to that of i-propylamine, is 4.8 Å[141]. It is possible that i-propylamine cannot access the 8-ring channels and that is the reason behind the apparent low acid site count with that probe (558 μmolg^{-1}). n-butanol whose size should not be all that different from n-butylamine, has a kinetic diameter of 5 Å[142] and is

slightly larger than that of isopropanol. Due to its linear nature however, it can titrate the bulk of the acid sites inside the pores of FER. The shape of t-butylamine combined with its relatively large diameter prohibits the titration of but a very few of acid sites ($12\mu molg^{-1}$) in FER.

Zeolite beta (BEA), zeolite Y (FAU) and the two amorphous silica alumina powders show a peculiar response to being dosed with different alkylamines. For FAU other than ethylamine and t-butylamine, site densities from the other alkylamines are in agreement. In order to understand trends in site densities from different amines, we turn to the data from the TPD experiments. In Figure 24 we take a closer look at the signals of evolved alkenes during deamination of different alkylamines on FAU.
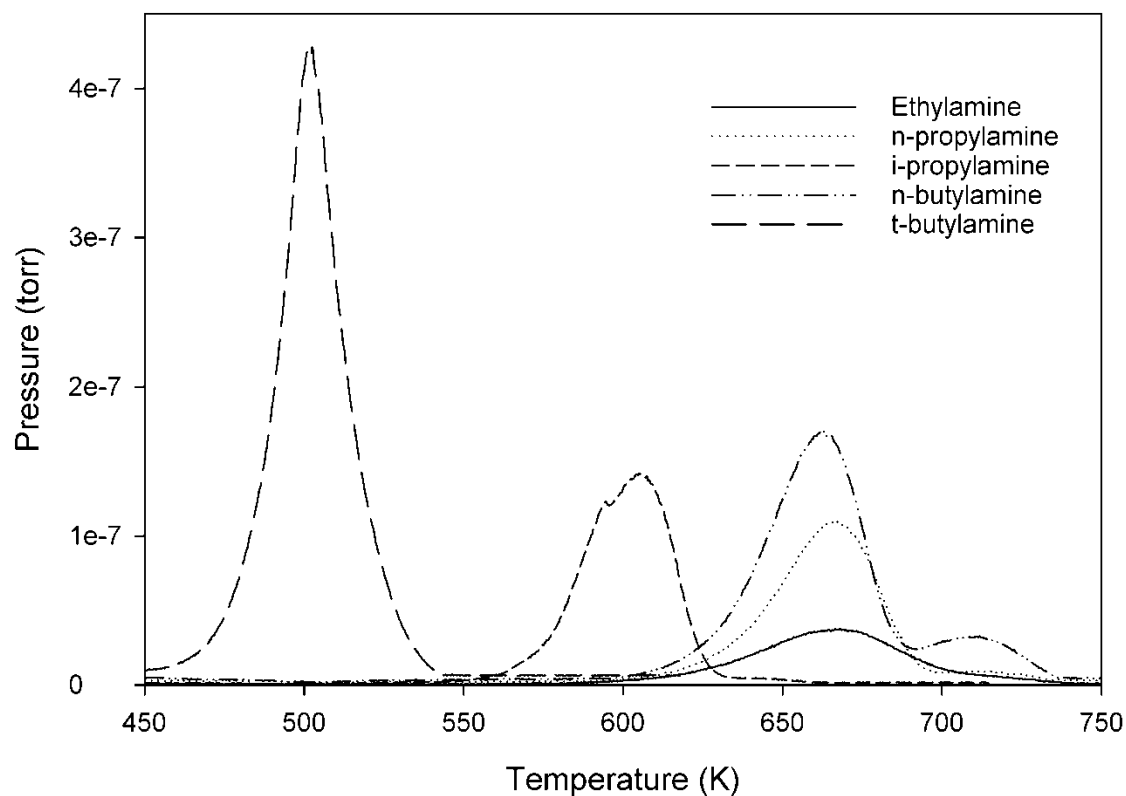
Figure 24 *Desorption temperature for alkenes under alkylamine TPDs in FAU zeolite. Legend designates the dosed alkylamine. Signals are from actual alkene evolutions.*

It is immediately apparent that certain alkylamines react with a simultaneous release of the alkene at different temperatures. This trend is not specific to zeolite Y. All materials tested exhibited the same temperature of maximum alkene evolution under same alkylamine deamination. This suggests that it is not the catalytic material that dictates deamination barrier but rather the type of alkylamine used. Indeed, it seems that amines possessing a primary α-carbon such as ethylamine, n-propylamine and n-butylamine deaminate between 600-700 K, the secondary α-carbon in i-propylamine facilitates deamination at lower temperatures of 550-650 K and lastly, t-butylamine having a tertiary α-carbon deaminates at much lower temperatures (450-550 K), consistent with previous observations[143]. It has also been suggested that the proton affinities of alcohols scale with the stability of the intermediate in alcohol dehydration over ZSM-5[144]. Therefore, we plot proton affinities of alkylamines along with average temperature of alkene evolution with respect to alkylamine type in Figure 25. Most probably, the increased proton affinity is an artifact of the structure of the amine; i.e., the tertiary α-carbon configuration satisfies both higher proton affinity and higher stability of the more substituted carbocation intermediate at the same time and thus, reaction is more likely than desorption for t-butylamine and i-propylamine, while linear alkylamines might undergo desorption prior to reaction. Acid site densities calculated in BEA, FAU and the two ASAs increase with increasing proton affinity of alkylamines and consequently, decrease with increasing deamination temperature. It is interesting to note here that, due to almost identical deamination temperatures for each alkylamine regardless of the material, deamination over a Brønsted site seems to be invariant with the physical properties of the solid acid. A Brønsted site seems to have similar

characteristics whether it is located in the micropores of a ZSM-5 zeolite or inside the mesopores

of an ASA.
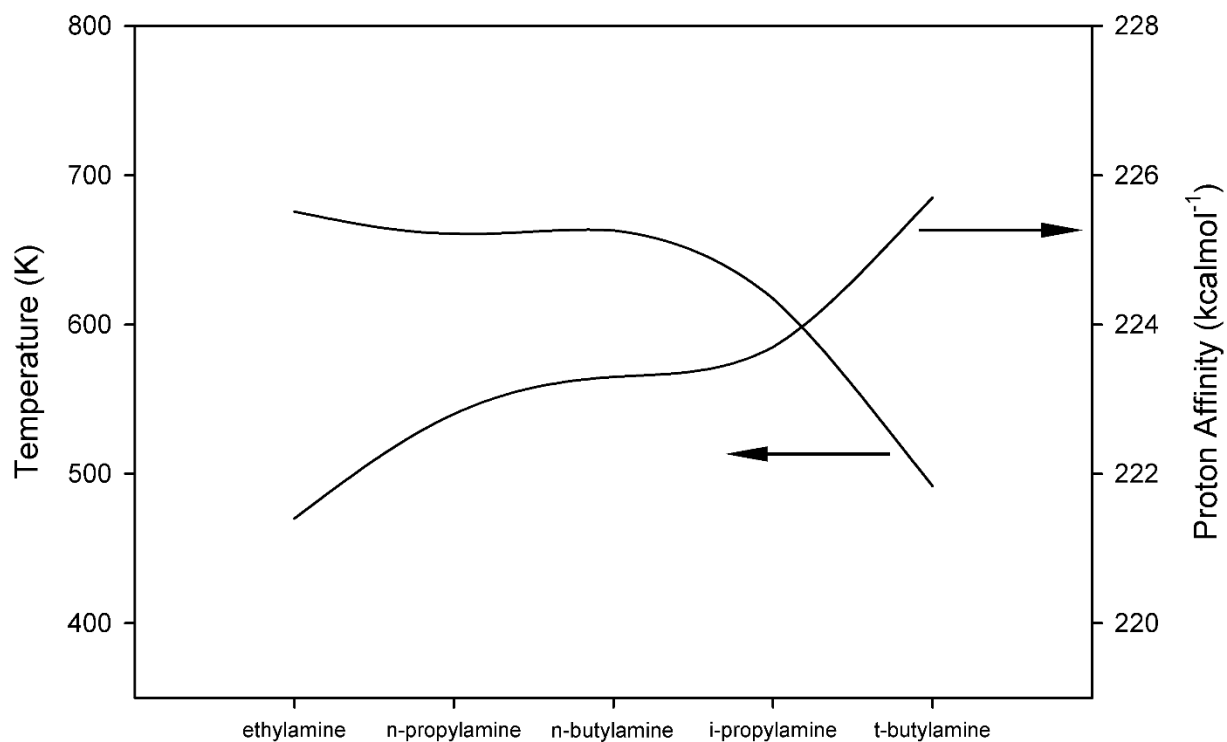
Figure 25 *Average temperature of alkene evolution along with proton affinities for all dosed alkylamines. Average temperature taken from all MFI, BEA, FAU, MOR, FER and the two ASA[145].*

In order to explain the varying site densities, seemingly dependent on the type of alkylamine, we

use the desorption signals of alkylamines and alkenes from FAU zeolite that is presented in

Figure 26.
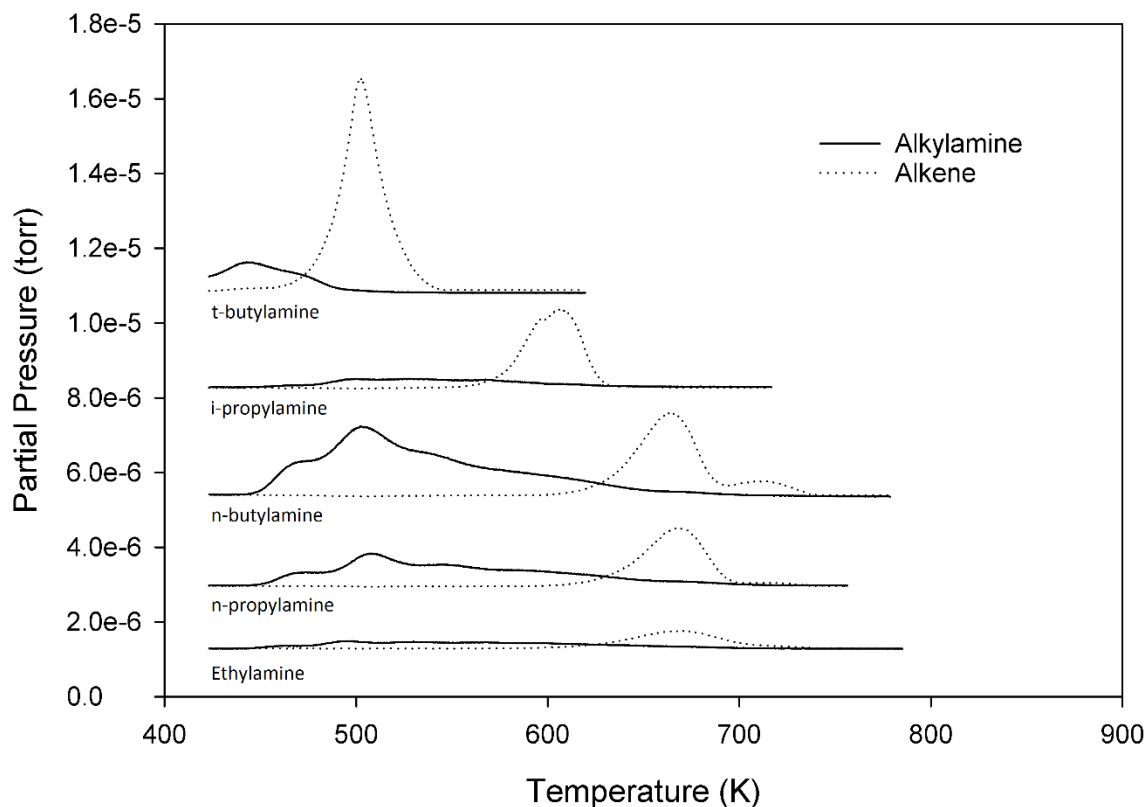
Figure 26 *Signals for alkylamine and alkene evolution during temperature programmed desorption of all available alkylamines*

A continuous desorption of alkylamine is observed on all TPD experiments up to deamination temperature. These are probably physisorbed species, or chemically adsorbed species on weak acid sites, the nature of which is unknown to us. Remarkably, desorption stops as soon as the energetic barrier for deamination is reached. The lower barrier for deamination of t-butylamine allows for the reaction to occur at much lower temperatures where the bulk of desorption has not yet occurred and thus, almost all of the adsorbed alkylamine deaminates. A similar trend is observed for i-propylamine and that is probably the reason why we see higher acid site counts on certain materials by i-propylamine and t-butylamine TPD. For linear butylamines, we notice a large desorption peak of unreacted amine relative to the alkene released during reaction, which

might explain the lower site counts we observe for those probes. In MFI we observe similar trends in the desorption of amines prior to reaction; however, site counts are almost identical across all probes. If we take a closer look at Table 13 we will notice that inconsistencies over site counts via different amines occur exclusive with materials that have acid site inhomogeneity, such as the ASA samples, FAU and BEA. Beta and zeolite Y are prone to dealumination through hydration and have been known to possess extra framework aluminum[146, 147], while the ASA samples have a high Lewis acid site density (Table 13). t-butylamine might present an excellent choice of base for acid site characterization, borrowing materials with small pores through which it cannot access the acid sites.

6.4 Alkylamines as *in situ* Reaction Probes

The above observations warrant a closer look at the kinetics of alkylamine deamination. Accordingly, we used the same setup to run deamination reactions with i-propylamine and test the catalytic activity of all the purely Bronsted materials (excluding ASA). Small pored zeolites were not considered due to their restricting small pore diameters. Instead of a mass spectrum detector, the effluent was analyzed via an FID detector on an HP-5890 gas chromatograph equipped with a gas sampling valve and an Agilent HP-1 column. Before reaching the GC, the effluent was scrubbed in a 1M H_2SO_4 solution to neutralize the unreacted i-propylamine and produced ammonia. Typically, 50-2200 mg of catalyst was supported by quartz wool plugs in a ½" quartz tube. The mass of each catalyst was adjusted in order to keep the total number on Brønsted sites constant. Prior to reactions the catalysts were calcined for 4 hours at 725 K under 50sccm of air (Airgas, Ultra Zero). 9.1 torr of i-propylamine were introduced into the reactor carried by a 50 sccm stream of He, which was previously passed through a moisture trap to remove any water. Initially, reaction temperature was set at 523 K and the reactor effluent was

left to reach steady state. Rates of deamination were recorded and were set as reference rates.

Temperature was raised to 548K and rates were collected at that temperature. At 548 K some

materials showed loss in activity. Rates were adjusted accordingly by fitting a simple 1st order

deactivation model. After the reactor was cooled back down to 523 K rates were compared with

the initial reference condition to validate the deactivation model. Rates were also collected at 483

K and apparent activation barriers were calculated. Partial pressure of i-propylamine was also

varied in order to gain insight in the reaction order. Site time yields (STY) were calculated by

using acid site densities of catalysts obtained by i-propylamine TPD. The summary of our

findings are presented in Table 14.

Table 14 *Kinetic parameters for i-propylamine deamination of aliminosilicates*

Entry	Material	Rate of production of propylene ($\mu molg^{-1}min^{-1}$)	STY (h^{-1})	Ea (kJ/mol)	Reaction order with respect to i-propylamine
4	ZSM-5 (23:1)	0.35	0.018	194±60	
5	ZSM-5 (30:1)	0.40	0.034	199±48	0
6	ZSM-5 (50:1)	0.20	0.032	209±41	0.02
7	ZSM-5 (80:1)	0.16	0.029	213±43	0.03
8	ZSM-5 (200:1)	0.03	0.023	208±16	0.02
9	ZSM-5 (500:1)	0.03	0.058	206±17	
10	Beta	0.53	0.038	145±10	0.26
11	Zeolite Y	0.23	0.021	162±15	0.05
12	Mordenite	0.37	0.020	183±66	0
13	Ferrierite	0.37	0.040	201±36	0.01

Apparent activation barriers for demanination of i-propylamine scatter around 200 kJmol^{-1} with

the exception of beta and Zeolite Y, where the apparent activation barrier is lower. The reaction

order with respect to i-propylamine is consistently zero with the exception of zeolite beta. The

apparent barriers tabulated above were extracted from simple Arrhenius plots. For catalysts on

which alkene production rate is zero order with respect to isopropylamine, i.e. the active sites are

populated exclusively by isopropylamine, the above apparent barriers describe energetics for

reactions where the forward rate is not controlled by equilibrium steps, whereas in the case of zeolite beta, where the order is non-zero, the barrier we experimentally extract is an apparent barrier, or a convolution of different energetics contributions. To accurately measure an activation barrier, we first consider the relationship for the apparent barrier which is described in Equation 18, derived from the Arrhenius expression as follows:

$$r_T = A \cdot e^{-E_{APP}/RT} \tag{15}$$

Rearranging Equation 15 we get:

$$\ln(r) = \ln(A) - \frac{E_{APP}}{RT} \tag{16}$$

An expression can be derived for E_{APP} as follows:

$$E_{APP} = RT^2 \frac{\partial \ln(r)}{\partial T} \tag{17}$$

Next, we need to have a rate expression in order to apply Equation 17. We will consider a simple model where an isopropylamine molecule adsorbs onto a Brønsted acid site. In a monomolecular fashion and reacts with the simultaneous release of propylene and ammonia as follows:

$$A + * \leftrightarrow A^* \qquad\qquad \text{step 1} \tag{18}$$

$$A^* \rightarrow P_1^* + P_2^* \qquad\qquad \text{step 2} \tag{19}$$

$$P_1 + * \leftrightarrow P_1^* \qquad\qquad \text{step 3} \tag{20}$$

$$P_2 + * \leftrightarrow P_2^* \qquad\qquad \text{step 4} \tag{21}$$

where A is isopropylamine, P_1 is propylene, P_2 is ammonia and * is a vacant Brønsted site. Steps 1,3,4 are likely equilibrated and so, for these equilibrated adsorption/desorption steps, forward rates of reaction will equate to the reverse rates of reaction as follows:

$$k_1 p_A \Theta^* = k_{-1} \Theta_A \qquad \text{and} \qquad \Theta_A = K_A p_A \Theta^* \tag{22}$$

$$k_3 p_{P_1} \Theta^* = k_{-3} \Theta_{P_1} \qquad \text{and} \qquad \Theta_{P_1} = K_{P_1} p_{P_1} \Theta^* \tag{23}$$

$$k_4 p_{P_1} \Theta^* = k_{-4} \Theta_{P_2} \qquad \text{and} \qquad \Theta_{P_2} = K_{P_2} p_{P_2} \Theta^* \tag{24}$$

$$\Theta_A + \Theta_{P_1} + \Theta_{P_2} + \Theta^* = 1 \tag{25}$$

where k_2 is the forward rate constant for step 2, K_A, K_{P_1}, K_{P_2} are the equilibrium constants for steps 1,3 and 4 respectively. Substituting equations 22-24 into Equation 25 we can get an expression for Θ^*:

$$\Theta^* = \frac{1}{1 + K_A p_A + K_{P_1} p_{P_1} + K_{P_2} p_{P_2}} \tag{26}$$

Assuming deamination as the rate limiting step we can construct the following general rate expression and further simplify it by using equations 22 and 26:

$$r = k_2 \Theta_A = k_2 K_A p_A \Theta^*$$

$$r = \frac{k_2 K_A p_A}{1 + K_A p_A + K_{P_1} p_{P_1} + K_{P_2} p_{P_2}} \tag{27}$$

By differentiating the rate with respect to temperature (Equation 17) we can get the following expression for the apparent barrier:

$$E_{APP} = RT^2 \frac{\partial \ln(r)}{\partial T}$$

$$E_{APP} = RT^2 \frac{\partial \ln\left(\dfrac{k_2 K_A p_A}{1 + K_A p_A + K_{P_1} p_{P_1} + K_{P_2} p_{P_2}}\right)}{\partial T}$$

$$E_{APP} = RT^2 \frac{\partial}{\partial T}\left[lnk_2 + lnK_A + lnp_A - \ln(1 + K_A p_A + K_{P_1} p_{P_1} + K_{P_2} p_{P_2}) \right]$$

For species i we have the equilibrium constant expression:

$$K_i = exp\left(\frac{-\Delta G_i}{RT}\right) = exp\left(\frac{\Delta S_i}{R}\right) exp\left(\frac{-\Delta H_i}{RT}\right)$$

And the apparent energy expression transforms into:

$$E_{APP} = RT^2 \frac{\partial}{\partial T} \left\{ \begin{array}{l} ln\left[A_2 \exp\left(-\frac{E_A}{RT}\right)\right] + ln\left[exp\left(\frac{\Delta S_A}{R}\right) exp\left(\frac{-\Delta H_A}{RT}\right)\right] + ln p_A - \\ \qquad ln(1 + K_A p_A + K_{P_1} p_{P_1} + K_{P_2} p_{P_2}) \end{array} \right\}$$

$$E_{APP} = RT^2 \frac{\partial}{\partial T} \left[\begin{array}{l} ln A_2 - \frac{E_A}{RT} + \frac{\Delta S_A}{R} - \frac{\Delta H_A}{RT} + ln p_A - \\ ln\left(1 + K_A p_A + K_{P_1} p_{P_1} + K_{P_2} p_{P_2}\right) \end{array} \right]$$

$$E_{APP} = RT^2 \left[0 + \frac{E_A}{RT^2} + \frac{\Delta H_A}{RT^2} + 0 \right.$$

$$\left. - \frac{\partial}{\partial T}\left(1 + K_A p_A + K_{P_1} p_{P_1} + K_{P_2} p_{P_2}\right) \frac{1}{1 + K_A p_A + K_{P_1} p_{P_1} + K_{P_2} p_{P_2}} \right]$$

$$E_{APP} = E_A + \Delta H_A - RT^2 \left(0 + p_A \frac{\partial K_A}{\partial T} + p_{P_1} \frac{\partial K_{P_1}}{\partial T} + p_{P_2} \frac{\partial K_{P_2}}{\partial T} \right) \Theta^*$$

$$E_{APP} = E_A + \Delta H_A$$

$$- RT^2 \left\{ p_A \frac{\partial\left[exp\left(\frac{\Delta S_A}{R}\right) exp\left(\frac{-\Delta H_A}{RT}\right)\right]}{\partial T} + p_{P_1} \frac{\partial\left[exp\left(\frac{\Delta S_{P_1}}{R}\right) exp\left(\frac{-\Delta H_{P_1}}{RT}\right)\right]}{\partial T} \right.$$

$$\left. + p_{P_2} \frac{\partial\left[exp\left(\frac{\Delta S_{P_2}}{R}\right) exp\left(\frac{-\Delta H_{P_2}}{RT}\right)\right]}{\partial T} \right\} \Theta^*$$

$$E_{APP} = E_A + \Delta H_A$$

$$- RT^2 \left[p_A \left(\frac{\Delta H_A}{RT^2} \right) exp \left(\frac{\Delta S_A}{R} \right) exp \left(\frac{-\Delta H_A}{RT} \right) \right.$$

$$+ p_{P_1} \left(\frac{\Delta H_{P_1}}{RT^2} \right) exp \left(\frac{\Delta S_{P_1}}{R} \right) exp \left(\frac{-\Delta H_{P_1}}{RT} \right)$$

$$\left. + p_{P_2} \left(\frac{\Delta H_{P_2}}{RT^2} \right) exp \left(\frac{\Delta S_{P_2}}{R} \right) exp \left(\frac{-\Delta H_{P_2}}{RT} \right) \right] \Theta^*$$

$$E_{APP} = E_A + \Delta H_A - RT^2 \left[K_A p_A \left(\frac{\Delta H_A}{RT^2} \right) + K_{P_1} p_{P_1} \left(\frac{\Delta H_{P_1}}{RT^2} \right) + K_{P_2} p_{P_2} \left(\frac{\Delta H_{P_2}}{RT^2} \right) \right] \Theta^*$$

$$E_{APP} = E_A + \Delta H_A - \Delta H_A K_A p_A \Theta^* - \Delta H_{P_1} K_{P_1} p_{P_1} \Theta^* - \Delta H_{P_2} K_{P_2} p_{P_2} \Theta^*$$

$$E_{APP} = E_A + \Delta H_A - \Theta_A \Delta H_A - \Theta_{P_1} \Delta H_{P_1} - \Theta_{P_2} \Delta H_{P_2}$$

$$E_{APP} = E_A + (1 - \Theta_A) \Delta H_A - \Theta_{P_1} \Delta H_{P_1} - \Theta_{P_2} \Delta H_{P_2} \tag{28}$$

We can simplify the above equation by assuming that propylene and ammonia, with adsorption enthalpies of -77 [148] and -145 kJ mol^{-1} [149] respectively, will not successfully compete for adsorption with isopropylamine which has an adsorption enthalpy of -205 kJ mol^{-1} [149] and their fractional coverage will probably be insignificant compared to the coverage of isopropylamine which is expected to dominate the surface. Accordingly Equation 28 can be simplified as follows:

$$E_{APP} = E_A + (1 - \Theta_A) \Delta H_A \tag{28}$$

All that remains is to correlate the coverage of isopropylmine with the reaction order with respect to isopropylamine partial pressure. The reaction order is given as the slope of the plot of the logarithm of the rate versus the logarithm of the partial pressure of the reactant. As such we have the following expression:

$$n_A = \frac{\partial \ln(r)}{\partial \ln(p_A)} = p_A \frac{\partial \ln(r)}{\partial p_A}$$

$$n_A = p_A \frac{\partial \ln(\frac{k_2 K_A p_A}{1 + K_A p_A + K_{P_1} p_{P_1} + K_{P_2} p_{P_2}})}{\partial p_A}$$

$$n_A = p_A \frac{\partial}{\partial p_A} \left[\ln(k_2) + \ln(K_A) + \ln(p_A) - \ln(1 + K_A p_A + K_{P_1} p_{P_1} + K_{P_2} p_{P_2}) \right]$$

$$n_A = p_A \left(\frac{1}{p_A} - \frac{K_A p_A}{1 + K_A p_A + K_{P_1} p_{P_1} + K_{P_2} p_{P_2}} \right)$$

$$n_A = 1 - K_A p_A \Theta^* = 1 - \Theta_A \tag{29}$$

By combining equations 28 and 29 we can construct the following expression:

$$E_A = E_{APP} - n_A \Delta H_A \tag{30}$$

In the case of zeolite beta for example, we can obtain an elementary barrier by correcting the apparent barrier with the use of Equation 30.

$$E_A = 145 - 0.26(-205) = 198.3 \text{ kJ mol}^{-1}$$

We can now define turnover frequency for a Brønsted catalyzed reaction as

$$TOF = {r}/{B_{sd}} \tag{14}$$

Where r is the measured rate of reaction and B_{sd} is the Brønsted site density measured by alkylamine TPD. Since the surface is saturated with alkylamine, the rates and consequently the TOF depends only on the pre-exponential and activation energy and can be written as

$$TOF = A \cdot \exp\left(-E_a / R \cdot T\right) \tag{15}$$

Where A is the pre exponential factor, E_a the activation barrier, R the universal gas constant and T the reaction temperature.

Combining equations 14 and 15 we can solve for Brønsted site density as follows

$$B_{sd} = r / A \cdot \exp\left(\frac{-E_a}{R \cdot T}\right) \tag{16}$$

Having plethora of rate data on different catalysts for i-propylamine deamination, we can construct an Arrhenius plot (Figure 27) from which we can calculate an activation barrier of $Ea = 193 \pm 18$ kJmol^{-1} and a pre-exponential of $A = 1.2 \cdot 10^{14} \, s^{-1}$. As long as we have a measured rate of reaction and we know the pre-exponential and activation energy, we can accurately predict the Brønsted site count of our catalyst.

It is very common for most catalysts during a chemical reaction to exhibit some extent of deactivation upon initial contact of the reactants making it thus hard to capture the initial rate of reaction which is a true measurement of the intrinsic activity of the catalyst. With the above formulation we can still measure intrinsic rates even on deactivated catalysts as long as the reaction we are studying is occurring exclusively over a Brønsted acid site.
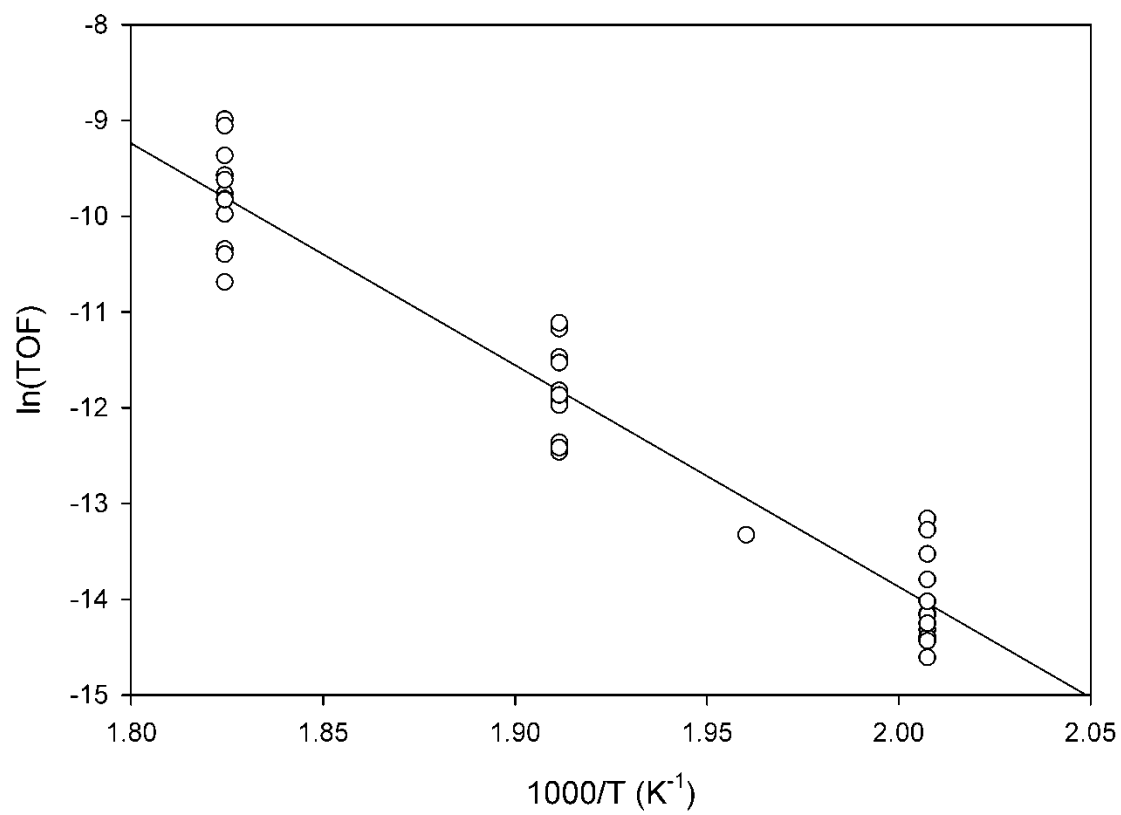
Figure 27 *Arrhenius plot of i-propylamine deamination across different materials*

References

[1] I.E. Wachs, Recent conceptual advances in the catalysis science of mixed metal oxide catalytic materials, Catalysis Today, 100 (2005) 79-94.

[2] E.M. Rubin, Genomics of cellulosic biofuels, Nature, 454 (2008) 841-845.

[3] R.L. Borup, M.A. Inbody, T.A. Semelsberger, J.I. Tafoya, D.R. Guidry, Fuel composition effects on transportation fuel cell reforming, Catalysis Today, 99 (2005) 263-270.

[4] A. Chatzidimitriou, J.Q. Bond, Oxidation of levulinic acid for the production of maleic anhydride: breathing new life into biochemicals, Green Chemistry, 17 (2015) 4367-4376.

[5] J.B. A. Aden, J. Holladay, J. White, A. Manheim, Top Value Added Chemicals From Biomass Volume I: Results of Screening for Potential Candidates from Sugars and Synthesis Gas in: G.P. T. Werpy (Ed.), NREL, 2004.

[6] D.M. Alonso, S.G. Wettstein, M.A. Mellmer, E.I. Gurbuz, J.A. Dumesic, Integrated conversion of hemicellulose and cellulose from lignocellulosic biomass, Energy & Environmental Science, 6 (2013) 76-80.

[7] G.M. Gonzalez Maldonado, R.S. Assary, J.A. Dumesic, L.A. Curtiss, Acid-catalyzed conversion of furfuryl alcohol to ethyl levulinate in liquid ethanol, Energy & Environmental Science, 5 (2012) 8990-8997.

[8] J.-P. Lange, E. van der Heide, J. van Buijtenen, R. Price, Furfural—A Promising Platform for Lignocellulosic Biofuels, ChemSusChem, 5 (2012) 150-166.

[9] B. Girisuta, L.P.B.M. Janssen, H.J. Heeres, Kinetic Study on the Acid-Catalyzed Hydrolysis of Cellulose to Levulinic Acid, Industrial & Engineering Chemistry Research, 46 (2007) 1696-1708.

[10] W.R.H. Wright, R. Palkovits, Development of Heterogeneous Catalysts for the Conversion of Levulinic Acid to γ-Valerolactone, ChemSusChem, 5 (2012) 1657-1667.

[11] D.M. Alonso, J.Q. Bond, J.A. Dumesic, Catalytic conversion of biomass to biofuels, Green Chemistry, 12 (2010) 1493-1513.

[12] E.I. Gürbüz, D.M. Alonso, J.Q. Bond, J.A. Dumesic, Reactive Extraction of Levulinate Esters and Conversion to γ-Valerolactone for Production of Liquid Fuels, ChemSusChem, 4 (2011) 357-361.

[13] J.-P. Lange, R. Price, P.M. Ayoub, J. Louis, L. Petrus, L. Clarke, H. Gosselink, Valeric Biofuels: A Platform of Cellulosic Transportation Fuels, Angewandte Chemie International Edition, 49 (2010) 4479-4483.

[14] J.C. Serrano-Ruiz, D.J. Braden, R.M. West, J.A. Dumesic, Conversion of cellulose to hydrocarbon fuels by progressive removal of oxygen, Applied Catalysis B: Environmental, 100 (2010) 184-189.

[15] D.M. Alonso, J.Q. Bond, J.C. Serrano-Ruiz, J.A. Dumesic, Production of liquid hydrocarbon transportation fuels by oligomerization of biomass-derived C9 alkenes, Green Chemistry, 12 (2010) 992-999.

[16] J.C. Serrano-Ruiz, D. Wang, J.A. Dumesic, Catalytic upgrading of levulinic acid to 5-nonanone, Green Chemistry, 12 (2010) 574-577.

[17] D.M. Alonso, J.Q. Bond, D. Wang, J.A. Dumesic, Activation of Amberlyst-70 for Alkene Oligomerization in Hydrophobic Media, Topics in Catalysis, 54 (2011) 447-457.

[18] J.Q. Bond, D. Wang, D.M. Alonso, J.A. Dumesic, Interconversion between γ-valerolactone and pentenoic acid combined with decarboxylation to form butene over silica/alumina, Journal of Catalysis, 281 (2011) 290-299.

[19] D.M. Alonso, S.G. Wettstein, J.Q. Bond, T.W. Root, J.A. Dumesic, Production of Biofuels from Cellulose and Corn Stover Using Alkylphenol Solvents, ChemSusChem, 4 (2011) 1078-1081.

[20] J.J. Bozell, L. Moens, D.C. Elliott, Y. Wang, G.G. Neuenscwander, S.W. Fitzpatrick, R.J. Bilski, J.L. Jarnefeld, Production of levulinic acid and use as a platform chemical for derived products, Resources, Conservation and Recycling, 28 (2000) 227-239.

[21] Quandl, Mont Belvieu Normal Butane, in, Mont Belvieu Normal Butane, https://www.quandl.com/data/CHRIS/CME_MNB1, 2017.

[22] Everchem, Benzene Update, in, Everchem Specialty Chemicals, 2017, pp. Current and Projected Benzene Prices.

[23] T.R. Felthouse, J.C. Burnett, S.F. Mitchell, M.J. Mummey, Maleic Anhydride, Maleic Acid, and Fumaric Acid, in: Kirk-Othmer Encyclopedia of Chemical Technology, John Wiley & Sons, Inc., 2000.

[24] V.V. Guliants, J.B. Benziger, S. Sundaresan, The oxidation of C4 molecules on vanadyl pyrophosphate catalysts, in: W.N.D.E.I. Joe W. Hightower, T.B. Alexis (Eds.) Studies in Surface Science and Catalysis, Elsevier, 1996, pp. 991-1000.

[25] Z. Na, Maleic Anhydride Chain - World Market Overview, in, Tecnon OrbiChem, 2015.

[26] A.P. Dunlop, S. Shelbert, Preparation of succinic acid, in, Google Patents, 1954.

[27] T. Seiyama, K. Nita, T. Maehara, N. Yamazoe, Y. Takita, Oxyhydrative scission of olefins, Journal of Catalysis, 49 (1977) 164-173.

[28] Y. Takita, K. Nita, T. Maehara, N. Yamazoe, T. Seiyama, Oxyhydrative scission of olefins, Journal of Catalysis, 50 (1977) 364-372.

[29] Y. Takita, T. Maehara, N. Yamazoe, T. Seiyama, Oxyhydrative scission of olefins, Journal of Catalysis, 104 (1987) 359-364.

[30] X. Gao, S.R. Bare, B.M. Weckhuysen, I.E. Wachs, In situ spectroscopic investigation of molecular structures of highly dispersed vanadium oxide on silica under various conditions, The Journal of Physical Chemistry B, 102 (1998) 10842-10852.

[31] AIST, Spectral Database for Organic Compounds SDBS, in, 2015.

[32] E. McCullagh, J. McMonagle, B. Hodnett, Kinetic study of the selective oxidation of butan-2-one to diacetyl over vanadium phosphorus oxide, Applied Catalysis A: General, 93 (1993) 203-217.

[33] E. McCullagh, J.B. McMonagle, B.K. Hodnett, Kinetic study of the selective oxidation of butan-2-one to diacetyl over vanadium phosphorus oxide, Applied Catalysis A: General, 93 (1993) 203-217.

[34] E. McCullagh, N.C. Rigas, J.T. Gleaves, B.K. Hodnett, Selective oxidation of butan-2-one to diacetyl over vanadium pentoxide, Applied Catalysis A: General, 95 (1993) 183-195.

[35] C.L. Perrin, A. Flach, M.N. Manalo, Decomposition of Malonic Anhydrides, Journal of the American Chemical Society, 134 (2012) 9698-9707.

[36] B.M. Weckhuysen, D.E. Keller, Chemistry, spectroscopy and the role of supported vanadium oxides in heterogeneous catalysis, Catalysis Today, 78 (2003) 25-46.

[37] T. Machold, W.Y. Suprun, H. Papp, Characterization of VOx-TiO2 catalysts and their activity in the partial oxidation of methyl ethyl ketone, Journal of Molecular Catalysis A: Chemical, 280 (2008) 122-130.

[38] A. Saytzeff, Zur Kenntniss der Reihenfolge der Analgerung und Ausscheidung der Jodwasserstoffelemente in organischen Verbindungen, Justus Liebigs Annalen der Chemie, 179 (1875) 296-301.

[39] P. Mars, D.W. van Krevelen, Oxidations carried out by means of vanadium oxide catalysts, Chemical Engineering Science, 3 (1954) 41-59.

[40] J. Liu, F. Mohamed, J. Sauer, Selective oxidation of propene by vanadium oxide monomers supported on silica, Journal of Catalysis, 317 (2014) 75-82.

[41] R. Fittig, 41. Ueber einige Derivate des Acetons, Justus Liebigs Annalen der Chemie, 114 (1860) 54-63.

[42] H.C. Brown, J.H. Brewster, H. Shechter, An Interpretation of the Chemical Behavior of Five- and Six-membered Ring Compounds1, Journal of the American Chemical Society, 76 (1954) 467-474.

[43] M.A. Hasan, M.I. Zaki, L. Pasupulety, Oxide-catalyzed conversion of acetic acid into acetone: an FTIR spectroscopic investigation, Applied Catalysis A: General, 243 (2003) 81-92.

[44] M.I. Zaki, M.A. Hasan, L. Pasupulety, Surface Reactions of Acetone on Al2O3, TiO2, ZrO2, and CeO2: IR Spectroscopic Assessment of Impacts of the Surface Acid–Base Properties, Langmuir, 17 (2001) 768-774.

[45] U. Bentrup, A. Brückner, C. Rüdinger, H.-J. Eberle, Elucidating structure and function of active sites in VOx/TiO2 catalysts during oxyhydrative scission of 1-butene by in situ and operando spectroscopy, Applied Catalysis A: General, 269 (2004) 237-248.

[46] I.E. Wachs, Catalysis science of supported vanadium oxide catalysts, Dalton Transactions, 42 (2013) 11762-11769.

[47] M.A. Banares, Supported metal oxide and other catalysts for ethane conversion: a review, Catalysis Today, 51 (1999) 319-348.

[48] N. Magg, B. Immaraporn, J.B. Giorgi, T. Schroeder, M. Bäumer, J. Döbler, Z. Wu, E. Kondratenko, M. Cherian, M. Baerns, Vibrational spectra of alumina-and silica-supported vanadia revisited: An experimental and theoretical model catalyst study, Journal of Catalysis, 226 (2004) 88-100.

[49] A. Dinse, B. Frank, C. Hess, D. Habel, R. Schomäcker, Oxidative dehydrogenation of propane over low-loaded vanadia catalysts: Impact of the support material on kinetics and selectivity, Journal of Molecular Catalysis A: Chemical, 289 (2008) 28-37.

[50] N. Das, H. Eckert, H. Hu, I.E. Wachs, J.F. Walzer, F.J. Feher, Bonding states of surface vanadium (V) oxide phases on silica: structural characterization by vanadium-51 NMR and Raman spectroscopy, The Journal of Physical Chemistry, 97 (1993) 8240-8243.

[51] M. Martinez-Huerta, X. Gao, H. Tian, I. Wachs, J. Fierro, M. Banares, Oxidative dehydrogenation of ethane to ethylene over alumina-supported vanadium oxide catalysts: Relationship between molecular structures and chemical reactivity, Catalysis Today, 118 (2006) 279-287.

[52] L.J. Burcham, I.E. Wachs, The origin of the support effect in supported metal oxide catalysts: in situ infrared and kinetic studies during methanol oxidation, Catalysis Today, 49 (1999) 467-484.

[53] A. Khodakov, B. Olthof, A.T. Bell, E. Iglesia, Structure and catalytic properties of supported vanadium oxides: support effects on oxidative dehydrogenation reactions, Journal of Catalysis, 181 (1999) 205-216.

[54] C.A. Carrero, C.J. Keturakis, A. Orrego, R. Schomäcker, I.E. Wachs, Anomalous reactivity of supported V 2 O 5 nanoparticles for propane oxidative dehydrogenation: influence of the vanadium oxide precursor, Dalton Transactions, 42 (2013) 12644-12653.

[55] G. Deo, I.E. Wachs, Reactivity of supported vanadium oxide catalysts: The partial oxidation of methanol, Journal of catalysis, 146 (1994) 323-334.

[56] L. Dong, Y. Chen, The dispersion of molybdena on ceria, Journal of the Chemical Society, Faraday Transactions, 92 (1996) 4589-4593.

[57] S. Mahapatra, G. Madras, T. Guru Row, Synthesis, characterization and photocatalytic activity of lanthanide (Ce, Pr and Nd) orthovanadates, Industrial & engineering chemistry research, 46 (2007) 1013-1017.

[58] T. Feng, J. Vohs, A TPD study of the partial oxidation of methanol to formaldehyde on CeO 2-supported vanadium oxide, Journal of Catalysis, 221 (2004) 619-629.

[59] T. Feng, J. Vohs, TPD–TGA and Calorimetric Study of the Partial Oxidation of Methanol on TiO 2-Supported Vanadium Oxide, Journal of Catalysis, 208 (2002) 301-309.

[60] R.Y. Saleh, I.E. Wachs, S.S. Chan, C.C. Chersich, The interaction of V2O5 with TiO2 (anatase): Catalyst evolution with calcination temperature and O-xylene oxidation, Journal of catalysis, 98 (1986) 102-114.

[61] I.E. Wachs, Raman and IR studies of surface metal oxide species on oxide supports: supported metal oxide catalysts, Catalysis Today, 27 (1996) 437-455.

[62] O.A. Abdelrahman, H.Y. Luo, A. Heyden, Y. Román-Leshkov, J.Q. Bond, Toward rational design of stable, supported metal catalysts for aqueous-phase processing: Insights from the hydrogenation of levulinic acid, Journal of Catalysis, 329 (2015) 10-21.

[63] J.Q. Bond, C.S. Jungong, A. Chatzidimitriou, Microkinetic analysis of ring opening and decarboxylation of γ-valerolactone over silica alumina, Journal of Catalysis, 344 (2016) 640-656.

[64] L.E. Briand, W.E. Farneth, I.E. Wachs, Quantitative determination of the number of active surface sites and the turnover frequencies for methanol oxidation over metal oxide catalysts: I. Fundamentals of the methanol chemisorption technique and application to monolayer supported molybdenum oxide catalysts, Catalysis Today, 62 (2000) 219-229.

[65] I.E. Wachs, The generality of surface vanadium oxide phases in mixed oxide catalysts, Applied Catalysis A: General, 391 (2011) 36-42.

[66] D.R. Stull, Vapor pressure of pure substances. Organic and inorganic compounds, Industrial & Engineering Chemistry, 39 (1947) 517-540.

[67] M. Ai, Activities for the decomposition of formic acid and the acid-base properties of metal oxide catalysts, Journal of Catalysis, 50 (1977) 291-300.

[68] G.Y. Popova, T. Andrushkevich, E. Semionova, Y.A. Chesalov, L. Dovlitova, V. Rogov, V. Parmon, Heterogeneous selective oxidation of formaldehyde to formic acid on V/Ti oxide catalysts: The role of vanadia species, Journal of Molecular Catalysis A: Chemical, 283 (2008) 146-152.

[69] G.Y. Popova, T. Andrushkevich, G. Zenkevich, Heterogeneous selective oxidation of formaldehyde over oxide catalysts. 2. Catalytic properties of V-Ti-oxide catalysts, Kinetika i Kataliz, 38 (1997) 285-288.

[70] W.E. Slink, P.B. DeGroot, Vanadium-titanium oxide catalysts for oxidation of butene to acetic acid, Journal of Catalysis, 68 (1981) 423-432.

[71] R.J. Madon, M. Boudart, Experimental Criterion for the Absence of Artifacts in the Measurement of Rates of Heterogeneous Catalytic Reactions, Industrial & Engineering Chemistry Fundamentals, 21 (1982) 438-447.

[72] S. Wasik, K. McCulloh, Measurements of gaseous diffusion coefficients by a gas chromatographic technique, J. Res. Natl Bur. Stand., 73 (1969).

[73] C.J. Geankoplis, Transport processes and unit operations, Allyn and Bacon, Boston, 1978

[74] W.L. McCabe, J.C. Smith, P. Harriot, Unit Operations of Chemical Engineering, McGraw Hill, Boston, 2001.

[75] M.A. Vannice, W.H. Joyce, Kinetics of catalytic reactions, Springer, 2005.

[76] H. Cheung, L.A. Bromley, C. Wilke, Thermal conductivity of gas mixtures, AIChE Journal, 8 (1962) 221-228.

[77] M.A. Vannice, Kinetics of Catalytic Reactions, Springer Science & Business Media, (2006).

[78] J.A. Dumesic, The Microkinetics of Heterogeneous Catalysis, AIChE Journal, (1994) 1-315.

[79] D.E. Keller, T. Visser, F. Soulimani, D.C. Koningsberger, B.M. Weckhuysen, Hydration effects on the molecular structure of silica-supported vanadium oxide catalysts: A combined IR, Raman, UV–vis and EXAFS study, Vibrational spectroscopy, 43 (2007) 140-151.

[80] G. Deo, I.E. Wachs, Effect of additives on the structure and reactivity of the surface vanadium oxide phase in V2O5/TiO2 catalysts, Journal of catalysis, 146 (1994) 335-345.

[81] X. Gao, S.R. Bare, J. Fierro, I.E. Wachs, Structural characteristics and reactivity/reducibility properties of dispersed and bilayered V2O5/TiO2/SiO2 catalysts, The Journal of Physical Chemistry B, 103 (1999) 618-629.

[82] I.E. Wachs, J.-M. Jehng, G. Deo, B.M. Weckhuysen, V. Guliants, J. Benziger, S. Sundaresan, Fundamental studies of butane oxidation over model-supported vanadium oxide catalysts: Molecular structure-reactivity relationships, Journal of catalysis, 170 (1997) 75-88.

[83] A. Christodoulakis, M. Machli, A.A. Lemonidou, S. Boghosian, Molecular structure and reactivity of vanadia-based catalysts for propane oxidative dehydrogenation studied by in situ Raman spectroscopy and catalytic activity measurements, Journal of Catalysis, 222 (2004) 293-306.

[84] M.V. Martínez-Huerta, G. Deo, J.L.G. Fierro, M.A. Bañares, Changes in ceria-supported vanadium oxide catalysts during the oxidative dehydrogenation of ethane and temperature-programmed treatments, The Journal of Physical Chemistry C, 111 (2007) 18708-18714.

[85] J.-M. Jehng, G. Deo, B.M. Weckhuysen, I.E. Wachs, Effect of water vapor on the molecular structures of supported vanadium oxide catalysts at elevated temperatures, Journal of Molecular Catalysis A: Chemical, 110 (1996) 41-54.

[86] Z. Wu, A.J. Rondinone, I.N. Ivanov, S.H. Overbury, Structure of vanadium oxide supported on ceria by multiwavelength raman spectroscopy, The Journal of Physical Chemistry C, 115 (2011) 25368-25378.

[87] M.D. Argyle, K. Chen, A.T. Bell, E. Iglesia, Effect of catalyst structure on oxidative dehydrogenation of ethane and propane on alumina-supported vanadia, Journal of Catalysis, 208 (2002) 139-149.

[88] Z. Wu, S. Dai, S.H. Overbury, Multiwavelength Raman spectroscopic study of silica-supported vanadium oxide catalysts, The Journal of Physical Chemistry C, 114 (2009) 412-422.

[89] B. Morrow, A. McFarlan, Chemical reactions at silica surfaces, Journal of non-crystalline solids, 120 (1990) 61-71.

[90] X. Gao, S.R. Bare, B.M. Weckhuysen, I.E. Wachs, In situ spectroscopic investigation of molecular structures of highly dispersed vanadium oxide on silica under various conditions, J. Phys. Chem. B, 102 (2001) 10842-10852.

[91] C. Brinker, R. Kirkpatrick, D. Tallant, B. Bunker, B. Montez, NMR confirmation of strained "defects" in amorphous silica, Journal of non-crystalline solids, 99 (1988) 418-428.

[92] Q. Sun, J.-M. Jehng, H. Hu, R.G. Herman, I.E. Wachs, K. Klier, In SituRaman Spectroscopy during the Partial Oxidation of Methane to Formaldehyde over Supported Vanadium Oxide Catalysts, Journal of Catalysis, 165 (1997) 91-101.

[93] M. Schraml-Marth, A. Wokaun, M. Pohl, H.-L. Krauss, Spectroscopic investigation of the structure of silica-supported vanadium oxide catalysts at submonolayer coverages, Journal of the Chemical Society, Faraday Transactions, 87 (1991) 2635-2646.

[94] C. Moisii, L.J. van de Burgt, A. Stiegman, Resonance raman spectroscopy of discrete silica-supported vanadium oxide, Chemistry of Materials, 20 (2008) 3927-3935.

[95] G.T. Went, S.T. Oyama, A.T. Bell, Laser Raman spectroscopy of supported vanadium oxide catalysts, Journal of Physical Chemistry, 94 (1990) 4240-4246.

[96] H. Eckert, I.E. Wachs, Solid-state vanadium-51 NMR structural studies on supported vanadium (V) oxide catalysts: vanadium oxide surface layers on alumina and titania supports, The Journal of Physical Chemistry, 93 (1989) 6796-6805.

[97] S.T. Oyama, G.T. Went, K.B. Lewis, A.T. Bell, G.A. Somorjai, Oxygen chemisorption and laser Raman spectroscopy of unsupported and silica-supported vanadium oxide catalysts, Journal of Physical Chemistry;(USA), 93 (1989).

[98] R. Baddour-Hadjean, J. Pereira-Ramos, C. Navone, M. Smirnov, Raman microspectrometry study of electrochemical lithium intercalation into sputtered crystalline V2O5 thin films, Chemistry of Materials, 20 (2008) 1916-1923.

[99] I.E. Wachs, J.-M. Jehng, W. Ueda, Determination of the chemical nature of active surface sites present on bulk mixed metal oxide catalysts, The Journal of Physical Chemistry B, 109 (2005) 2275-2284.

[100] L. Nguyen, S. Loridant, H. Launay, A. Pigamo, J. Dubois, J. Millet, Study of new catalysts based on vanadium oxide supported on mesoporous silica for the partial oxidation of methane to formaldehyde: Catalytic properties and reaction mechanism, Journal of Catalysis, 237 (2006) 38-48.

[101] S. Xie, E. Iglesia, A.T. Bell, Effects of hydration and dehydration on the structure of silica-supported vanadia species, Langmuir, 16 (2000) 7162-7167.

[102] Z. Wu, H.-S. Kim, P.C. Stair, S. Rugmini, S.D. Jackson, On the Structure of Vanadium Oxide Supported on Aluminas: UV and Visible Raman Spectroscopy, UV– Visible Diffuse Reflectance Spectroscopy, and Temperature-Programmed Reduction Studies, The Journal of Physical Chemistry B, 109 (2005) 2793-2800.

[103] S. Guimond, M.A. Haija, S. Kaya, J. Lu, J. Weissenrieder, S. Shaikhutdinov, H. Kuhlenbeck, H.-J. Freund, J. Döbler, J. Sauer, Vanadium oxide surfaces and supported vanadium oxide nanoparticles, Topics in catalysis, 38 (2006) 117-125.

[104] G.G. Cortez, M.A. Bañares, A Raman spectroscopy study of alumina-supported vanadium oxide catalyst during propane oxidative dehydrogenation with online activity measurement, Journal of Catalysis, 209 (2002) 197-201.

[105] J.M. Kanervo, M.E. Harlin, A.O.I. Krause, M.A. Bañares, Characterisation of alumina-supported vanadium oxide catalysts by kinetic analysis of H 2-TPR data, Catalysis today, 78 (2003) 171-180.

[106] G. Deo, I.E. Wachs, Predicting molecular structures of surface metal oxide species on oxide supports under ambient conditions, Journal of Physical chemistry, 95 (1991) 5889-5895.

[107] U. Balachandran, N. Eror, Raman spectra of titanium dioxide, Journal of Solid State Chemistry, 42 (1982) 276-282.

[108] X. Wang, J. Shen, Q. Pan, Raman spectroscopy of sol–gel derived titanium oxide thin films, Journal of Raman Spectroscopy, 42 (2011) 1578-1582.

[109] G.T. Went, L.-J. Leu, A.T. Bell, Quantitative structural analysis of dispersed vanadia species in TiO2 (anatase)-supported V2O5, Journal of Catalysis, 134 (1992) 479-491.

[110] C. Popa, M.a.V.n. Ganduglia-Pirovano, J. Sauer, Periodic Density Functional Theory Study of VO n Species Supported on the CeO2 (111) Surface, The Journal of Physical Chemistry C, 115 (2011) 7399-7410.

[111] M.A. Banares, G. Mestl, Structural characterization of operating catalysts by Raman spectroscopy, Advances in Catalysis, 52 (2009) 43-128.

[112] I.E. Wachs, C.A. Roberts, Monitoring surface metal oxide catalytic active sites with Raman spectroscopy, Chemical Society Reviews, 39 (2010) 5002-5017.

[113] M.V. Ganduglia-Pirovano, C. Popa, J. Sauer, H. Abbott, A. Uhl, M. Baron, D. Stacchiola, O. Bondarchuk, S. Shaikhutdinov, H.-J. Freund, Role of ceria in oxidative dehydrogenation on supported vanadia catalysts, Journal of the American Chemical Society, 132 (2010) 2345-2349.

[114] M. Banares, M. Martınez-Huerta, X. Gao, J. Fierro, I. Wachs, Dynamic behavior of supported vanadia catalysts in the selective oxidation of ethane: In situ Raman, UV–Vis DRS and reactivity studies, Catalysis today, 61 (2000) 295-301.

[115] W. Daniell, A. Ponchel, S. Kuba, F. Anderle, T. Weingand, D. Gregory, H. Knözinger, Characterization and catalytic behavior of VO x-CeO 2 catalysts for the oxidative dehydrogenation of propane, Topics in catalysis, 20 (2002) 65-74.

[116] U.O. Krašovec, B. Orel, A. Šurca, N. Bukovec, R. Reisfeld, Structural and spectroelectrochemical investigations of tetragonal CeVO 4 and Ce/V-oxide sol-gel derived ion-storage films, Solid State Ionics, 118 (1999) 195-214.

[117] I.E. Wachs, B.M. Weckhuysen, Structure and reactivity of surface vanadium oxide species on oxide supports, Applied Catalysis A: General, 157 (1997) 67-90.

[118] J. Döbler, M. Pritzsche, J. Sauer, Oxidation of methanol to formaldehyde on supported vanadium oxide catalysts compared to gas phase molecules, Journal of the American Chemical Society, 127 (2005) 10861-10868.

[119] T. Kim, I.E. Wachs, CH 3 OH oxidation over well-defined supported V 2 O 5/Al 2 O 3 catalysts: influence of vanadium oxide loading and surface vanadium–oxygen functionalities, Journal of Catalysis, 255 (2008) 197-205.

[120] S. Feyel, D. Schröder, X. Rozanska, J. Sauer, H. Schwarz, Gas-Phase Oxidation of Propane and 1-Butene with [V3O7]+: Experiment and Theory in Concert, Angewandte Chemie International Edition, 45 (2006) 4677-4681.

[121] K. Chen, E. Iglesia, A.T. Bell, Kinetic isotopic effects in oxidative dehydrogenation of propane on vanadium oxide catalysts, Journal of Catalysis, 192 (2000) 197-203.

[122] J. Haber, Supported Vanadium Oxide Catalysts:'Molecular Structural Characterization and Reactivity Properties, Critical Reviews in Surface Chemistry, 4 (1994) 141-187.

[123] J. Haber, A. Kozlowska, R. Kozłowski, The structure and redox properties of vanadium oxide surface compounds, Journal of Catalysis, 102 (1986) 52-63.

[124] T. Blasco, J.L. Nieto, Oxidative dyhydrogenation of short chain alkanes on supported vanadium oxide catalysts, Applied Catalysis A: General, 157 (1997) 117-142.

[125] G. Gouadec, P. Colomban, Raman spectroscopy of nanomaterials: how spectra relate to disorder, particle size and mechanical properties, Progress in Crystal Growth and Characterization of Materials, 53 (2007) 1-56.

[126] W. Weber, K. Hass, J. McBride, Raman study of CeO 2: second-order scattering, lattice dynamics, and particle-size effects, Physical Review B, 48 (1993) 178.

[127] I. Kosacki, T. Suzuki, H.U. Anderson, P. Colomban, Raman scattering and lattice defects in nanocrystalline CeO 2 thin films, Solid State Ionics, 149 (2002) 99-105.

[128] R. Nemanich, S. Solin, R.M. Martin, Light scattering study of boron nitride microcrystals, Physical Review B, 23 (1981) 6348.

[129] M. Fujii, S. Hayashi, K. Yamamoto, Growth of Ge microcrystals in SiO2 thin film matrices: a Raman and electron microscopic study, Japanese Journal of Applied Physics, 30 (1991) 687.

[130] P. Payra, P. Dutta, Zeolites, in: Handbook of Zeolite Science and Technology, CRC Press, 2003.

[131] A.B. Kellicutt, R. Salary, O.A. Abdelrahman, J.Q. Bond, An examination of the intrinsic activity and stability of various solid acids during the catalytic decarboxylation of [gamma]-valerolactone, Catalysis Science & Technology, 4 (2014) 2267-2279.

[132] R.J. Gorte, What do we know about the acidity of solid acids?, Catalysis Letters, 62 (1999) 1-13.

[133] W.E. Farneth, R.J. Gorte, Methods for Characterizing Zeolite Acidity, Chemical Reviews, 95 (1995) 615-635.

[134] T. Barzetti, E. Selli, D. Moscotti, L. Forni, Pyridine and ammonia as probes for FTIR analysis of solid acid catalysts, Journal of the Chemical Society, Faraday Transactions, 92 (1996) 1401-1407.

[135] S.M. Bruce, Z. Zong, A. Chatzidimitriou, L.E. Avci, J.Q. Bond, M.A. Carreon, S.G. Wettstein, Small pore zeolite catalysts for furfural synthesis from xylose and switchgrass in a γ-valerolactone/water solvent, Journal of Molecular Catalysis A: Chemical, 422 (2016) 18-22.

[136] S.E.S. NIST Mass Spectra Data Center, Director, Mass Spectra, in: P.J. Linstrom, W.G. Mallard (Eds.), NIST Chemistry Webbook, NIST Standard Reference Database Number 69, National Institute of Standards and Technology, Gaithersburg MD, 20899, <**Error! Hyperlink reference not valid.**.

[137] C.A. Emeis, Determination of Integrated Molar Extinction Coefficients for Infrared Absorption Bands of Pyridine Adsorbed on Solid Acid Catalysts, Journal of Catalysis, 141 (1993) 347-354.

[138] N. Mehio, S. Dai, D.-e. Jiang, Quantum Mechanical Basis for Kinetic Diameters of Small Gaseous Molecules, The Journal of Physical Chemistry A, 118 (2014) 1150-1154.

[139] A.G. Palkhiwala, R.J. Gorte, Characterization of H-FER and H-TON using temperature-programmed desorption of alkylamines, Catalysis Letters, 57 (1999) 19-23.

[140] C.B.a.L.B. McCusker, Database of Zeolite Structures.

[141] S.D. Bhat, T.M. Aminabhavi, Novel sodium alginate composite membranes incorporated with SBA-15 molecular sieves for the pervaporation dehydration of aqueous mixtures of isopropanol and 1,4-dioxane at 30°C, Microporous and Mesoporous Materials, 91 (2006) 206-214.

[142] X. Qiao, T.-S. Chung, W.F. Guo, T. Matsuura, M.M. Teoh, Dehydration of isopropanol and its comparison with dehydration of butanol isomers from thermodynamic and molecular aspects, Journal of Membrane Science, 252 (2005) 37-49.

[143] D.J. Parrillo, A.T. Adamo, G.T. Kokotailo, R.J. Gorte, Amine adsorption in H-ZSM-5, Applied Catalysis, 67 (1990) 107-118.

[144] M.T. Aronson, R.J. Gorte, W.E. Farneth, The influence of oxonium ion and carbenium ion stabilities on the Alcohol/H-ZSM-5 interaction, Journal of Catalysis, 98 (1986) 434-443.

[145] D.H. Aue, H.M. Webb, M.T. Bowers, Quantitative proton affinities, ionization potentials, and hydrogen affinities of alkylamines, Journal of the American Chemical Society, 98 (1976) 311-317.

[146] Z. Zhao, S. Xu, M.Y. Hu, X. Bao, C.H.F. Peden, J. Hu, Investigation of Aluminum Site Changes of Dehydrated Zeolite H-Beta during a Rehydration Process by High-Field Solid-State NMR, The Journal of Physical Chemistry C, 119 (2015) 1410-1417.

[147] B.H. Wouters, T.H. Chen, P.J. Grobet, Reversible Tetrahedral–Octahedral Framework Aluminum Transformation in Zeolite Y, Journal of the American Chemical Society, 120 (1998) 11419-11425.

[148] J.Q. Bond, C.S. Jungong, A. Chatzidimitriou, Microkinetic analysis of ring opening and decarboxylation of γ-valerolactone over silica alumina, Journal of Catalysis, 344 (2016) 640-656.

[149] D.J. Parrillo, R.J. Gorte, W.E. Farneth, A calorimetric study of simple bases in H-ZSM-5: a comparison with gas-phase and solution-phase acidities, Journal of the American Chemical Society, 115 (1993) 12441-12445.

VITA

NAME OF AUTHOR:

Anargyros Chatzidimitriou

PLACE OF BIRTH:

Athens, Greece

UNDERGRADUATE SCHOOLS ATTENDED:

National Technical University of Athens, Greece

DEGREES AWARDED:

Diploma in Chemical Engineering, 2011, National Technical University of Athens